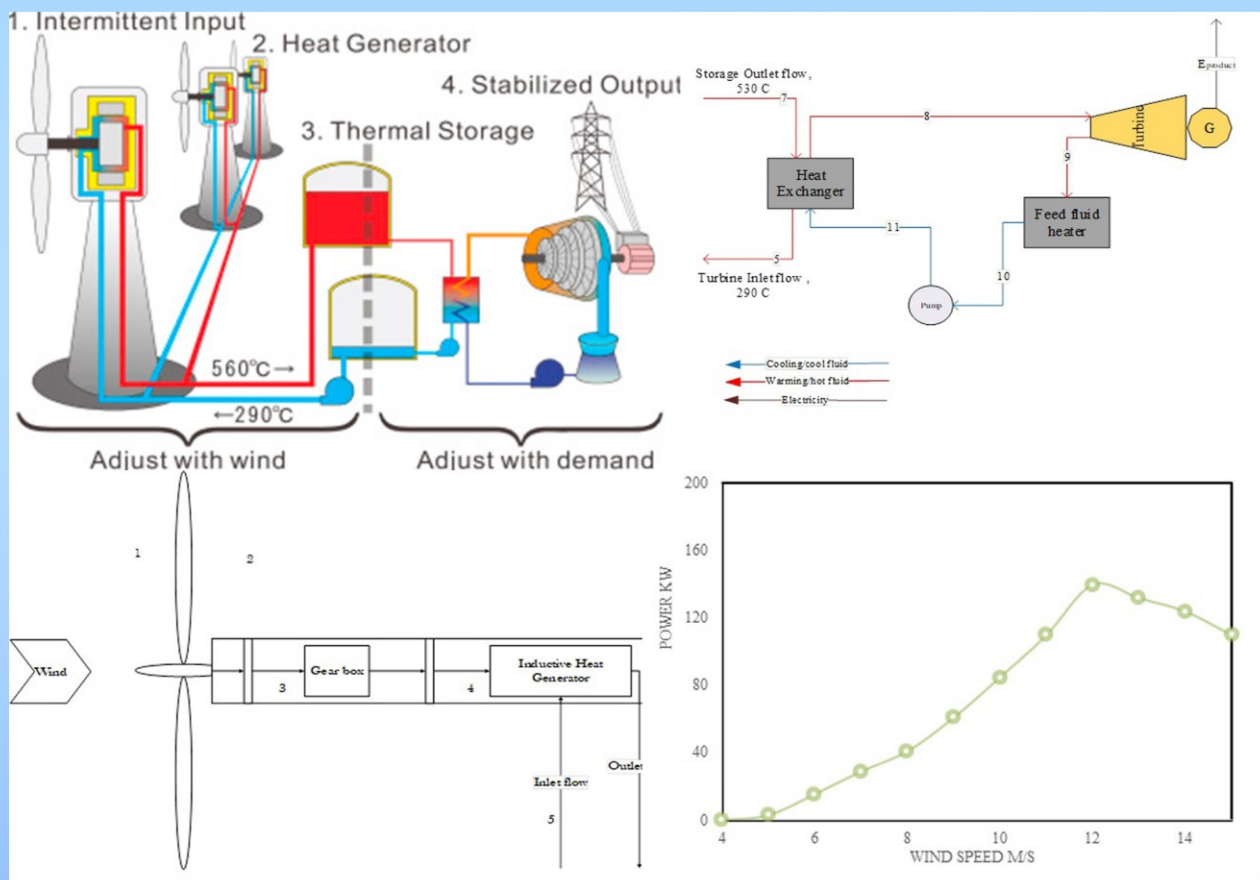


Trends in Renewable Energy

Volume 7, December 2021



Cover image: Wind-Thermal System, see article by Norouzi in this issue.



Trends in Renewable Energy

ISSN: 2376-2136 (Print) ISSN: 2376-2144 (Online)

<http://futureenergysp.com/>

Trends in Renewable Energy is an open accessed, peer-reviewed semi-annual journal publishing reviews and research papers in the field of renewable energy technology and science.

The aim of this journal is to provide a communication platform that is run exclusively by scientists working in the renewable energy field. Scope of the journal covers: Bioenergy, Biofuel, Biomass, Bioprocessing, Biorefinery, Biological waste treatment, Catalysis for energy generation, Energy conservation, Energy delivery, Energy resources, Energy storage, Energy transformation, Environmental impact, Feedstock utilization, Future energy development, Green chemistry, Green energy, Microbial products, Physico-chemical process for Biomass, Policy, Pollution, Renewable energy, Smart grid, Thermo-chemical processes for biomass, etc.

The Trends in Renewable Energy publishes the following article types: peer-reviewed reviews, mini-reviews, technical notes, short-form research papers, and original research papers.

The article processing charge (APC), also known as a publication fee, is fully waived for the Trends in Renewable Energy.

Editorial Team of Trends in Renewable Energy

EDITOR-IN-CHIEF

Dr. Bo Zhang Prof., School of Chemical Engineering & Pharmacy, Wuhan Institute of Technology, China
Dr. Changyan Yang Prof., School of Chemical Engineering & Pharmacy, Wuhan Institute of Technology, China

HONORARY CHAIRMEN

Dr. Yong Wang Voiland Distinguished Professor, The Gene and Linda Voiland School of Chemical Engineering and Bioengineering, Washington State University, United States
Dr. Mahendra Singh Sodha Professor, Lucknow University; Former Vice Chancellor of Devi Ahilya University, Lucknow University, and Barkatulla University; Professor/Dean/HOD/Deputy Director at IIT Delhi; Padma Shri Award; India
Dr. Elio Santacesaria Professor of Industrial Chemistry, CEO of Eurochem Engineering srl, Italy

VICE CHAIRMEN

Dr. Mo Xian Prof., Assistant Director, Qingdao Institute of BioEnergy and Bioprocess Technology, Chinese Academy of Sciences, China

EDITORS

Dr. Yiu Fai Tsang, Associate Prof., Department of Science and Environmental Studies, The Education University of Hong Kong
Dr. Melanie Sattler Dr. Syed Qasim Endowed Professor, Dept. of Civil Engineering, University of Texas at Arlington, United States
Dr. Attila Bai Associate Prof., University of Debrecen, Hungary
Prof. Christophe Pierre Ménézo University of Savoy Mont-Blanc, France
Dr. Moinuddin Sarker MCIC, FICER, MInstP, MRSC, FARSS., VP of R & D, Head of Science/Technology Team, Natural State Research, Inc., United States
Dr. Suzana Yusup Associate Prof., Biomass Processing Laboratory, Centre for Biofuel and Biochemical Research, Green Technology Mission Oriented Research, Universiti Teknologi PETRONAS, Malaysia
Dr. Zewei Miao Global Technology Development, Monsanto Company, United States
Dr. Hui Wang Pfizer Inc., United States
Dr. Shuangning Xiu North Carolina Agricultural and Technical State University, United States
Dr. Junming XU Associate Prof., Institute of Chemical Industry of Forest Products, China Academy of Forest, China
Dr. Hui Yang Prof., College of Materials Science and Engineering, Nanjing Tech University, China
Dr. Ying Zhang Associate Prof., School of Chemistry and Materials Science, University of Science and Technology of China, China
Dr. Ming-Jun Zhu Prof., Assistant Dean, School of Bioscience & Bioengineering, South China University of Technology, China

EDITORIAL BOARD

Dr. Risabh Dev Shukla Dean and Associate Prof., Department of Electrical Engineering, Budge Budge Institute of Technology Kolkata, India
Dr. Neeraj Gupta Indian Institute of Technology Roorkee, India

Dr. Elena Lucchi	Politecnico di Milano, Italy
Dr. Muhammad Mujtaba Asad	Faculty of Technical and Vocational Education, Universiti Tun Hussein Onn Malaysia, Malaysia
Dr. Afzal Sikander	Department of Instrumentation and Control Engineering, Dr. B. R. Ambedkar National Institute of Technology, India
Dr. Padmanabh Thakur	Professor and Head, Department of Electrical Engineering, Graphic Era University, India
Dr. K. DHAYALINI	Professor, Department of Electrical and Electronics Engineering, K. Ramakrishnan College of Engineering, Tamilnadu, India
Shangxian Xie	Texas A&M University, United States
Dr. Tanmoy Dutta	Sandia National Laboratories, United States
Dr. Efstathios Stefanos	Pontifical Catholic University of Ecuador, Faculty of Exact and Natural Sciences, School of Physical Sciences and Mathematics, Ecuador
Dr. Xin Wang	Miami University, United States
Dr. Rami El-Emam	Assist. Prof., Faculty of Engineering, Mansoura University, Egypt
Dr. Rameshprabu Ramaraj	School of Renewable Energy, Maejo University, Thailand
Dr. ZAFER ÖMER ÖZDEMİR	Kirklareli University, Technology Faculty, Turkey
Dr. Vijay Yeul	Chandrapur Super Thermal Power Station, India
Dr. Mohanakrishna Gunda	VITO - Flemish Institute for Technological Research, Belgium
Dr. Shuai Tan	Georgia Institute of Technology, United States
Shahabaldin Rezanian	Universiti Teknologi Malaysia (UTM), Malaysia
Dr. Madhu Sabnis	Contek Solutions LLC, Texas, United States
Dr. Qiang Yan	Mississippi State University, United States
Dr. Mustafa Tolga BALTA	Associate Prof., Department of Mechanical Engineering, Faculty of Engineering, Aksaray University, Turkey
Dr. María González Alriols	Associate Prof., Chemical and Environmental Engineering Department, University of the Basque Country, Spain
Dr. Nattaporn Chaiyat	Assist. Prof., School of Renewable Energy, Maejo University, Thailand
Dr. Nguyen Duc Luong	Institute of Environmental Science and Engineering, National University of Civil Engineering, Vietnam
Mohd Lias Bin Kamal	Faculty of Applied Science, Universiti Teknologi MARA, Malaysia
Dr. N.L. Panwar	Assistant Prof., Department of Renewable Energy Engineering, College of Technology and Engineering, Maharana Pratap University of Agriculture and Technology, India
Dr. Caio Fortes	BASF, Brazil
Dr. Flavio Praticco	Department of Methods and Models for Economics, Territory and Finance, Sapienza University of Rome, Italy
Dr. Wennan ZHANG	Docent (Associate Prof.) and Senior Lecturer in Energy Engineering, Mid Sweden University, Sweden
Dr. Ing. Stamatis S. Kalligeros	Associate Prof., Hellenic Naval Academy, Greece
Carlos Rolz	Director of the Biochemical Engineering Center, Research Institute at Universidad del Valle, Guatemala
Ms. Liliash Makashini	Copperbelt University, Zambia
Dr. Ali Mostafaeipour	Assistant Prof., Industrial Engineering Department, Yazd University, Iran
Dr. Camila da Silva	Prof., Maringá State University, Brazil
Dr. Anna Skorek-Osikowska	Silesian University of Technology, Poland
Dr. Shek Atiqure Rahman	Sustainable and Renewable Energy Engineering, College of Engineering, University of Sharjah, Bangladesh
Dr. Emad J Elnajjar	Associate Prof., Department of Mechanical Engineering, United Arab Emirates University, United Arab Emirates
Dr. Seyed Soheil Mousavi Ajarostaghi	Babol Noshirvani University of Technology, Babol, Iran
Dr. Dinesh K. Sharma	National Ecology and Environment Foundation, India
Dr. Lakshmana Kumar Ramasamy	Department of Corporate relations, Hindusthan College of Engineering and Technology, India
Dr. S. Venkata Ramana	SUSU/National Research University, Russian Federation
Dr. Priyanka Marathey	Department of Solar Energy, Pandit Deendayal Petroleum University, India
Osamah Siddiqui	University of Ontario Institute of Technology, Canada

Dr. Rupendra Kumar Pachauri	Assistant Prof., Electrical and Electronics Engineering Department, University of Petroleum and Energy Studies, India
Dr. Jun Mei	School of Chemistry and Physics, Science and Engineering Faculty, Queensland University of Technology, Australia
Dr. Valeria Di Sarli	Institute for Research on Combustion, National Research Council of Italy, Italy
Dr. Utkucan Şahin	Assistant Prof., Department of Energy Systems Engineering, Faculty of Technology, Muğla Sıtkı Koçman University, Turkey
Dr. ALIASHIM ALBANI	School of Ocean Engineering, Universiti Malaysia Terengganu, Malaysia
Dr. Ashwini Kumar	Assistant Prof., College of Engineering, HSBPVT's Parikrama Group of Institutions, India
Dr. Hasan AYDOGAN	Associate Prof., Mechanical Engineering Department, Selcuk University, Turkey
Dr. Jiekang Wu	Professor, School of Automation, Guangdong University of Technology, China
Dr. Ong Huei Ruey	DRB-HICOM University of Automotive, Malaysia
Dr. Miguel Ángel Reyes Belmonte	IMDEA Energy Institute, Spain
Dr. Chitra Venugopal	Associate Professor in Electrical Engineering, University of Trinidad and Tobago, Trinidad
Dr. Amit Kumar Singh	Assistant Prof., Instrumentation & Control Engineering Department, Dr. B.R.A. National Institute of Technology, India
Dr. Suvanjan Bhattacharyya	University of Pretoria, South Africa
Dr. Karunesh Tiwari	Babu Banarasi Das University, India
Dr. Sharadrao A. Vhanalkar	Karmaveer Hire Arts, Science, Commerce and Education College, India
Dr. Prasenjit Chatterjee	Assistant Prof. and Head, MCKV Institute of Engineering, India
Dr. S. Balamurugan	Mindnotix Technologies, India
Dr. Mohammad Nurunnabi	University of Oxford, United Kingdom
Dr. Kenneth Okedu	Caledonian College of Engineering, Oman
Dr. Cheng Zhang	Sr. Materials Engineer, Medtronic, Inc., United States
Dr. Chandani Sharma	Assistant Prof., Department of Electrical Engineering, Graphic Era University, India
Dr. Kashif Irshad	Assistant Prof., Mechanical Engineering Department, King Khalid University, Saudi Arabia
Dr. Abhijit Bhagavatula	Principal Lead Engineer, Southern Company Services, United States
Dr. S. Sathish	Associate Prof., Department of Mechanical Engineering, Hindustan University, India
Mr. A. Avinash	Assistant Prof., KPR Institute of Engineering & Technology, India
Dr. Bindeshwar Singh	Assistant Prof., Kamla Nehru Institute of Technology, India
Dr. Yashar Hashemi	Tehran Regional Electric Company, Iran
Dr. Navanietha Krishnaraj R	South Dakota School of Mines and Technology, United States
Dr. SANDEEP GUPTA	JECRC University, India
Dr. Shwetank Avikal	Graphic Era Hill University, India
Dr. Xianglin Zhai	Poochon Scientific LLC, United States
Dr. Rui Li	Associate Prof., College of Engineering, China Agricultural University, China
Dr. Adam Elhag Ahmed	National Nutrition Policy Chair, Department of Community Services, College of Applied Medical Sciences, King Saud University, Saudi Arabia
Dr. Jingbo Li	Massachusetts Institute of Technology, United States
Dr. Srikanth Mutnuri	Associate Prof., Department of Biological Sciences, Associate Dean for International Programmes and Collaboration, Birla Institute of Technology & Science, India
Dr. Bashar Malkawi	Global Professor of Practice in Law, James E. Rogers College of Law, University of Arizona, United States
Dr. Simona Silvia Merola	Istituto Motori - National Research Council of Naples, Italy
Dr. Hakan Caliskan	Faculty of Engineering, Department of Mechanical Engineering, Usak University, Turkey
Dr. Umashankar Subramaniam	Associate Prof., College of Engineering, Prince Sultan University, Saudi Arabia
Dr. Tayfun GÜNDOĞDU	Faculty of Electrical and Electronic Engineering, Department of Electrical Engineering, Istanbul Technical University, Turkey
Dr. Yukesh Kannah R	Department of Civil Engineering, Anna University Regional Campus, India

Jean Bosco Mugiraneza
Dr. R. Parameshwaran

Dr. Endong Wang

University of Rwanda, Rwanda
Assistant Prof., Dept. of Mechanical Engineering, Birla Institute of Technology
& Science (BITS-Pilani), India
Associate Prof., Department of Sustainable Resources Management, College
of Environmental Science and Forestry, State University of New York (SUNY-
ESF)

Table of Contents

Volume 7, December 2021

Articles

Enhance the Output Power of a Shaded Solar Photovoltaic Arrays with Shade Dispersion based TCT

Configuration

V Bala Raju, Ch Chengaiah.....1-23

Life Cycle Assessment of A Hydrocarbon-based Electrified Cleaning Agent

Peng Liu, Bo Zhang, Changyan Yang, Yu Gong, Yinhang Qu, Jiayi Li, Bohan Yang, Yigang Ding24-52

Pyrolysis-Gas Chromatography/Mass Spectrometry Analysis of Oils from Different Sources

Qi Qiu, Yiting Zhang..... 53-72

Exergy and Energy Analysis of Wind-Thermal System

Nima Norouzi..... 73-86

Information Technology, Artificial Intelligence and Machine Learning in Smart Grid – Performance

Comparison between Topology Identification Methodology and Neural Network Identification

Methodology for the Branch Number Approximation of Overhead Low-Voltage Broadband over

Power Lines Network Topologies

Athanasios G. Lazaropoulos 87-113

World on the Road to 100% Renewable Energy

Nima Norouzi..... 114-126

Enhance the Output Power of a Shaded Solar Photovoltaic Arrays with Shade Dispersion based TCT Configuration

V. Bala Raju*, Dr. Ch. Chengaiah

Department of Electrical and Electronics Engineering, Sri Venkateswara University College of Engineering, Tirupati, India

Received April 9, 2021; Accepted April 19, 2021; Published April 22, 2021

Partial shading has a negative impact on the performance parameters of a Solar Photovoltaic (PV) array, because it shades certain panels while leaving others un-shaded. This article focuses on modeling, comparing and performance assessment of 6×6, 6×5 and 5×6 size shadowed solar PV arrays under different partial shading cases in the MATLAB/ Simulink software. For this purpose, the simulation of series-parallel (SP), Total-Cross-Tied (TCT) and proposed shade dispersion based TCT (SD-TCT) type of array configurations was carried out under few shading cases. The proposed SD-TCT was designed using the shades dispersion technique, which is based on a number logic approach. In this technique, in order to effectively remove the row-current mismatches in the TCT PV array configuration, the shaded and un-shaded modules in an array were re-arranged, so that the shading on modules expands across the whole array. The physical placement of the TCT array modules has been reordered in accordance with the proposed number logic pattern exclusive of altering the electrical links among the panels. The simulation results showed that the performance of the SD-TCT type was superior to that of conventional array configurations.

Keywords: PV Array; Modules; Configurations; Mismatch Losses; Power improvement; Shading Cases

Introduction

The power generated by solar photovoltaic (PV) plants varies with the temperature and irradiance of the PV module. Shades, such as shadows of surrounding trees, shifting clouds and dust deposition on modules, directly influence the cell temperature and radiation level of the PV system. In the shading conditions (SC), the power generated by the array is reduced and results in the output P-V curves to have multiple peaks *i.e.*, LMPP (Local maximum power point) and GMPP (Global maximum power point). Several MPPT tracking methods for LMPP and GMPP of the solar PV array configurations have been proposed in the literature. One solution for reducing losses from malfunction and shading is PV array configurations. The foremost conventional PV array configuration or arrangements or structures are Parallel-Series (SP), Bridge-Linked (BL), Series (S), Honey-Comb (HC), Parallel (P), Total-Cross-Tied (TCT) type. In the literature of [1-5], a brief comparison study among S, P, SP, TCT, and

*Corresponding author: vbrajuu@gmail.com

BL structures was conducted in the MATLAB/Simulink environment. The findings suggested that the design of TCT achieves the best output power under most SCs. A further alternative is the use of dynamic reconfiguration methods such as power electronics Equalizer (PEE) type and the electric array reconfiguration (EAR) methods to remove multiple peaks of the shaded array P-V-specifications and thus increase the power produced by an array. The solution is also proposed in the literature. But more sensors, switches, and control algorithms are essential for implementing the above techniques in an enormous PV farm [6-10].

In order to overcome this limit, it is suggested to adopt different static array reconfiguration methods, such as magic-square pattern, Sudoku and optimal sudoku pattern and Futoshiki puzzle pattern [11-12] to boost the power generation in SC and rearrange the TCT configuration with $i \times j$ size array (where i is no. of rows and j is no. of columns). In the above techniques, the optimum location of any module is calculated based on the shadow model to minimize the shading losses, and the PV panel is relocated without modifying the electrical links. Such techniques, however, refer only to a square type of PV arrays and not to non-square arrays, *i.e.*, $i \neq j$. For digit i , which is either odd or even number, the current study suggests a novel approach based on shade dispersion (SD-TCT) configuration of arrays $i=j$ and $i \neq j$. The proposed method for rearranging the row location of an $i \times j$ PV array is generalized in this context. In different shading conditions, a comparison is made of the SD-TCT configuration with different existing settings, including SP and TCT of an $i \times j$ ($i, j=6$ and 5) array. In the SD-TCT structure, the modules positions only need to be changed once during installation, *i.e.*, electrical links alteration of modules are unnecessary. Therefore, for the execution of the existing scheme in real time at a wide PV system, and it doesn't need a lot of switches, sensors, control algorithms. The proposed structure spreads the shadows across the PV array to ensure increased the array power under SC.

The rest paper is structured as modeling of a PV array, various array configurations, the methodology used in the proposed configuration, and the simulation, modeling and performance study of different size arrays.

Mathematical Modeling

Modeling of Photovoltaic Array

The PV cell transforms the light energy into electricity and increases the output voltage by the series of cells known as module or panel. The PV array is a grouping of the series (N_S) and parallel (N_P) connected panels, which are exposed in Figure 1.

The equations of 1, 2, and 3 are represented mathematically of a solar PV cell, module, and array [13-14], respectively.

$$I_{cell} = I_{ph} - I_0 \left[\exp \left\{ \frac{q(V_{cell} + I_{cell}R_{ser})}{KAT_c} \right\} - 1 \right] - \left[\frac{(V_{cell} + I_{cell}R_{ser})}{R_{par}} \right] \quad \text{--- (1)}$$

$$I_m = I_{ph} - I_0 \left[\exp \left(\frac{q(V_m + I_m R_{ser})}{n_s K A T_c} \right) - 1 \right] - \left[\frac{(V_m + I_m R_{ser})}{R_{par}} \right] \quad \text{--- (2)}$$

$$I_a = N_P \cdot I_{ph} - N_P \cdot I_0 \left[\exp \left(\frac{q(V_a + \frac{N_S}{N_P} I_a R_{ser})}{N_S K A T_c} \right) - 1 \right] - \left[\frac{(V_a + \frac{N_S}{N_P} I_a R_{ser})}{\frac{N_S}{N_P} \cdot R_{par}} \right] \quad \text{--- (3)}$$

where V_{Cell} and I_{Cell} , V_m and I_m , V_a and I_a are voltage[V] and current[A] of a solar PV cell, module and array, respectively. N_s and N_p are the no. of series and parallel connected modules, n_s is the no. of series connection pv cells, I_0 is reverse saturation current [A], I_{ph} is the photo-generated current [A], R_{ser} and R_{par} are series and parallel resistances[Ω], and a is the ideality factor. Cell thermal voltage is given as $V_{\text{Th}} = k T_C/q$, where q : Charge of electron, T_C : Cell operating temp, and k : Boltzmann's constant.

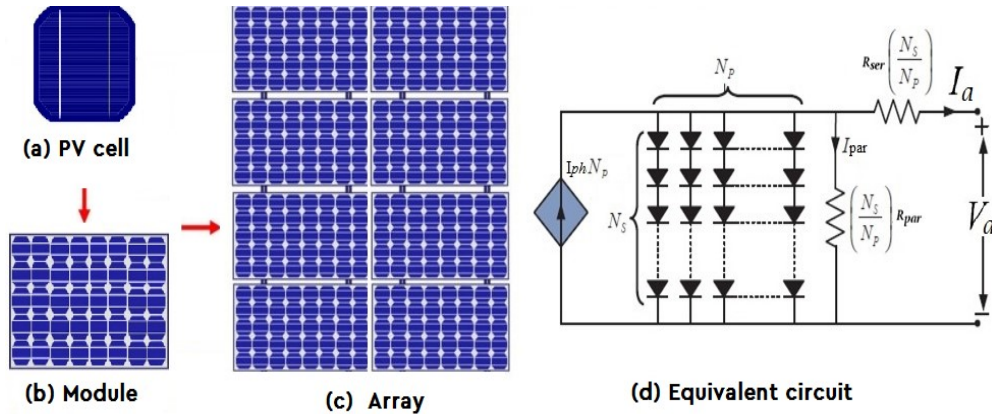


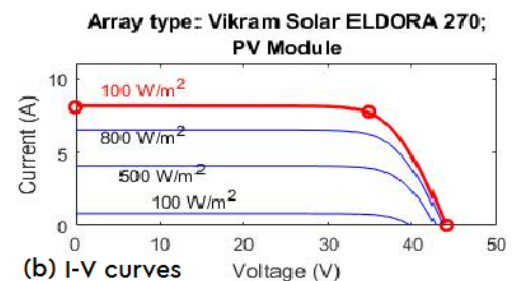
Figure 1. Solar PV array formation

Modeling of Photovoltaic Array

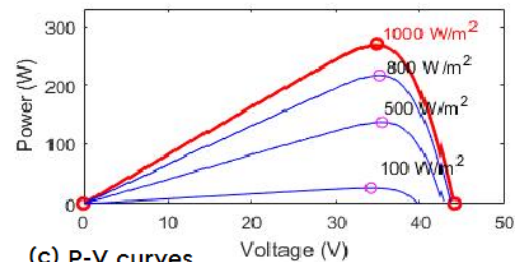
In this work, the Vikram Solar PV module is used for the simulation of SP, TCT, SD-TCT array arrangements. The specifications and output curves of module are shown in Figure 2.

Electrical Parameters		Values
Maximum Power		270 W
Cells per module	N_{cell}	72
Open circuit voltage	V_{OC}	44 V
Short-circuit current	I_{SC}	8.1 A
Voltage at maximum power point	V_{MP}	34.7 V
Current at maximum power point	I_{MP}	7.8 A
Temperature coefficient of V_{oc}		-0.3583% / $^{\circ}\text{C}$
Temperature coefficient of I_{sc}		0.0249% / $^{\circ}\text{C}$
Light generated current	I_L	8.1924 A
Diode saturation current	I_0	2.4871e-10
Diode ideality factor		0.98223
Shunt resistance	R_{sh}	3126.5623 Ω
Series resistance	R_s	0.52303 Ω

(a) Vikram Solar PV module parameters



(b) I-V curves



(c) P-V curves

Figure 2. Parameters and output curves of a solar PV module

Solar PV Array Configurations

The foremost traditional configurations are total-cross-tied (TCT), series (S), bridge-linked (BL), series-parallel (SP), honey-comb (HC), parallel (P) type of arrangements, as illustrated in Figure 3. The difference in row currents is created because of shaded conditions, and PV panels with lower irradiation are thus bypassed. Therefore,

many peaks are formed in the P-V output characteristics, and therefore some power is lost. PV array reconfigurations or rearrangements methods are used to spread the shade uniformly around the PV array, which can significantly reduce the mismatch losses (ML) in PV systems. Researchers have made numerous efforts to research and evaluate the shading effect on array configurations to minimize ML and to achieve maximum power production. In other words, the lower radiation PV module is relocated electrically or physically so that a single P-V peak is reached. This paper only considered SP, TCT, and proposed SD-TCT (re-arranged TCT connection) type of configurations for analyzing the performance of different sizes PV arrays.

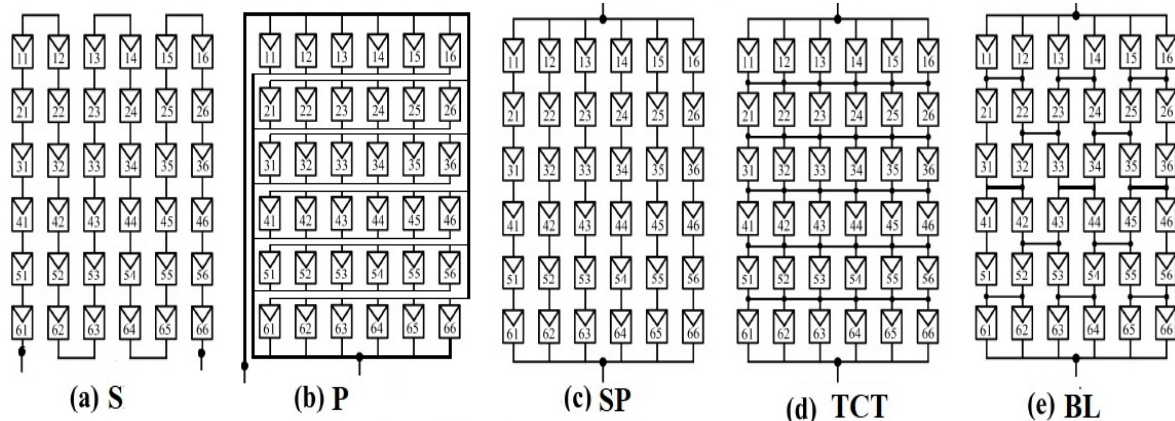


Figure 3. Traditional 6×6 size SPV array configurations

Modeling of TCT Configuration

The TCT (Total Cross Tied) configuration is a series-parallel version in which all rows are cross-linked to the TCT type structure. PV array's lifespan is nearly doubled by the introduction of cross-links to increase the array power. As a result of the connecting links, more loops are created. Because of this, few effects are investigated: voltage limitations in the array are found, and different currents flow throughout the same-string PV panels. In order to locate the global peak (GP) power, it is extremely important to calculate row currents in the TCT form. The current row estimate for a TCT scheme is considered to be a 6×6 PV array.

The output current in a row is the sum of the module current limits. The array currents are calculated for any TCT row by:

$$I_{Rn} = \sum_{n=1}^6 I_m * S_n \quad \text{--- (4)}$$

where I_m is the PV module's maximum current at full irradiance of 1000 W/m² (STC), and $S_n = G_s/G_0$, in which G_s is the solar irradiance at shaded condition, and G_0 is the STC irradiance. Figure 3(d) illustrates the 6×6 TCT array, and the array voltage for six rows is given by the Kirchhoff's Voltage Law (KVL) as:

$$V_a = \sum_{i=1}^6 V_{mi} \quad \text{--- (5)}$$

where V_a is the array voltage and V_{mi} is the voltage of i^{th} row of the PV array. Applying the current law of Kirchhoff to calculate the current at each node in the TCT array and the array current is given as:

$$I_a = \sum_{j=1}^6 (I_{ij} - I_{(i+1)j}) = 0, \quad i = 1,2,3,4,5,6 \quad \text{--- (6)}$$

where i and j are the number of row and column, respectively.

Methodology

The General Rule for Proposed SD-TCT Array Configuration

The proposed SD-TCT array arrangement is applicable for the shading sequence or patterns of any size, *i.e.*, the row and column size could be odd or even number. The rule for configuring a general solar pattern can be defined as:

$$n_{ij}, \text{ Where } \begin{cases} i = \text{No. of rows } (i = 1,2,3,4,5,6) \\ j = \text{No. of Columns } (j = 1,2,3,4,5,6) \end{cases}$$

where n_{ij} is written for the n^{th} element of the i^{th} row and j^{th} column of a shading sequence.

To determine the logic number in a column, the following equations can be considered:

$$j = \begin{cases} j, & \text{if } i = 1 \\ j + (i - 1) \cdot \text{floor}\left(\frac{j_{\max}}{3}\right), & i > 1 \end{cases}$$

$$\text{if } j < j_{\max}, \quad j = j$$

$$\text{else } j = j - j_{\max}$$

If any number is repeated in a column (j), just add 1 to the corresponding column, *i.e.*, $j=j+1$, otherwise take the same number in a column.

Formation of Proposed SD-TCT Configuration

An SD-TCT design aims primarily to dispatch shadows around the array under SC by arranging an $i \times j$ array column location with the numbers 1 to j as shown in Table 1. The proposed logic of numbers is developed for $i =$ odd and even for the column location arrangement of the $i \times j$ PV array. The repeating of the numbers in a specific column (C) and row (R) of a PV sequence is avoided by adding 1 to the previous logic number with the goal of obtaining a unique solution. For any array size, the proposed number logic approach is used, which is used in this paper for 6×6 , 6×5 , and 5×6 arrays.

The proposed design, therefore, reveals its pattern for puzzles and arrangements of the PV array optimized for SD-TCT (Shade dispersion based TCT configuration) arrangement in Figure 4. The 1st number in the box represents a logic number, and the 2nd number denotes the column number. The row and column positions in a 6×6 array are arranging with the numbers 1 to 6 in the suggested arrangement, as present in Figure 4(a). Here, the first-row column location of the array contains a number in an upwards order from 1 to 6. Numbers 1 to 6 are grouped from the second row using the proposed number logic approach, as shown in Table 1.

Table 1. Arrangement of a 6x6 array with proposed shade dispersion number logic approach

Columns Rows	C:1	C:2 (C:1 +1)	C:3 (C:2 +1)	C:4 (C:3 +1)	C:5 (C:4 +1)	C:6 (C:5 +1)
R:1	1	2	3	4	5	6
R:2 (R:1 +2)	3	4	5	6	7-6= 1	8-6= 2
R:3 (R:2 +2)	5	6	7-6= 1	8-6= 2	3	4
R:4 (R:3 +2)	7-6=1 1+1= 2	8-6=2 2+1= 3	3+1= 4	4+1= 5	5+1= 6	6+1=7 7-6= 1
R:5 (R:4 +2)	4	5	6	7-6= 1	8-6= 2	3
R:6 (R:5 +2)	6	7-6= 1	8-6= 2	3	4	5

Table 2. Arrangement of a 6x5 array with proposed shade dispersion number logic approach

Columns Rows	C:1	C:2 (C:1 +1)	C:3 (C:2 +1)	C:4 (C:3 +1)	C:5 (C:4 +1)
R:1	1	2	3	4	5
R:2 (R:1 +2)	3	4	5	6	7-6= 1
R:3 (R:2 +2)	5	6	7-6= 1	8-6= 2	3
R:4 (R:3 +2)	7-6=1 1+1= 2	8-6=2 2+1= 3	3+1= 4	4+1= 5	5+1= 6
R:5 (R:4 +2)	4	5	6	7-6= 1	8-6= 2
R:6 (R:5 +2)	6	7-6= 1	8-6= 2	3	4

Table 3. Arrangement of a 5×6 array with proposed shade dispersion number logic approach

Columns Rows	C:1	C:2 (C:1 +1)	C:3 (C:2 +1)	C:4 (C:3 +1)	C:5 (C:4 +1)	C:6 (C:5 +1)
R:1	1	2	3	4	5	6 6-5= 1
R:2 (R:1 +2)	3	4	5	6 6-5= 1	2	3
R:3 (R:2 +2)	5	6 6-5= 1	2	3	4	5
R:4 (R:3 +2)	7-5=2	3	4	5	6 6-5= 1	2
R:5 (R:4 +2)	4	5	6 6-5= 1	2	3	4

11	22	33	44	55	66
31	42	53	64	15	26
51	62	13	24	35	46
21	32	43	54	65	16
41	52	63	14	25	36
61	12	23	34	45	56

(a) 6x6 SD-TCT

11	22	33	44	55
31	42	53	64	15
51	62	13	24	35
21	32	43	54	65
41	52	63	14	25
61	12	23	34	45

(b) 6x5 SD-TCT

11	22	33	44	55	16
31	42	53	14	25	36
51	12	23	34	45	56
21	32	43	54	15	26
41	52	13	24	35	46

(c) 5x6 SD-TCT

Figure 4. Arrangement of 6×6, 6×5 and 5×6 arrays with proposed number logic approach

Re-arrangement of Array Modules in TCT Configuration

Reconfiguration methods are used to spread the partial shade effect with every conventional configuration. Several literature attempts are made to establish the best scheme for PV systems for all operating conditions in order to find the best configuration [15–16]. TCT is now the most feasible interconnections scheme for achieving efficient and sustainable photovoltaic power generation based on crucial evaluations with TCT, BL, and SP. Some scholarly studies for PV array reconfiguration that adopts TCT interconnect are available in the literature. A smart reconfiguration approach is mandatory to define the new positions in a TCT PV array. A new physical shade dispersion device based on the logic number is thus proposed for this work. The method follows the column wise relocation process in order to rearrange the TCT array, which allows shades with a minimum row current difference to be dispersed. The methodology opted for rearrangement of array modules in TCT with a number logic approach, as described in the previous section. The formation of 6×6, 6×5 and 5×6 array configurations with shade dispersion by logic number approach is illustrated in Figure 5(c), 5(d) and 5(e), respectively.

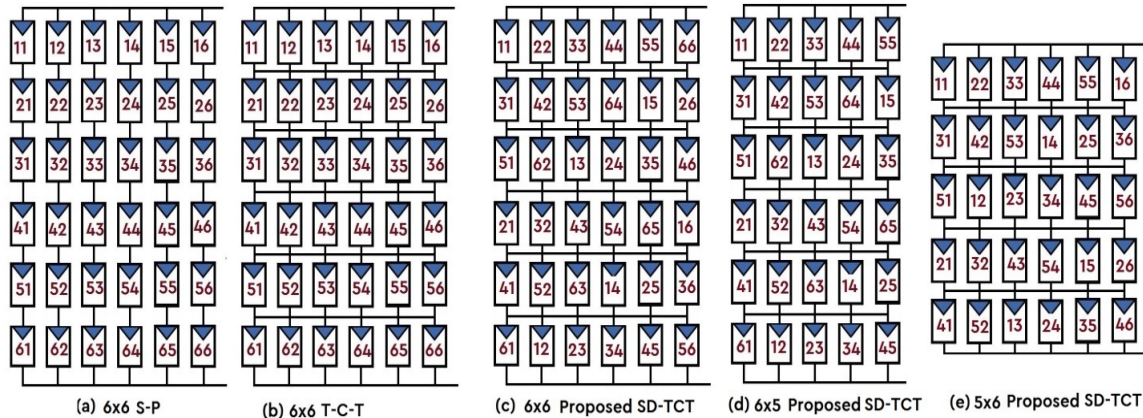


Figure 5. (a)-(b): S-P and TCT, (c)-(e): Re-arrangements of TCT array (SD-TCT)

Physical Relocation of Modules in the Proposed Configuration

The most difficult problem of this procedure was to pick the efficient reconfigurable sequence to spread the shading through the array. The first digit is the logical number in each box in the proposed SD-TCT arrangement, and the 2nd digit indicates the column. This method has the lead of matching the numbers 1 to 6 without repeating them. The purpose of this model system is to share out shadow effects without altering electrical connections by modifying their physical location of PV modules. This means that the panel number 34 is at a third row-fourth column in TCT. But in SD-TCT format, it moves physically into 4th column in the 6th row, as shown in Figure 6(c). Different improvements are made to all PV panels, which increase the current in an entry node and decrease the circumvention of the array modules. This increases the array of power efficiency. Figures 6(b)–6(c) demonstrate the reorganization of array modules by the use of the proposed arrangement without modifying the electrical links to the panels in the shading cases.

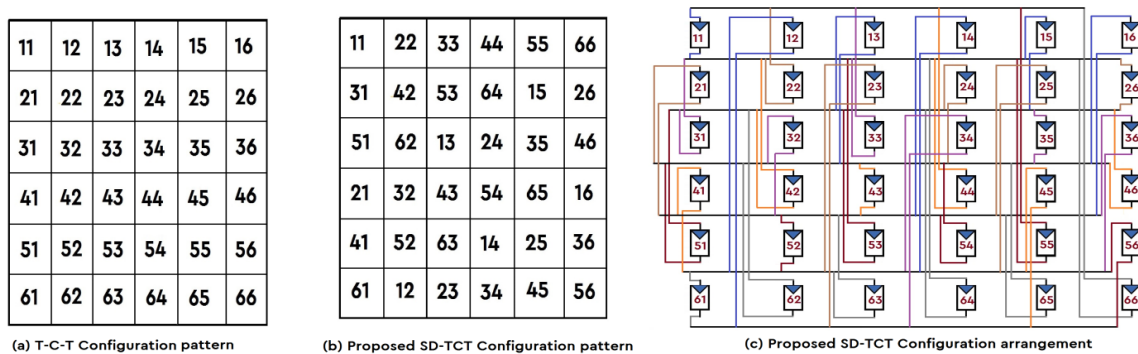


Figure 6. Arrangement of proposed 6×6 SD-TCT array configuration

Analysis of Shading Patterns

Solar PV modules in the array are partly shaded by shadows in surrounding trees, moveable clouds, sand, or dust deposition of the panels. In this paper, shading cases are considered for performance analysis illustrated in Figures 7(a), 9(a), 10(a), and corresponding shade dispersions in SD-TCT configuration are shown in Figures 7(b), 9(b), 10(b), respectively. Each shaded module receives a solar irradiance of 500 W/m^2 , and the maximum irradiance of un-shaded modules is 1000 W/m^2 .

Shading Cases for a 6×6 Array

The shading cases considered for analyzing the shade dispersion in SD-TCT configuration of a 6×6 SPV array is illustrated in Figure 7. Figure 7(a) represents the shading pattern in TCT array connection and Figure 7(b) represents the shade dispersion in SD-TCT arrangement with number logic approach as explained in the previous section. The proposed method disperses the shades on PV module with in a column only. So, in the complete column shading cases, there is no shade dispersion occurs as shown in case-7: single column shading, and case-9: two column shading of a 6×6 array. In non-shading case (*i.e.*, case-U), all 36 modules in a 6×6 PV array receives full irradiance at STC of 1000 W/m².

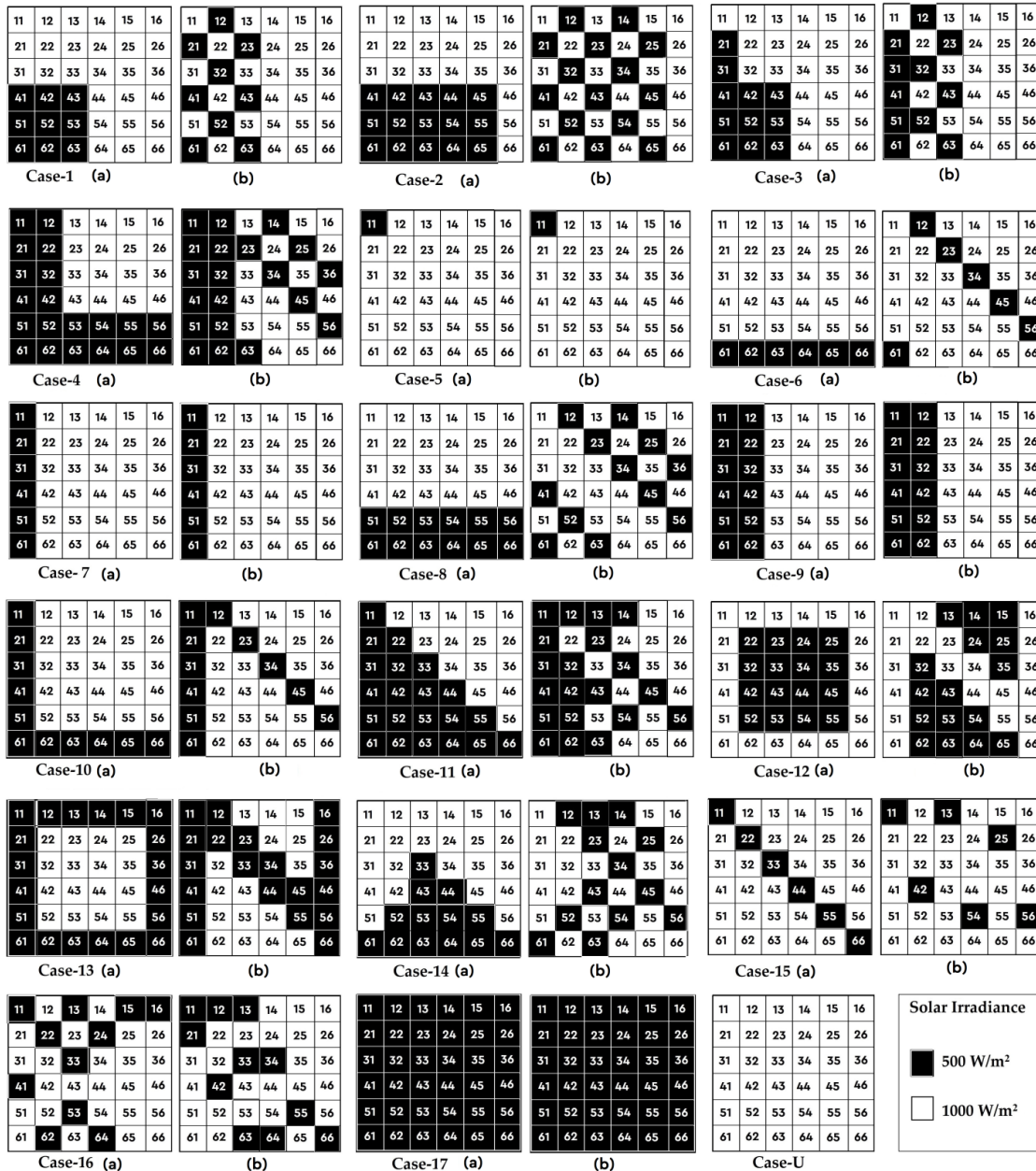


Figure 7. Shade dispersion analysis in a 6×6 array under various shadings: (a) TCT (b) SD-TCT configuration

Shade Dispersion in SD-TCT under Shading Case-1 of a 6×6 Array

Any shade extends across the whole array in the proposed SD-TCT system to ensure a maximum current for every node. The shaded row modules are spread over various rows when a shade occurs over a full row, so the current entering every row is almost equal to maximum. Figure 8 explains the dispersion of the shade in the 6th-row partial shading arrangement of TCT and SD-TCT.

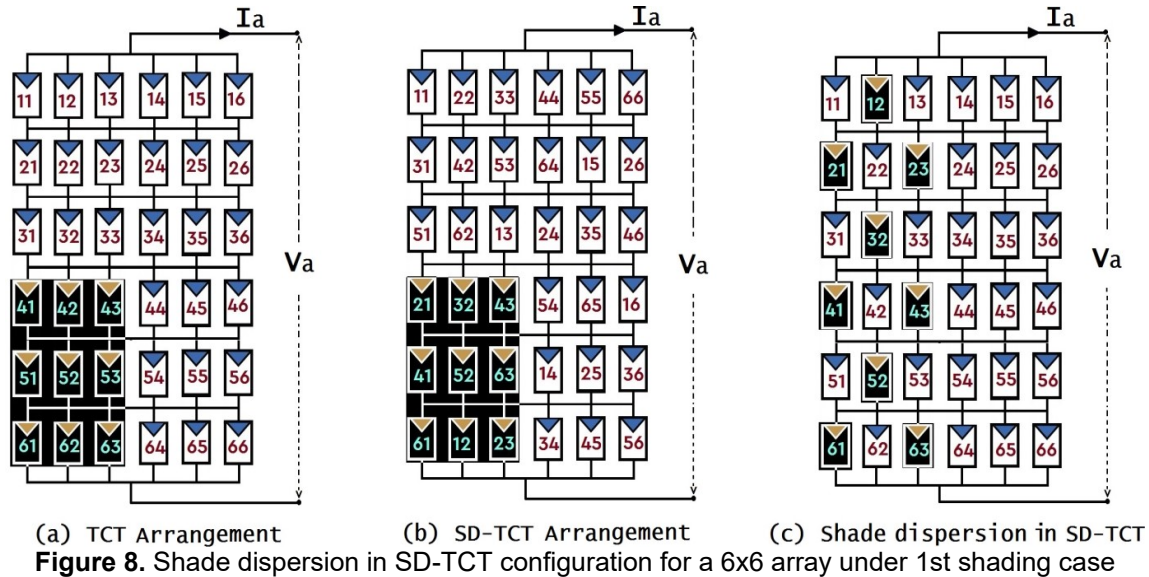


Figure 8. Shade dispersion in SD-TCT configuration for a 6x6 array under 1st shading case

Row Current Estimation

The current in rows assessment shows clear shade in the array arrangements. Moreover, by shifting the row currents, the severity of the shade can be understood clearly. The procedure for row current estimation for a 6×6 TCT under a short narrow shade sequence is given in Figure 8(a) as follows (illustrated in Figure 7: case-1 (a)).

Row Current Estimation in a 6×6 TCT Configuration under Case-1:

The generated current is expressed in equation-(7) in a 6×6 PV array depends on the solar irradiance,

$$I_{Ri} = \sum_{n=1}^6 S_{Mn} I_m = S_{M1} I_m + S_{M2} I_m + S_{M3} I_m + S_{M4} I_m + S_{M5} I_m + S_{M6} I_m \quad \dots \dots \dots (7)$$

where S_{Mn} is the shading factor of the n^{th} PV module in an array.

$$S_{M1} = \left(\frac{G_{M1}}{G_{STC}} \right), S_{M2} = \left(\frac{G_{M2}}{G_{STC}} \right), S_{M3} = \left(\frac{G_{M3}}{G_{STC}} \right), S_{M4} = \left(\frac{G_{M4}}{G_{STC}} \right), S_{M5} = \left(\frac{G_{M5}}{G_{STC}} \right), S_{M6} = \left(\frac{G_{M6}}{G_{STC}} \right) \quad \dots \dots \dots (8)$$

where I_{Ri} is the row current of the i^{th} row. I_m is the PV module's maximum current, G_{SMn} is solar irradiance at the shaded condition, and G_{STC} is irradiance at STC, *i.e.*, 1000 W/m².

The row current of the first, second, third, fourth, fifth, and sixth rows of the TCT arrangements is evaluated as given by:

$$I_{R1} = \left(6 \times \left(\frac{1000}{1000} \right) \times I_m \right) = 6 I_m = I_{R2} = I_{R3}$$

In 1st, 2nd and 3rd rows, all six modules receive full irradiance of 1000 w/m². In 4th, 5th and 6th rows, the irradiance of three modules is 500 W/m², and other three modules have 1000 W/m², as shown in Figure 6(a).

$$I_{R4} = \left(3 \times \left(\frac{1000}{1000}\right) \times I_m\right) + \left(3 \times \left(\frac{500}{1000}\right) \times I_m\right) = (3 \times 1 \times I_m) + (3 \times 0.5 \times I_m) = 4.5 I_m = I_{R5} = I_{R6}$$

Row Current Estimation in a 6×6 Proposed SD-TCT Configuration under Case-1

Compared to the TCT model, a row current assessment was also done by the number logic approach proposed. The row current for the first to the sixth row is set in the following sequence (from Figure 8(c)):

$$1^{\text{st}} \text{ row: } I_{R1} = (1 \times 0.5 \times I_m) + (5 \times 1 \times I_m) = 5.5 I_m$$

$$2^{\text{nd}} \text{ row: } I_{R2} = (2 \times 0.5 \times I_m) + (4 \times 1 \times I_m) = 5 I_m$$

$$3^{\text{rd}} \text{ row: } I_{R3} = (1 \times 0.5 \times I_m) + (5 \times 1 \times I_m) = 5.5 I_m$$

$$4^{\text{th}} \text{ row: } I_{R4} = (2 \times 0.5 \times I_m) + (4 \times 1 \times I_m) = 5 I_m$$

$$5^{\text{th}} \text{ row: } I_{R5} = (1 \times 0.5 \times I_m) + (5 \times 1 \times I_m) = 5.5 I_m$$

$$6^{\text{th}} \text{ row: } I_{R6} = (2 \times 0.5 \times I_m) + (4 \times 1 \times I_m) = 5 I_m$$

Row Current Estimation in a 6×6 Proposed SD-TCT Configuration under Cases-1 to 17:

Similarly by using the equation-(7), the row currents in a 6×6, 6×5 and 5×6 arrays are calculated under proposed 17 different shading cases (illustrated in Figures-7, 9 and 10). The calculated theoretical values of voltage, current and power for a 6×6 array TCT and SD-TCT configuration are tabulated in Table 4. In Table 4, IR is the PV modules row current that is gradually being bypassed.

Table 4. Theoretical calculations of V, I and P for a 6×6 array TCT and SD-TCT configurations

TCT Configuration			SD-TCT Configuration			Highest power: P (×V _m I _m)	Best Configuration
Row maximum currents: I _R (× I _m)	Available Voltage: V (× V _m)	Power: P (×V _m I _m)	Row maximum currents: I _R (× I _m)	Available Voltage: V (× V _m)	Power: P (×V _m I _m)		
Case-U							
I _{R1} = 6	6	36	I _{R1} = 6	6	36	36	TCT/ SD-TCT
I _{R2} = 6	5	30	I _{R2} = 6	5	30		
I _{R3} = 6	4	24	I _{R3} = 6	4	24		
I _{R4} = 6	3	18	I _{R4} = 6	3	18		
I _{R5} = 6	2	12	I _{R5} = 6	2	12		
I _{R6} = 6	1	6	I _{R6} = 6	1	6		
Case-1							
I _{R6} = 4.5	6	27	I _{R6} = 5	6	30	30	SD-TCT
I _{R5} = 4.5	5	22.5	I _{R4} = 5	5	25		
I _{R4} = 4.5	4	18	I _{R2} = 5	4	20		
I _{R3} = 6	3	18	I _{R5} = 5.5	3	16.5		
I _{R2} = 6	2	12	I _{R3} = 5.5	2	11		
I _{R1} = 6	1	6	I _{R1} = 5.5	1	5.5		

<u>Case-2</u>						
$I_{R6}= 3.5$	6	21	$I_{R6}= 4.5$	6	27	
$I_{R5}= 3.5$	5	17.5	$I_{R4}= 4.5$	5	22.5	
$I_{R4}= 3.5$	4	14	$I_{R2}= 4.5$	4	18	27
$I_{R3}= 6$	3	18	$I_{R5}= 5$	3	15	SD-TCT
$I_{R2}= 6$	2	12	$I_{R3}= 5$	2	10	
$I_{R1}= 6$	1	6	$I_{R1}= 5$	1	5	
<u>Case-3</u>						
$I_{R6}= 4.5$	6	27	$I_{R6}= 5$	6	30	
$I_{R5}= 4.5$	5	22.5	$I_{R5}= 5$	5	25	
$I_{R4}= 4.5$	4	18	$I_{R4}= 5$	4	20	30
$I_{R3}= 5.5$	3	16.5	$I_{R3}= 5$	3	15	SD-TCT
$I_{R2}= 5.5$	2	11	$I_{R2}= 5$	2	10	
$I_{R1}= 6$	1	6	$I_{R1}= 5.5$	1	5.5	
<u>Case-4</u>						
$I_{R6}= 3$	6	18	$I_{R3}= 4$	6	24	
$I_{R5}= 3$	5	15	$I_{R2}= 4$	5	20	
$I_{R4}= 5$	4	20	$I_{R1}= 4.5$	4	18	24
$I_{R3}= 5$	3	15	$I_{R6}= 4.5$	3	13.5	SD-TCT
$I_{R2}= 5$	2	10	$I_{R5}= 4.5$	2	9	
$I_{R1}= 5$	1	5	$I_{R4}= 4.5$	1	4.5	
<u>Case-5</u>						
$I_{R1}= 5.5$	6	33	$I_{R1}= 5.5$	6	33	
$I_{R2}= 6$	5	30	$I_{R2}= 6$	5	30	
$I_{R3}= 6$	4	24	$I_{R3}= 6$	4	24	33
$I_{R4}= 6$	3	18	$I_{R4}= 6$	3	18	TCT/ SD-TCT
$I_{R5}= 6$	2	12	$I_{R5}= 6$	2	12	
$I_{R6}= 6$	1	6	$I_{R6}= 6$	1	6	
<u>Case-6</u>						
$I_{R6}= 3$	6	18	$I_{R6}= 5.5$	6	33	
$I_{R5}= 6$	5	30	$I_{R5}= 5.5$	5	27.5	
$I_{R4}= 6$	4	24	$I_{R4}= 5.5$	4	22	33
$I_{R3}= 6$	3	18	$I_{R3}= 5.5$	3	16.5	SD-TCT
$I_{R2}= 6$	2	12	$I_{R2}= 5.5$	2	11	
$I_{R1}= 6$	1	6	$I_{R1}= 5.5$	1	5.5	
<u>Case-7</u>						
$I_{R6}= 5.5$	6	33	$I_{R6}= 5.5$	6	33	
$I_{R5}= 5.5$	5	27.5	$I_{R5}= 5.5$	5	27.5	
$I_{R4}= 5.5$	4	22	$I_{R4}= 5.5$	4	22	33
$I_{R3}= 5.5$	3	16.5	$I_{R3}= 5.5$	3	16.5	TCT/ SD-TCT
$I_{R2}= 5.5$	2	11	$I_{R2}= 5.5$	2	11	
$I_{R1}= 5.5$	1	5.5	$I_{R1}= 5.5$	1	5.5	
<u>Case-8</u>						
$I_{R6}= 3$	6	18	$I_{R6}= 5$	6	30	
$I_{R5}= 3$	5	15	$I_{R5}= 5$	5	25	
$I_{R4}= 6$	4	24	$I_{R4}= 5$	4	20	30
$I_{R3}= 6$	3	18	$I_{R3}= 5$	3	15	SD-TCT
$I_{R2}= 6$	2	12	$I_{R2}= 5$	2	10	
$I_{R1}= 6$	1	6	$I_{R1}= 5$	1	5	
<u>Case-9</u>						
$I_{R6}= 5$	6	30	$I_{R6}= 5$	6	30	
$I_{R5}= 5$	5	25	$I_{R5}= 5$	5	25	
$I_{R4}= 5$	4	20	$I_{R4}= 5$	4	20	30
						TCT/

$I_{R3}=5$	3	15	$I_{R3}=5$	3	15		SD-TCT
$I_{R2}=5$	2	10	$I_{R2}=5$	2	10		
$I_{R1}=5$	1	5	$I_{R1}=5$	1	5		
Case-10							
$I_{R6}=3$	6	18	$I_{R1}=5$	6	30		
$I_{R5}=5.5$	5	27.5	$I_{R2}=5$	5	25		
$I_{R4}=5.5$	4	22	$I_{R3}=5$	4	20	30	SD-TCT
$I_{R3}=5.5$	3	16.5	$I_{R4}=5$	3	15		
$I_{R2}=5.5$	2	11	$I_{R5}=5$	2	10		
$I_{R1}=5.5$	1	5.5	$I_{R6}=5.5$	1	5.5		
Case-11							
$I_{R6}=3$	6	18	$I_{R5}=4$	6	24		
$I_{R5}=3.5$	5	17.5	$I_{R4}=4$	5	20		
$I_{R4}=4$	4	16	$I_{R1}=4$	4	16	24	SD-TCT
$I_{R3}=4.5$	3	13.5	$I_{R6}=4.5$	3	13.5		
$I_{R2}=5$	2	10	$I_{R3}=4.5$	2	9		
$I_{R1}=5.5$	1	5.5	$I_{R2}=5$	1	5		
Case-12							
$I_{R2}=4$	6	24	$I_{R6}=4$	6	24		
$I_{R3}=4$	5	20	$I_{R5}=4.5$	5	22.5		
$I_{R4}=4$	4	16	$I_{R1}=4.5$	4	18	24	TCT/ SD-TCT
$I_{R5}=4$	3	12	$I_{R4}=5$	3	15		
$I_{R6}=6$	2	12	$I_{R3}=5$	2	10		
$I_{R1}=6$	1	6	$I_{R2}=5$	1	2		
Case-13							
$I_{R1}=3$	6	18	$I_{R4}=4$	6	24		
$I_{R6}=3$	5	15	$I_{R3}=4$	5	20		
$I_{R5}=5$	4	20	$I_{R2}=4$	4	16		
$I_{R4}=5$	3	15	$I_{R1}=4.5$	3	13.5	24	SD-TCT
$I_{R3}=5$	2	10	$I_{R5}=4.5$	2	9		
$I_{R2}=5$	1	5	$I_{R6}=5$	1	5		
Case-14							
$I_{R6}=3$	6	18	$I_{R5}=4.5$	6	27		
$I_{R5}=4$	5	20	$I_{R1}=4.5$	5	22.5		
$I_{R4}=5$	4	20	$I_{R2}=5$	4	20	27	SD-TCT
$I_{R3}=5.5$	3	16.5	$I_{R4}=5$	3	15		
$I_{R2}=6$	2	12	$I_{R6}=5$	2	10		
$I_{R1}=6$	1	6	$I_{R3}=5.5$	1	5.5		
Case-15							
$I_{R6}=5.5$	6	33	$I_{R1}=5$	6	30		
$I_{R5}=5.5$	5	27.5	$I_{R5}=5$	5	25		
$I_{R4}=5.5$	4	22	$I_{R4}=5.5$	4	22	33	TCT
$I_{R3}=5.5$	3	16.5	$I_{R2}=5.5$	3	16.5		
$I_{R2}=5.5$	2	11	$I_{R3}=6$	2	12		
$I_{R1}=5.5$	1	5.5	$I_{R6}=6$	1	6		
Case-16							
$I_{R1}=4$	6	24	$I_{R6}=4.5$	6	27		
$I_{R2}=5$	5	25	$I_{R1}=4.5$	5	22.5		
$I_{R6}=5$	4	20	$I_{R3}=5$	4	20		
$I_{R5}=5.5$	3	16.5	$I_{R5}=5.5$	3	16.5	27	SD-TCT
$I_{R4}=5.5$	2	11	$I_{R4}=5.5$	2	11		
$I_{R3}=5.5$	1	5.5	$I_{R2}=5.5$	1	5.5		
Case-17							

$I_{R6}=3$	6	18	$I_{R6}=3$	6	18	18	TCT/ SD-TCT
$I_{R5}=3$	5	15	$I_{R5}=3$	5	15		
$I_{R4}=3$	4	12	$I_{R4}=3$	4	12		
$I_{R3}=3$	3	9	$I_{R3}=3$	3	9		
$I_{R2}=3$	2	6	$I_{R2}=3$	2	6		
$I_{R1}=3$	1	3	$I_{R1}=3$	1	3		

Shading Cases for a 5x6 Array

The shading cases considered for analyzing the shade dispersion in a 5x6 SD-TCT array configuration are illustrated in Figure 9. Figure 9 (a) represents the shading pattern in TCT array connection and 9(b) represents the shade dispersion in SD-TCT arrangement with number logic approach. In non-shading case, *i.e.*, case-U, 30 modules in a 6x5 PV array receive full irradiance at STC of 1000 W/m².

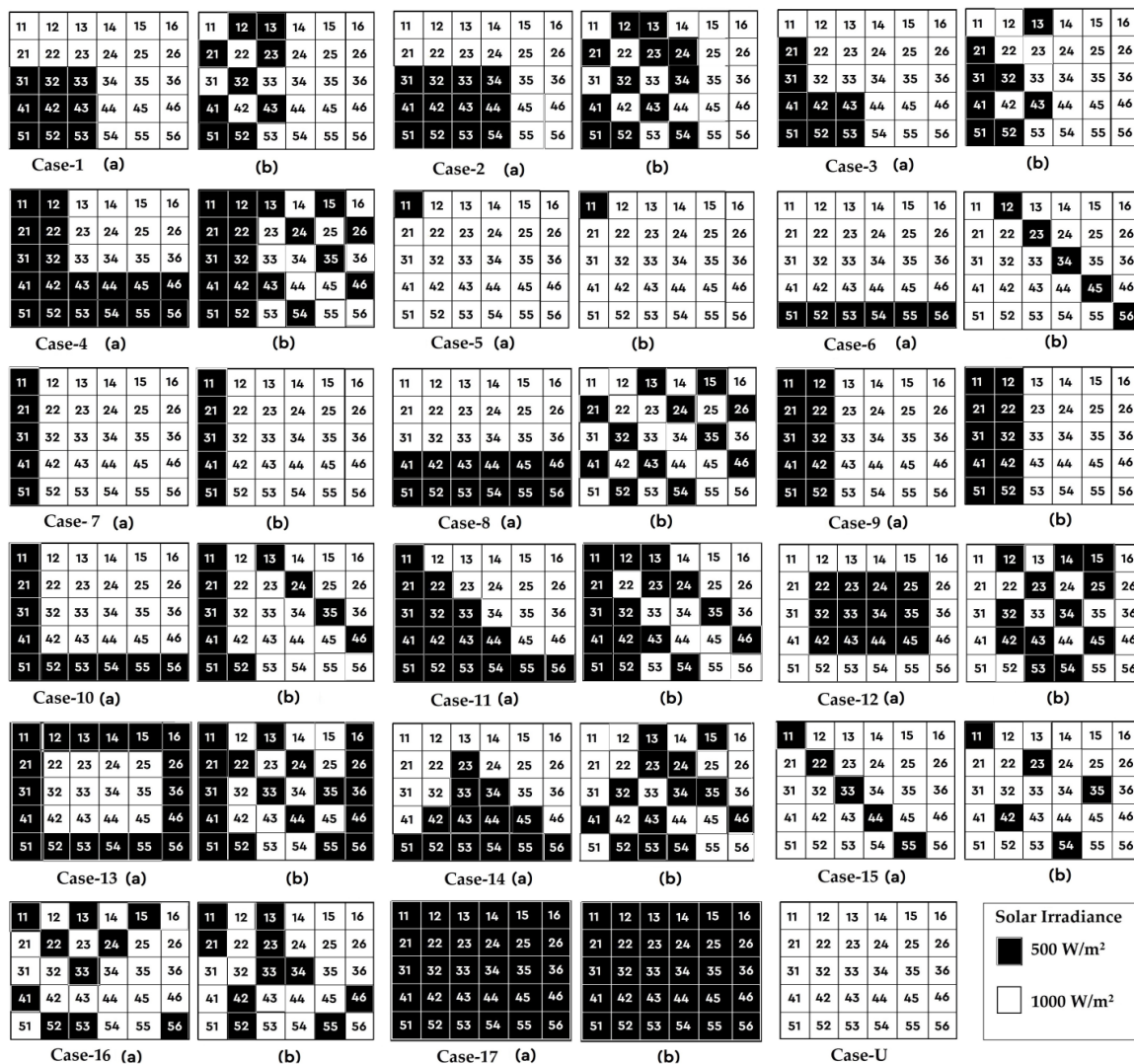


Figure 9. Shade dispersion analysis in a 5x6 array under various shadings:
(a) TCT (b) SD-TCT configuration

Shading Cases for a 6x5 Array

Shading cases for shadow dispersion analysis in a 6x5 SD-TCT configuration are shown in Figure 10. Figure 10(a) represents the shading pattern in TCT array connection,

and 10(b) represents the shade dispersion in SD-TCT arrangement with a number logic approach as explained in the formation of the SD-TCT section. In un-shading case, *i.e.*, case-U, 30 modules in a 6×5 PV array receive full irradiance at STC is 1000 W/m².

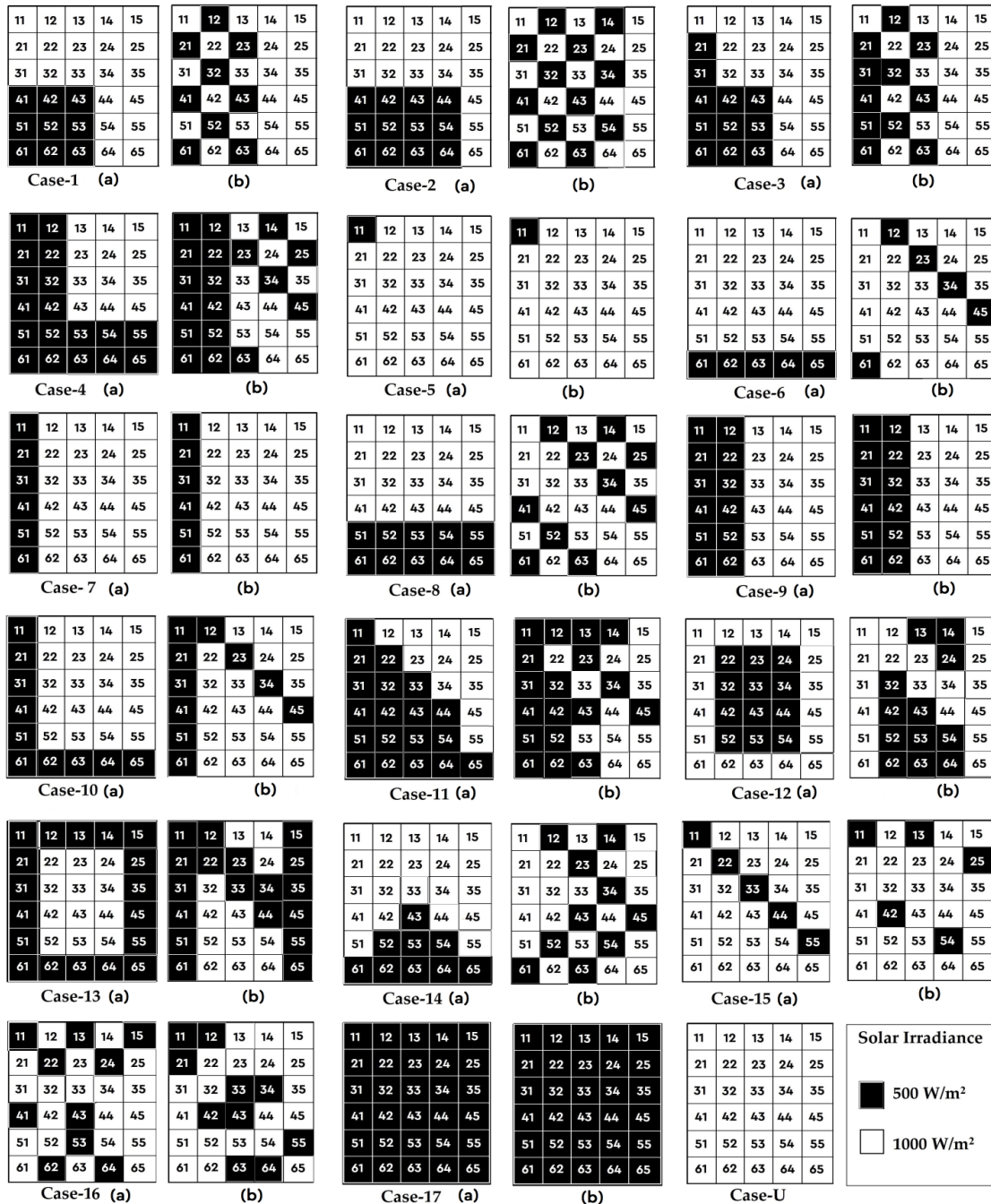


Figure 10. Shade dispersion analysis in a 6x5 array under various shadings: (a) TCT (b) SD-TCT configuration

Suppose considering case-6, PV modules in the sixth row of a 6×5 TCT array are partially shaded with an irradiance of 500 W/m² and other five rows are fully illuminated on sun irradiance as elaborated in Figure-10:case-6(a). The shaded modules in the 6th row are physically moved within a column based on the shade dispersion number logic approach, but electrical wiring is unchanged, as shown in Figure-10:case-6(b). The 6th-row modules in 61 to 66 are shaded in the TCT array and the proposed SD-TCT

arrangement provides shaded modules 61, 12, 23, 34, 45, which are positioned in different rows in a 6×5 PV array and thus shades are spread in an SD-TCT arrangement throughout the PV array. In the same way, shadows are spread in the entire PV array system for other cases.

Results and Discussion

Performance Analysis

To evaluate the performance of 6×6, 6×5 and 5×6 array size SP, TCT and proposed SD-TCT arrangements, three factors including Global Maximum Power Point (GMPP), mismatch losses (ML), % power improvement in SD-TCT under different shading cases are considered in this paper, which are displayed in Figures 7, 9 and 10, respectively. The ML exists between the parameters of the PV module under SC, as the modules obtain different intensities of solar radiation. ML is the distinction between the received peak power in the un-shaded case with an irradiance of 1000W/m² (GMPP_{uni}) and the maximum power under various shadings (GMPP_{SCs}).

$$\text{Mismatch losses}(ML) = GMPP_{uni} - GMPP_{SCs} \quad \text{--- (8)}$$

$$\text{Power improvement in SD - TCT (\%)} = \frac{GMPP_{SD.TCT} - GMPP_{TCT}}{GMPP_{SD.TCT}} \quad \text{--- (9)}$$

- Where, *GMPP* = Global maximum power point in watts(W)
ML = Mismatch Losses in watts(W)
GMPP_{uni} = GMPP at Uniform irradiance of 1000 W/m² in watts(W)
GMPP_{SCs} = GMPP at different shading conditions in watts(W)
GMPP_{SD.TCT} = GMPP of SD-TCT type of array configuration in watts(W)
GMPP_{TCT} = GMPP of TCT type of array configuration in watts(W)
SD - TCT = Shaded Dispersion Based TCT configuration.

Table 5. GMPP and ML of a 6×6 array size configurations

Cases	6×6 array configurations						Minimum ML (W)	Best Configuration
	S-P		T-C-T		SD- TCT			
	GMPP (W)	ML (W)	GMPP (W)	ML (W)	GMPP (W)	ML (W)		
U	9620	0	9620	0	9620	0	0	ALL
1	7384	2236	7714	1906	8309	1311	1311	Proposed
2	5979	3641	6155	3465	7513	2107	2107	Proposed
3	7359	2261	7661	1959	8128	1492	1492	Proposed
4	5208	4412	5433	4187	6815	2805	2805	Proposed
5	8869	751	9352	268	9352	268	268	TCT, Proposed
6	7974	1646	7974	1646	8834	786	786	Proposed
7	8834	786	8834	786	8834	786	786	ALL
8	6328	3292	6328	3292	8049	1571	1571	Proposed
9	8049	1571	8049	1571	8049	1571	1571	ALL
10	7350	2270	7323	2297	8128	1492	1492	Proposed
11	5190	4430	5510	4110	6853	2767	2767	Proposed
12	6617	3003	6778	2842	7057	2563	2563	Proposed
13	5346	4274	5433	4187	6752	2868	2868	Proposed
14	5422	4198	6000	3620	7660	1960	1960	Proposed

15	7974	1646	8834	786	8511	1109	786	TCT
16	6018	3602	7214	2406	7745	1875	1875	Proposed
17	4917	4703	4917	4703	4917	4703	4703	ALL

Table 6. GMPP and ML of a 6×5 array size configurations

Cases	6×5 array configurations						Minimum ML (W)	Best Configuration
	S-P		T-C-T		SD-TCT			
	GMPP (W)	ML (W)	GMPP (W)	ML (W)	GMPP (W)	ML (W)		
U	8017	0	8017	0	8017	0	0	ALL
1	5792	2225	6048	1969	6685	1332	1332	Proposed
2	5094	2923	5263	2754	6445	1572	1572	Proposed
3	5763	2254	6005	2012	6518	1499	1499	Proposed
4	4301	3716	4511	3506	5307	2710	2710	Proposed
5	7307	710	7716	301	7716	301	301	TCT, Proposed
6	6645	1372	6645	1372	7307	710	710	Proposed
7	7231	786	7231	786	7231	786	786	ALL
8	5273	2744	5273	2744	6597	1420	1420	Proposed
9	6445	1572	6445	1572	6445	1572	1572	ALL
10	6022	1995	5994	2023	6597	1420	1420	Proposed
11	4291	3726	4566	3451	5200	2817	2817	Proposed
12	5760	2257	5907	2110	6049	1968	1968	Proposed
13	4302	3715	4511	3506	5228	2789	2789	Proposed
14	4898	3119	5244	2773	6686	1331	1331	Proposed
15	6645	1372	7307	710	6990	1027	710	TCT
16	4864	3153	6190	1827	6597	1420	1420	Proposed
17	4097	3920	4097	3920	4097	3920	3920	ALL

Table 7. GMPP and ML of a 5×6 array size configurations

Cases	5×6 array configurations						Minimum ML (W)	Best Configuration
	S-P		T-C-T		SD-TCT			
	GMPP (W)	ML (W)	GMPP (W)	ML (W)	GMPP (W)	ML (W)		
U	8011	0	8011	0	8011	0	0	ALL
1	6137	1874	6340	1671	6783	1228	1228	Proposed
2	5529	2482	5699	2312	6307	1704	1704	Proposed
3	6135	1876	6459	1552	6871	1140	1140	Proposed
4	4322	3689	4473	3538	5549	2462	2462	Proposed
5	7386	625	7763	248	7763	248	248	TCT, Proposed
6	6365	1646	6365	1646	7096	915	915	Proposed
7	7357	654	7357	654	7357	654	654	ALL
8	4531	3480	4719	3292	6307	1704	1704	Proposed
9	6703	1308	6703	1308	6703	1308	1308	ALL
10	5868	2143	5845	2166	6703	1308	1308	Proposed
11	4348	3663	4651	3360	5754	2257	2257	Proposed
12	5529	2482	5699	2312	6307	1704	1704	Proposed
13	4322	3689	4473	3538	5549	2462	2462	Proposed
14	4450	3561	4733	3278	6210	1801	1801	Proposed
15	6434	1577	7357	654	7357	654	654	TCT, Proposed
16	5377	2634	6515	1496	6703	1308	1308	Proposed

17	4096	3915	4096	3915	4096	3915	3915	ALL
----	------	------	------	------	------	------	------	-----

Table 8. Power improvement in SD-TCT compared to SP and TCT array configurations

Cases	6×6 SPV array			6×5 SPV array			5×6 SPV array		
	SD-TCT Configuration:	% Power improvement in SD-TCT compared to		SD-TCT Configuration:	% Power improvement in SD-TCT compared to		SD-TCT Configuration:	% Power improvement in SD-TCT compared to	
		GMPP (W)	S-P		T-C-T	GMPP (W)		S-P	T-C-T
U	9620	0	0	8017	0	0	8011	0	0
1	8309	11.13	7.16	6685	13.35	9.52	6783	9.52	6.53
2	7513	20.41	18.07	6445	20.96	18.33	6307	12.33	9.64
3	8128	9.46	5.74	6518	11.58	7.87	6871	10.71	5.99
4	6815	23.58	20.27	5307	18.95	14.99	5549	22.11	19.39
5	9352	5.16	0	7716	5.81	0	7763	4.85	0
6	8834	9.73	9.73	7307	9.05	9.05	7096	10.30	10.30
7	8834	0	0	7231	0	0	7357	0	0
8	8049	21.38	21.38	6597	20.06	20.06	6307	28.15	25.17
9	8049	0	0	6445	0	0	6703	0	0
10	8128	9.57	9.90	6597	8.71	9.14	6703	12.45	12.80
11	6853	24.26	19.59	5200	17.48	12.19	5754	24.43	19.16
12	7057	6.23	3.95	6049	4.77	2.34	6307	12.33	9.64
13	6752	20.82	19.53	5228	17.71	13.71	5549	22.11	19.39
14	7660	29.21	21.67	6686	26.74	21.56	6210	28.34	23.78
15	8511	6.30	-3.79	6990	4.93	-4.53	7357	12.54	0
16	7745	22.29	6.85	6597	26.26	6.16	6703	19.78	2.80
17	4917	0	0	4097	0	0	4096	0	0

The findings of the simulation can be inferred:

- Under full irradiance on the PV array (case-U), the global maximum powers are 9620 W, 8017 W, and 8011 W for 6×6, 6×5, and 5×6 array SP, TCT, and proposed SD-TCT configurations, respectively.
- In shading cases-7, 9 and 17: All types of configurations have similar GMPP and minimum ML.
- The TCT and SD-TCT arrangements of power outputs are the same as the shading case-5.
- In 6×6, 6×5, and 5×6 size solar PV arrays, the proposed SD-TCT type of configuration has the highest GMPP's and minimum mismatch losses (ML) in most of the shading cases except in diagonal shape partial shading case-15.
- Compared with the SP and TCT arrangement, the power of SD-TCT has been enhanced, except for the shading cases 5, 7, 9 and 17.

Performance Characteristics of Array Configurations

Figures 11, 12 and 13 show P-V characteristics of 6×6, 6×5, and 5×6 array SD-TCT arrangements under different shading cases. The results find that the performance of a proposed SD-TCT is superior to other types of arrangements.

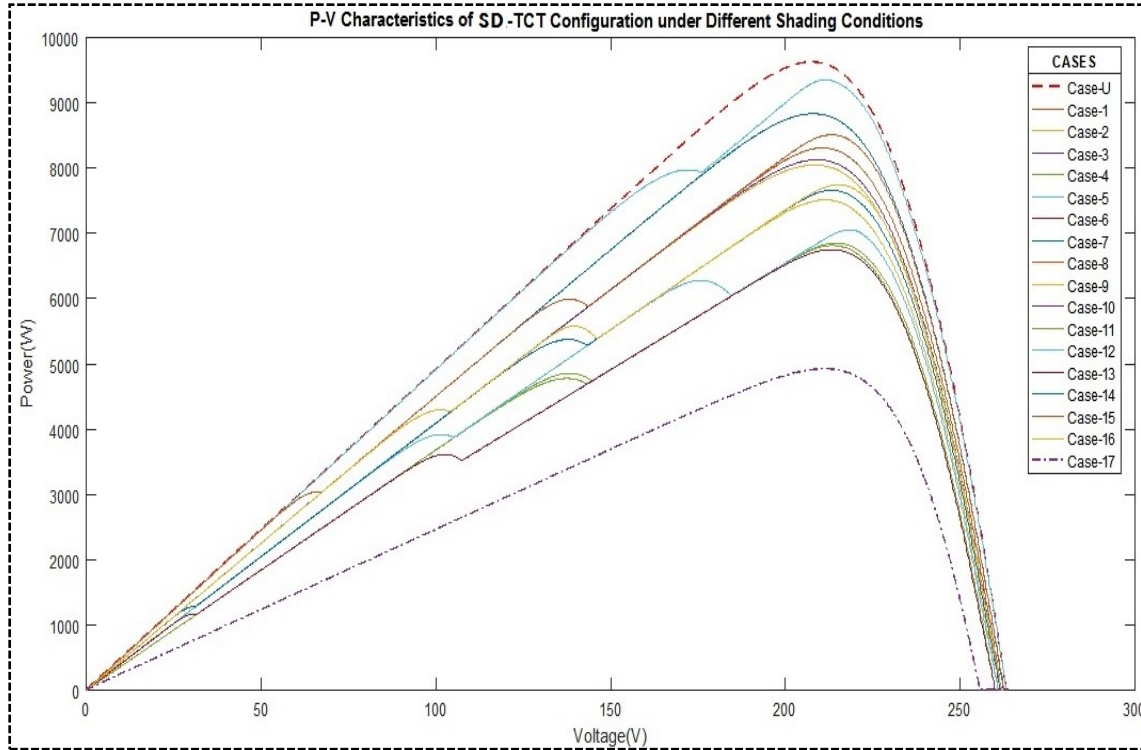


Figure 11. P-V characteristics for 6×6 array size proposed SD-TCT configurations

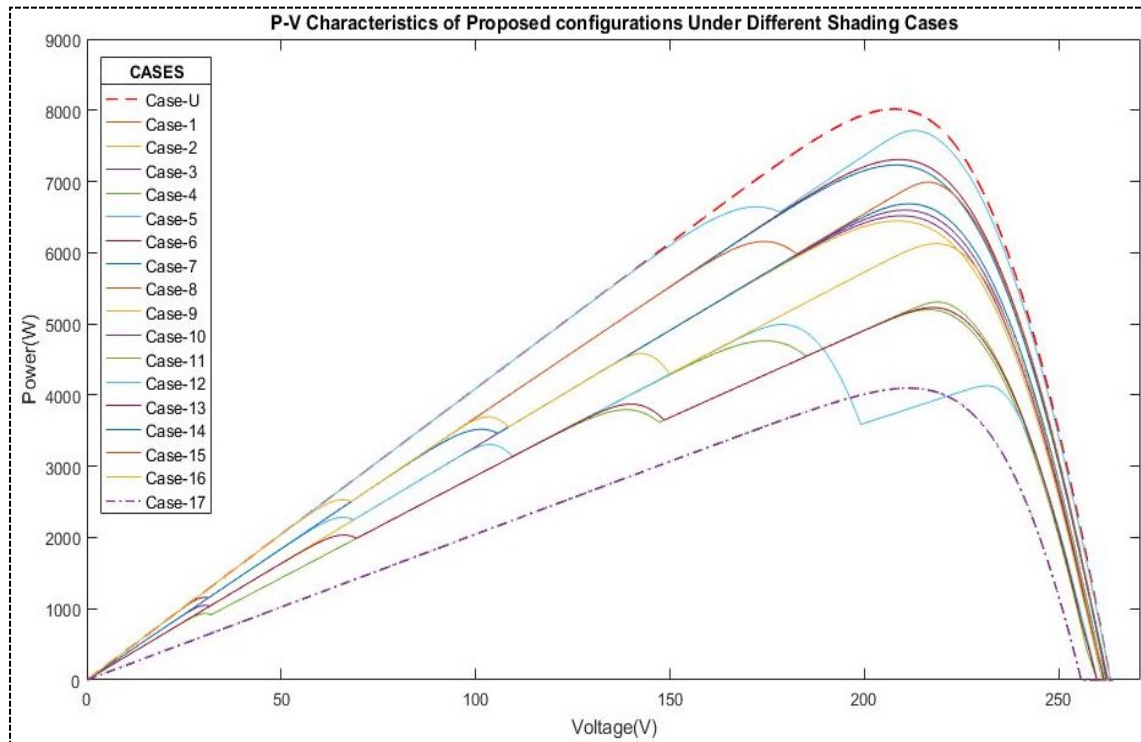


Figure 12. P-V characteristics for 6×5 array size proposed SD-TCT configurations

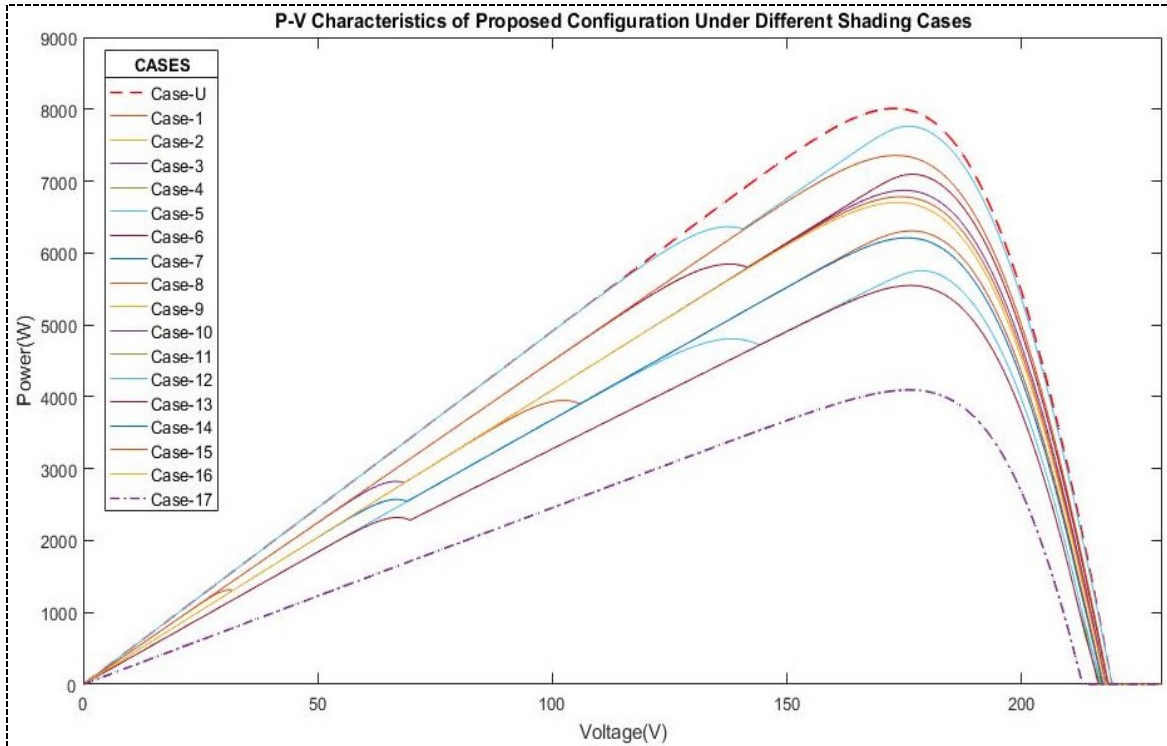


Figure 13. P-V characteristics for 5x6 array size proposed SD-TCT configurations

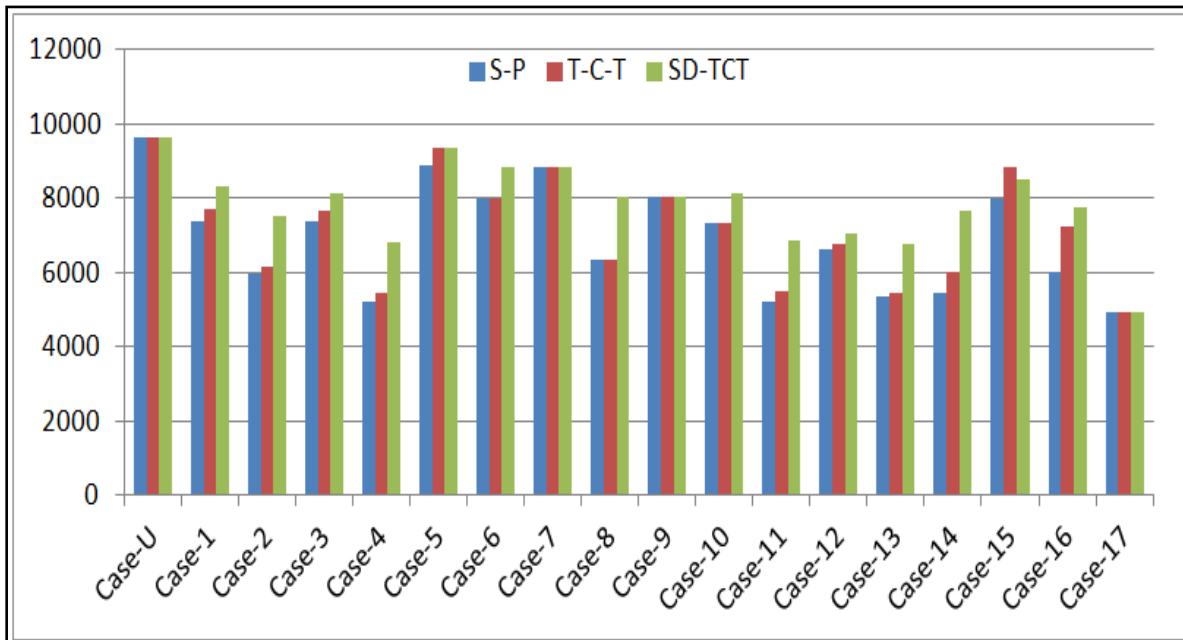


Figure 14. Comparison of GMPP's under different shading cases in 6x6 array size configurations

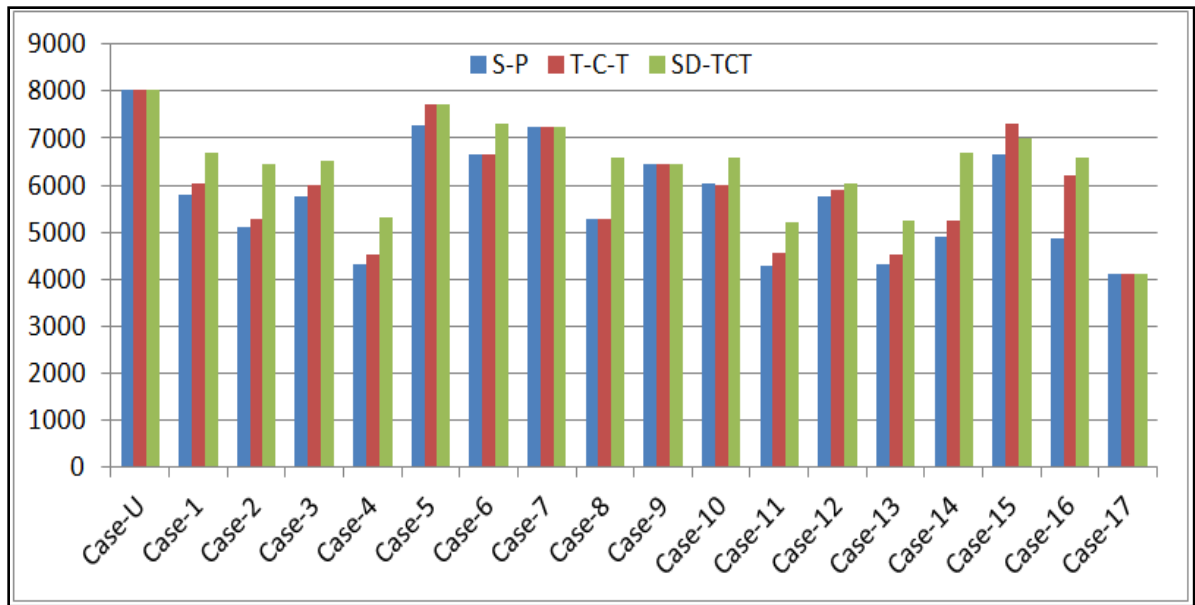


Figure 15. Comparison of GMPP's under different shading cases in 6×5 array size configurations

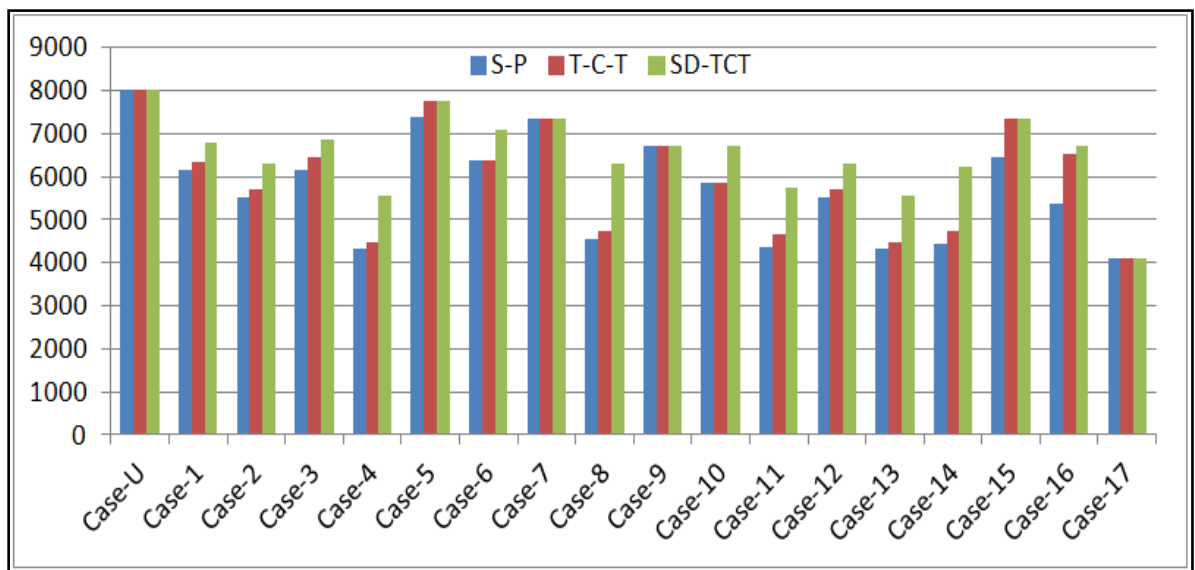


Figure 16. Comparison of GMPP's under different shading cases in 5×6 array size configurations

CONCLUSIONS

In order to optimize the solar PV power in a particular shading cases, this work implements a wide shading effect distribution technique across the array size range of $i \times j$ ($i = j$ and $i \neq j$, where i is row number and j is column number). The physical position of modules for each shading case, without any change in the electric connection, shall only be changed in the proposed method once at the time of the installation. The proposed SD-TCT configuration is cost-effective and easy for implementing a large PV farm in real time, as there are not too many switches and sensors required here. The power provided by SD-TCT is always more than the SP and TCT configuration.

Conflict of Interest

The authors declare that there is no conflict of interests regarding the publication of this paper.

REFERENCES

- [1] Roy Chowdhury, S., and Saha, H. (2010). Maximum power point tracking of partially shaded solar photovoltaic arrays. *Solar Energy Materials and Solar Cells*, 94(9), 1441-1447. DOI: 10.1016/j.solmat.2010.04.011
- [2] Kaushika, N. D., and Gautam, N. K. (2003). Energy yield simulations of interconnected solar PV arrays. *IEEE Transactions on Energy Conversion*, 18(1), 127-134. DOI: 10.1109/TEC.2002.805204
- [3] Karatepe, E., Boztepe, M., and Çolak, M. (2007). Development of a suitable model for characterizing photovoltaic arrays with shaded solar cells. *Solar Energy*, 81(8), 977-992. DOI: 10.1016/j.solener.2006.12.001
- [4] Hernández, J., Garcia, O., and Jurado, F. (2012). Photovoltaic devices under partial shading conditions. *International Review on Modelling and Simulations*, 5, 414-425.
- [5] Patel, H., and Agarwal, V. (2008). MATLAB-Based Modeling to Study the Effects of Partial Shading on PV Array Characteristics. *IEEE Transactions on Energy Conversion*, 23(1), 302-310. DOI: 10.1109/TEC.2007.914308
- [6] Bidram, A., Davoudi, A., and Balog, R. S. (2012). Control and Circuit Techniques to Mitigate Partial Shading Effects in Photovoltaic Arrays. *IEEE Journal of Photovoltaics*, 2(4), 532-546. DOI: 10.1109/JPHOTOV.2012.2202879
- [7] Vijayalekshmy, S., Rama Iyer, S., and Beevi, B. (2015). Comparative Analysis on the Performance of a Short String of Series-Connected and Parallel-Connected Photovoltaic Array Under Partial Shading. *Journal of The Institution of Engineers (India): Series B*, 96(3), 217-226. DOI: 10.1007/s40031-014-0143-7
- [8] Belhachat, F., and Larbes, C. (2015). Modeling, analysis and comparison of solar photovoltaic array configurations under partial shading conditions. *Solar Energy*, 120, 399-418. DOI: 10.1016/j.solener.2015.07.039
- [9] Wang, Y.-J., and Hsu, P.-C. (2011). An investigation on partial shading of PV modules with different connection configurations of PV cells. *Energy*, 36(5), 3069-3078. DOI: 10.1016/j.energy.2011.02.052
- [10] BALARAJU, V., and Chengaiah, C. (2020). A Comprehensive Study on Re-arrangement of Modules Based TCT Configurations of Partial Shaded PV Array with Shade Dispersion Method. *Trends in Renewable Energy*, 6, 37-60. DOI: 10.17737/tre.2020.6.1.00111
- [11] Rani, B. I., Ilango, G. S., and Nagamani, C. (2013). Enhanced Power Generation From PV Array Under Partial Shading Conditions by Shade Dispersion Using Su

- Do Ku Configuration. *IEEE Transactions on sustainable energy*, 4(3), 594-601. DOI: 10.1109/TSTE.2012.2230033
- [12] Sahu, H. S., Nayak, S. K., and Mishra, S. (2016). Maximizing the Power Generation of a Partially Shaded PV Array. *IEEE Journal of Emerging and Selected Topics in Power Electronics*, 4(2), 626-637. DOI: 10.1109/JESTPE.2015.2498282
- [13] Raju, V.B., and Chengaiah, Ch. (2019). Performance Analysis of Conventional, Hybrid and Optimal PV Array Configurations of Partially Shaded Modules. *International Journal of Engineering and Advanced Technology*, 9(1), 3061-3073. DOI: 10.35940/ijeat.A1661.109119
- [14] Yadav, A. S., Pachauri, R. K., Chauhan, Y. K., Choudhury, S., and Singh, R. (2017). Performance enhancement of partially shaded PV array using novel shade dispersion effect on magic-square puzzle configuration. *Solar Energy*, 144, 780-797. DOI: 10.1016/j.solener.2017.01.011
- [15] Kaushika, N. D., and Gautam, N. K. (2003). Energy yield simulations of interconnected solar PV arrays. *IEEE Transactions on Energy Conversion*, 18(1), 127-134. DOI: 10.1109/TEC.2002.805204
- [16] Gautam, N. K., and Kaushika, N. D. (2002). Reliability evaluation of solar photovoltaic arrays. *Solar Energy*, 72(2), 129-141. DOI: 10.1016/S0038-092X(01)00085-8

Article copyright: © 2021 V. Bala Raju, Dr. Ch. Chengaiah. This is an open access article distributed under the terms of the [Creative Commons Attribution 4.0 International License](https://creativecommons.org/licenses/by/4.0/), which permits unrestricted use and distribution provided the original author and source are credited.



Life Cycle Assessment of A Hydrocarbon-based Electrified Cleaning Agent

Peng Liu¹, Bo Zhang^{1*}, Changyan Yang^{1,2*}, Yu Gong¹, Yinhang Qu¹, Jiayi Li¹, Bohan Yang¹, Yigang Ding¹

1: Key Laboratory for Green Chemical Process of Ministry of Education, Hubei Key Laboratory of Novel Chemical Reactor and Green Chemical Technology, School of Chemical Engineering and Pharmacy, Wuhan Institute of Technology, Hubei, China

2: Hubei Key Laboratory for Processing and Application of Catalytic Materials, Huanggang Normal University, Hubei, China

Received April 15, 2021; Accepted May 1, 2021; Published May 3, 2021

The electrified cleaning agent requires a moderate volatilization rate, low ozone-depleting substances value, non-flammable, non-explosive and other characteristics. This study performed a whole life cycle assessment on a hydrocarbon-based electrified cleaning agent. The life cycle model is cradle-to-grave, and the background data sets include power grid, transportation, high-density polyethylene, chemicals, etc. The analysis shows that the global warming potential (GWP) of the life cycle of 1 kg of electrified cleaning agent is 2.08 kg CO₂ eq, acidification potential (AP) is 9.49E-03 kg SO₂ eq, eutrophication potential (EP) is 1.18E-03 kg PO₄³⁻ eq, respirable inorganic matter (RI) is 2.13E-03 kg PM_{2.5} eq, ozone depletion potential (ODP) is 4.91E-05 kg CFC-11 eq, photochemical ozone formation potential (POFP) is 2.89E-02 kg NMVOC eq, ionizing radiation-human health potential (IRP) is 3.16E-02 kg U235 eq, ecotoxicity (ET) is 2.69E-01 CTUe, human toxicity-carcinogenic (HT-cancer) is 4.32E-08 CTUh, and human toxicity-non-carcinogenic (HT-non cancer) is 2.31E-07 CTUh. The uncertainty of the results is between 3.46-9.95%.

The four processes of tetrachloroethylene production, D40 solvent oil production, tetrachloroethylene environmental discharge during product use, and electricity usage during product disposal have substantial effects on each LCA indicator, so they are the focus of process improvement. Changes in power consumption during production and transportation distance of raw materials have little effect on total carbon emissions. Compared with the production process of single-solvent electrified cleaning agent tetrachloroethylene and n-bromopropane, the production of the electrified cleaning agent developed in this study has its own advantages in terms of carbon footprint and other environmental impact indicators. Carbon emissions mainly come from the power consumption of each process, natural gas production and combustion, and other energy materials for heating. It is recommended to use renewable raw materials instead of crude oil to obtain carbon credits based on geographical advantages, and try to use production processes with lower carbon emissions, while the exhaust gas from the traditional production process is strictly absorbed and purified before being discharged.

Keywords: D40 solvent oil; Tetrachloroethylene; Global warming potential (GWP), Acidification potential (AP); Eutrophication potential (EP); Photochemical ozone formation potential (POFP); Ecotoxicity (ET)

1. Introduction

Electrified cleaning refers to cleaning operations performed under normal working conditions with a certain voltage. It is usually required that the electrified cleaning agent must have a moderate volatilization rate (*i.e.*, not to freeze the line), low ozone-depleting substances (ODS) value, non-flammable, non-explosive and other characteristics. The electrified cleaning agent is mainly used for cleaning equipment and devices in use under high-voltage electric fields, such as locomotive substations, high-voltage substations and high-voltage lines. Traditional charged cleaning agents mostly use chlorinated hydrocarbons (*e.g.*, Freon), bromo-hydrocarbons and other halogenated hydrocarbons, which are high specific resistance reagents with high ODS value and strong volatility. They may damage the atmospheric O₃ layer, and are easy to cause the line to freeze and increase the load of the line, affecting the normal operation [1].

The eco-friendly cleaning agent for high/low voltage equipment in use developed by this study is compounded with D40 solvent oil and tetrachloroethylene with extremely low ODS value as the base liquid, supplemented by butanol and other additives, which can effectively remove soil, dirt, oil stains and animal feces on the surface of charged devices. The electrified cleaning agent has a resistance value of more than 10 G ohms, and can be used in an electric field environment of up to 100,000 volts. It is mainly used for live cleaning of high-voltage circuits, substations, electrical equipment, etc. This research conducts a full life cycle assessment of the electrified cleaning agent, including the production, use and waste recycling process of the product.

2. Definition of Objectives and Scope

2.1 Object Definition

2.1.1 Product Information

The research object of this study is: to access an electrified cleaning agent. The specific information is as follows :

Specification number : DL1006-series

Product category: Eco-environmental cleaning agent for high/low voltage live equipment (such as high voltage circuit, substation and electrical equipment). The target users of eco-environmental cleaning agents are the customers with high-voltage circuits, substations, electrical equipment and other equipment, including high-speed railways, motor vehicles, aircrafts, tanks, electrical equipment and instruments of ships.

Shape and form: solution

2.1.2 Functional Unit and Benchmark Flow

Functional unit: 1 kg product

2.1.3 Data Representation

The representation of time, geography and technology is as follows:

(1) Time representation: 2020

(2) Geographical representation: China

2.2 Scope Definitions

2.2.1. System Boundary

The system boundary of this study is from cradle to grave (from resource exploitation to waste treatment and recycle). The life process includes the production, use, recovery and waste solvent distillation of charged cleaners. Background processes include power grid, transportation, high density polyethylene for packaging, chemicals and sludge landfilling.

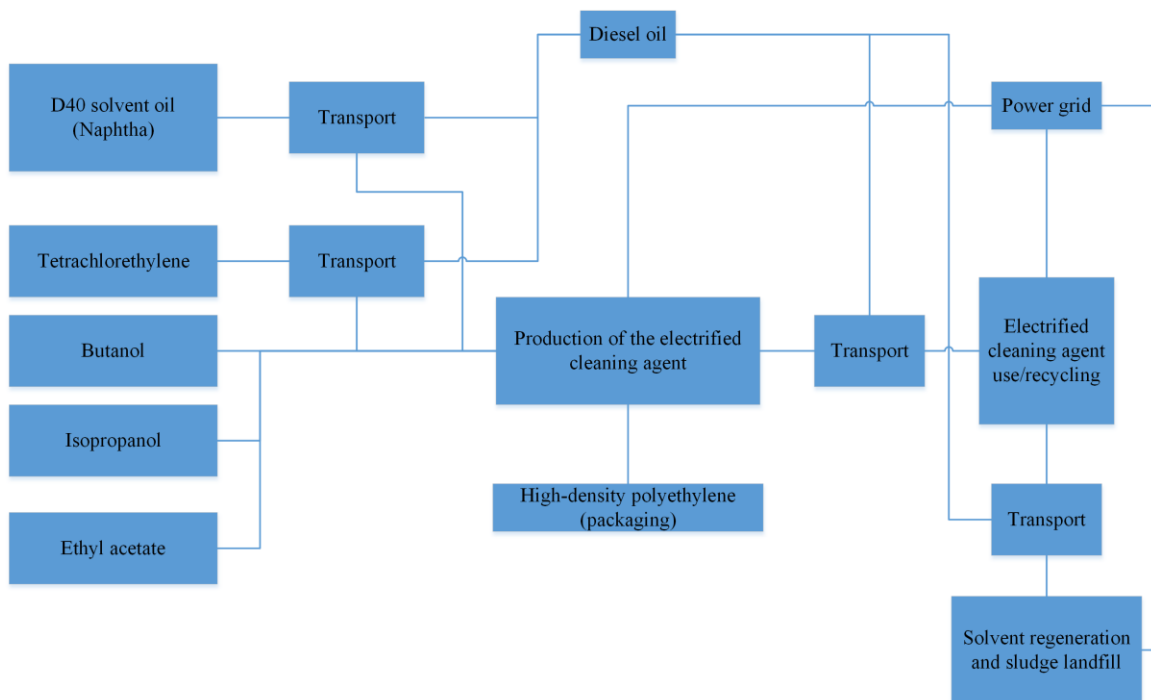


Figure. 1. System boundary of the electrified cleaning agent

2.2.2. Selection Principle

The trade-off rules used in this study are based on the weight ratio of raw material to the product weight or the total process input. Specific rules are as follows:

- (1) When the weight of ordinary material is less than 1% of the product weight and the weight of material containing rare or high purity components is less than 0.1 % of the product weight, the upstream production data of the material can be ignored. Total negligible material weight shall not exceeding 5 %.
- (2) The material can be ignored if the low value waste is used as raw materials, such as fly ash, slag, straw, garbage and other upstream production data. The production equipment, plant, living facilities and other emissions are ignored.

2.2.3 Environmental Impact Indicators

Environmental impact indicators are summarized in Table 1. Data quality represents the difference between the target representativeness of LCA research and the actual representativeness of data. The data quality evaluation method in this report adopts the CLCD method.

Table 1. Environmental impact indicators

Environmental impact indicators	Indicator unit	Main substances
Global warming potential (GWP)	kg CO ₂ eq.	CO ₂ , CH ₄ , N ₂ O...
Acidify potential (AP)	kg SO ₂ eq.	SO ₂ , NO _x , NH ₃ ...
Eutrophication potential (EP)	kg PO ₄ ³⁻ eq.	NH ₃ , NH ₄ -N, COD...
Inhalable inorganic matter (RI)	kg PM _{2.5} eq.	CO, PM ₁₀ , PM _{2.5} ...
Ozone depletion potential (ODP)	kg CFC-11 eq.	CCl ₄ , C ₂ H ₃ Cl ₃ , CH ₃ Br...
photochemical ozone formation potentials(POFP)	kg NMVOC eq.	C ₂ H ₆ , C ₂ H ₄ ...
Ionizing Radiation - Human Health	kg U235 eq.	C-14, Cs-134...
Ecotoxicity	CTUe	HF, Hg ²⁺ , Be...
Human toxicity - carcinogenic	CTUh	As, Cr, Pb...
Human toxicity - noncarcinogenic	CTUh	Hg ²⁺ , HF, TI...

Note: eq. is the abbreviation of equivalent.

2.2.4. Software and Database

In this study, the eFootprint software system was used to establish a life cycle model of charged detergents and calculate the LCA results. The eFootprint software system is an online LCA analysis software developed by IKE Environmental Technology Co., Ltd (<http://ike-global.com/>). It supports full life cycle process analysis and has built-in China Life Cycle Basic Database (CLCD), European ELCD database and Swiss Ecoinvent database.

The China Life Cycle Basic Database (CLCD) used in the research was developed by IKE, which is an industry average database based on the core model of China's basic industrial system life cycle. The CLCD database includes inventory data sets of major domestic energy, transportation and basic raw materials.

The LCA model of the electrified cleaning agent was established in eFootprint software. The background data sources of this LCA study are shown in Table 2:

Table 2. Background data source

List name	Specification model	Process	Data set name	Name database
Electricity	AR	Electrified cleaning agent 【Production】	East China Power Grid (to users)	CLCD-China-ECER 0.8
Electricity	-	Electrified cleaning agent 【use】	East China Power Grid (to users)	CLCD-China-ECER 0.8
Electricity	-	Electrified cleaning agent 【Disposal】	East China Power Grid (to users)	CLCD-China-ECER 0.8
D40 solvent oil	CP	Electrified cleaning agent 【Production】	Naphtha/Naphtha	CLCD-China-ECER 0.8
Tetrachloroethylene	AR	Electrified cleaning agent 【Production】	tetrachloroethylene production	Ecoinvent 3.1 ^[2]
Isopropanol	AR	Electrified cleaning agent 【Production】	Isopropanol (domestic)	CLCD-China-ECER 0.8
Butanol	AR	Electrified cleaning agent 【Production】	1-Butanol	Ecoinvent 3.1
Ethyl acetate	AR	Electrified cleaning agent 【Production】	Ethyl acetate	Ecoinvent 3.1
High-density polyethylene	-	Electrified cleaning agent 【Production】	High-density polyethylene	CLCD-China-ECER 0.8
Sludge landfill	-	Electrified cleaning agent 【Disposal】	Landfill of textiles	ELCD 3.0

3. Data Collection

3.1 Electrified Cleaning Agent 【Production】

(1) Basic process information

Process name: electrified cleaning agent 【production】

Process boundary: from cradle to gate

(2) Data representativeness

Main data sources: chemical process simulation, enterprise surveys. The data does not represent industry average data

Company name: Suqian Dunjia Biotechnology Co., Ltd. (Jiangsu, China)

Origin: China

Base year: 2020

Process equipment: reactors, steam generator, vacuum homogenizer, packaging machine

Main raw material: organic solvent

Main energy consumption: electricity

Production scale: 2000 t/y

Table 3 LCI Data of the electrified cleaner 【production】 process

Type	List name	Quantity	unit	Upstream data source	Use / emission reasons
Product	Electrified cleaning agent	1	kg	--	--
Raw materials	D40 solvent oil	0.64	kg	CLCD-China-ECER 0.8 ^[3]	
Raw materials	Tetrachlorethylene	0.33	kg	Ecoinvent 3.1	
Raw materials	Butanol	0.01	kg	Ecoinvent 3.1	
Raw materials	Isopropanol	0.02	kg	CLCD-China-ECER 0.8 ^[4]	
Raw materials	Ethyl acetate	3.62E-03	kg	Ecoinvent 3.1	
Raw materials	High-density polyethylene	0.02	kg	CLCD-China-ECER 0.8	
Energy	electricity	0.05	MJ	CLCD-China-ECER 0.8 ^[5]	
Environmental emissions	water vapor	8.40E-04	kg		Boiler blowdown
Environmental emissions	Suspended solids, unspecified	9.33E-05	kg		Discharge (body of water)
Environmental emissions	biological oxygen demand	0.0001	kg		Discharge (body of water)
Environmental emissions	COD	0.0001	kg		Discharge (body of water)

(3) Transportation information

Table 4. Transportation information

Material name	Gross weight	Starting point	End	Transport distance	Type of transport ^[6]
D40 solvent oil	1.1 kg	Jiangsu	Jiangsu	200 km	Truck transportation (30t)-diesel
Tetrachloroethylene	1.1 kg	Jiangsu	Jiangsu	200 km	Truck transportation (30t)-diesel

Note: In the benchmark model, only the transportation of D40 solvent oil and tetrachloroethylene, which account for the largest proportion, is considered. The upstream data sources of transportation data are all from the CLCD database.

Technical supplementary description: The production is planned to use the existing equipment of a cleaning agent company in Jiangsu Suqian Dunjia Biotechnology Co., Ltd. The strict material and energy consumption balance calculations for the production process was performed by using ASPEN Plus. Figure 2 shows the flow chart of the simulation. D40 solvent oil and tetrachloroethylene (PCE), which are main raw materials of the charged cleaner, are added to the stirred tank 1 through pumps 1 and 2 (PUMP1 and PUMP2), respectively. The material is heated to 30°C by steam and stirred at 30°C for 30 minutes. After mixing, the materials are pumped by the pump 3 to the heat

exchanger to cool to room temperature, and then enter the stirred tank 2. Butanol, isopropanol and ethyl acetate are added to the tank 2 at room temperature, and stirred for 30 minutes. Finally, the products are packed by the packaging machine and shipped.

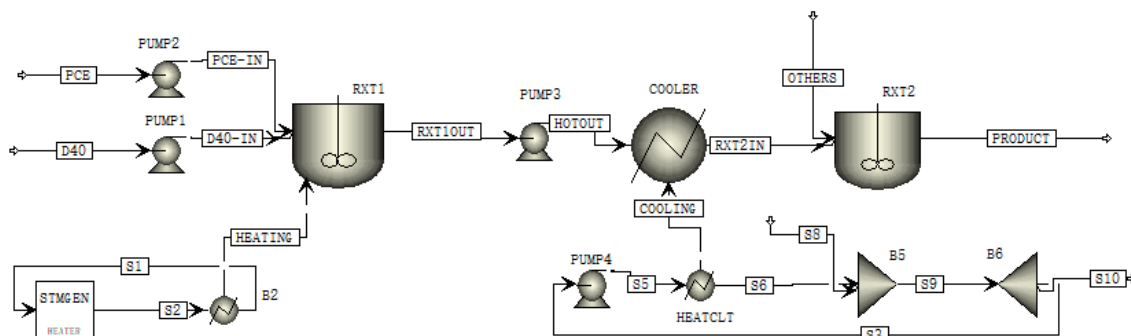


Figure 2. Electrified cleaning agent production process

3.2 Electrified Cleaning Agent 【Use】

(1) Basic Process Information

Process name: electrified cleaning agent [use]

Process boundary: from gate to use

(2) Data representativeness

Main data source: estimation of the process parameters does not represent industry average data

Origin : China

Base year: 2020

Process equipment: air gun, spray gun, condensation recovery device

Main raw material: electrified cleaning fluid

Main energy consumption: electricity

Application scale: 2000 t/y

Table 5. LCI data of the electrified cleaning agent 【use】 process

Type	List name	Quantity	Unit	Upstream data source	Use/emission reason
Energy	Electricity	0.02	MJ	CLCD-China-ECER 0.8	-
Environmental emissions	Tetrachloroethylene	0.06	kg	-	Emissions (atmosphere)
Environmental emissions	Naphtha (petroleum), hydrotreated heavy	0.13	kg	-	Emissions (atmosphere)
Environmental emissions	Butanol	0.01	kg	-	Emissions (atmosphere)
Environmental emissions	Isopropanol	0.02	kg	-	Emissions (atmosphere)
Environmental emissions	Ethyl acetate	3.62E-03	kg	-	Emissions (atmosphere)

Technical supplementary description: First, the air gun is used to remove dust from the equipment. Then, the spray gun is used to spray the charged cleaning fluid to clean the equipment. Finally, the air gun is used to evaporate the cleaning fluid, while the recycling and condensing equipment is operated to recover the solvent. In the benchmark model, it is assumed that 80% of the solvent can be recycled, *i.e.*, 20% of D40 solvent oil and tetrachloroethylene and all additives are discharged into the atmosphere.

3.3 Electrified Cleaning Agent 【Disposal】

(1) Basic process information

Process name: electrified cleaning agent 【disposal】

Process boundary: from use to grave

(2) Data representativeness

Main data sources: chemical process simulation, database. The results do not represent industry average data

Origin: China

Base year: 2020

Process equipment: distillation equipment, sludge landfill

Main raw material: Recycled electrified cleaning agent

Main energy consumption: electricity

Production scale: 2000 t/y

Technical supplementary description: A two-stage distillation device is used to rectify the waste solution to separate tetrachloroethylene and D40 solvent oil. Figure 3 is a diagram of the two-stage distillation device for waste solvents simulated in ASPEN Plus. D40 solvent oil is simulated using a mixture of 50% decane and 50% undecane, and the sludge is simulated using ethyl palmitate. The used or unclean solvents in this process (*i.e.*, detergents contain excessive soluble and non-volatile residues such as fatty acids, grease and oil) are first heated to above the boiling point of tetrachloroethylene (121°C) to recycle high-purity tetrachloroethylene (99% purity). Then, the distillate from the bottom of the tower enters the second-stage distillation tower and is heated to the boiling point of D40 mineral spirits (greater than 190°C) to volatilize and recover D40 mineral spirits. Residual impurities are left at the bottom of the kettle and become sludge due to their higher boiling point than D40 oil. Tetrachloroethylene and D40 solvent oil can be reused.

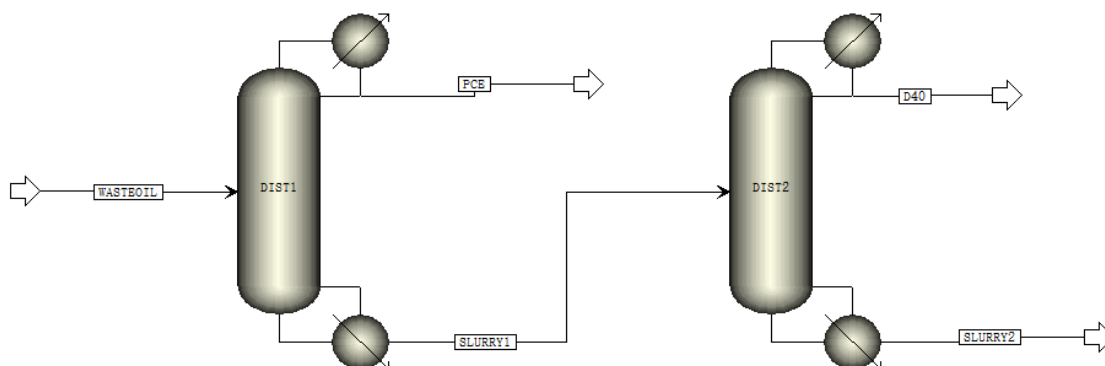


Figure 3. Design of a 2-stage distillation device for waste solvent

Table 6. Calculation results of the 2-stage distillation unit for the distillation of the waste solvent (feed rate: 1000 kg/h)

Calculation results	Distillation Tower 1 (DIST1)	Distillation Tower 2 (DIST2)
Minimum reflux ratio	0.4581	0.0112
Actual reflux ratio	1.247	0.0527
Minimum number of plates	6.6628	2.4893
Actual number of plates	10	10
Feed tray	5.6298	5.5392
Reboiler load/(MJ/h)	489.12	200.44
Condenser load/(MJ/h)	161.08	207.1
Distillate product temperature	120.95	182.17
Bottom temperature	190.91	275.68
Distillate to feed ratio	0.3064	0.9635

Table 7. Material calculation results of the waste solvent 2-stage distillation unit

Calculation results	Unit	(WAST EOIL)	(PCE)	(SLUR RY1)	Recovery of solvent oil (D40)	(SLUR RY2)
Temperature	°C	25	120.9547	190.9094	182.1664	275.6797
Pressure	bar	1	1	1.2	1	1.2
Molar enthalpy	cal/mol	-58436.548	-9450.39	-63022.5	-60376.2	-142478
Mass enthalpy	cal/gm	-372.19905	-57.0812	-411.311	-404.941	-543.247
Molar entropy	cal/mol-K	-203.01068	-44.0808	-229.724	-226.883	-334.24
Mass entropy	cal/gm-K	-1.2930329	-0.26625	-1.49927	-1.52169	-1.27441
Molar density	mol/cc	0.0055618	0.008671	0.003912	0.004053	0.002421
Mass density	gm/cc	0.8732294	1.435496	0.599471	0.604314	0.634827
Enthalpy flow	cal/sec	-107524.17	-5327.89	-80432	-74246.2	-6627.29
Average molecular weight		157.00349	165.5603	153.2235	149.0988	262.2706
Molar flow	kmol/hr	6.6240568	2.029588	4.594469	4.427016	0.167452
Mass Flow	kg/hr	1040	336.0192	703.9808	660.063	43.91784
D40 solvent oil	kg/hr	664	3.379192	660.6208	656.3036	4.317173
Tetrachloroethylene	kg/hr	336	332.64	3.36	3.359333	0.000667
Sludge	kg/hr	40	0	40	0.4	39.6
Mass ratio						
D40 solvent oil	wt%	0.6384615	0.010057	0.938407	0.994305	0.098301
Tetrachloroethylene	wt%	0.3230769	0.989943	0.004773	0.005089	1.52E-05
Sludge	wt%	0.0384615	0	0.05682	0.000606	0.901684
Volume flow	L/min	19.849689	3.901314	19.57227	18.2042	1.153013

Table 8. LCI data of electrified cleaning agent 【Disposal】

Type	List name	Quantity	Unit	Upstream/downstream data sources	Use/emission reason
Energy	Electric power	0.53	MJ	CLCD-China-ECER 0.8	Solvent distillation process
Waste to be disposed of	Sludge	0.04	kg	ELCD 3.0	Sludge landfill after solvent distillation
Renewable waste	Tetrachloroethylene	0.26	kg		Recovery and reuse after solvent distillation
Renewable waste	Naphtha (D40)	0.51	kg		Recovery and reuse after solvent distillation

4. Life Cycle Impact Analysis

4.1 LCA Results

The LCA results were modeled by the eFootprint software based on 1 kg electrified cleaning agent. The calculated indicators include global warming potential (GWP), acidification potential (AP), eutrophication potential (EP), respirable inorganic matter (RI), ozone depletion potential (ODP), photochemical ozone formation potential (POFP, also called POCP), ionizing radiation-human health potential (IRP), ecotoxicity (ET), human toxicity-carcinogenic (HT-cancer), and human toxicity-non-carcinogenic (HT-non cancer). The LCA results are as follows (Table 9).

Table 9. LCA results of electrified cleaning agent (1 kg)

Environmental impact indicators	Impact type indicator unit	LCA results
GWP	kg CO ₂ eq	2.08
AP	kg SO ₂ eq	9.49E-03
EP	kg PO ₄ ³⁻ eq	1.18E-03
RI	kg PM _{2.5} eq	2.13E-03
ODP	kg CFC-11 eq	4.91E-05
POFP	kg NMVOC eq	2.89E-02
IRP	kg U235 eq	3.16E-02
ET	CTUe	2.69E-01
HT-cancer	CTUh	4.32E-08
HT-non cancer	CTUh	2.31E-07

4.2 Analysis of Process Cumulative Contribution

The cumulative contribution of a process refers to the cumulative value of the direct contribution of the process and the contribution of all upstream processes (*i.e.*, the contribution of raw material consumption). Since the process usually contains multiple inventory data, the process contribution analysis is actually the accumulation of the sensitivity of multiple inventory data.

Table 10. Cumulative contribution results of electrified cleaning agent

Name	GWP	AP	EP	RI	ODP
Electrified cleaning agent total	2.08E+00	9.49E-03	1.18E-03	2.13E-03	4.91E-05
Electrified cleaning agent production	1.88E+00	8.13E-03	9.32E-04	1.79E-03	4.91E-05
electricity	1.27E-02	7.14E-05	4.44E-06	2.13E-05	3.25E-11
D40 solvent oil	4.37E-01	1.95E-03	2.79E-04	3.17E-04	2.42E-07
D40 solvent oil-transportation	9.62E-03	1.95E-04	3.49E-05	3.68E-05	8.26E-10
Tetrachloroethylene	1.23E+00	5.12E-03	4.45E-04	1.04E-03	4.88E-05
Tetrachloroethylene-Transport	4.87E-03	9.86E-05	1.77E-05	1.86E-05	4.18E-10
Butanol	3.62E-02	1.79E-04	5.10E-05	3.12E-05	4.05E-09
Isopropanol	8.98E-02	2.94E-04	7.33E-05	2.34E-04	6.30E-09
Ethyl acetate	4.98E-03	3.55E-05	7.58E-06	5.64E-06	2.09E-09
High-density polyethylene	5.43E-02	1.88E-04	1.68E-05	8.07E-05	6.13E-09
Electrified cleaning agent use	1.99E-02	3.27E-04	5.51E-05	6.50E-05	1.27E-09
Direct contribution	0.00E+00	0.00E+00	0.00E+00	0.00E+00	0.00E+00
electricity	5.28E-03	2.98E-05	1.85E-06	8.88E-06	1.35E-11
Product transportation	1.47E-02	2.97E-04	5.33E-05	5.61E-05	1.26E-09
Electrified cleaning agent Disposal	1.86E-01	1.04E-03	1.89E-04	2.84E-04	1.45E-09
electricity	1.40E-01	7.89E-04	4.90E-05	2.35E-04	3.59E-10
Sludge	3.48E-02	1.58E-05	9.80E-05	4.55E-06	1.07E-10
Sludge-Transport	1.32E-04	2.67E-06	4.80E-07	5.05E-07	1.13E-11
Waste solvent-transportation	1.13E-02	2.29E-04	4.10E-05	4.32E-05	9.70E-10

Table 10. Cumulative contribution results of electrified cleaning agent (continued)

Name	POFP	IRP	ET	HT-cancer	HT-non cancer
Electrified cleaning agent total	2.89E-02	3.16E-02	2.69E-01	4.32E-08	2.31E-07
Electrified cleaning agent production	6.36E-03	2.26E-02	2.21E-01	2.19E-08	1.51E-07
electricity	5.27E-06	7.63E-04	6.08E-05	3.32E-12	7.86E-12
D40 solvent oil	1.77E-03	1.48E-02	1.00E-01	4.82E-09	7.88E-09
D40 solvent oil-transportation	5.87E-05	5.16E-05	3.94E-04	1.65E-11	2.69E-11
Tetrachloroethylene	3.92E-03	2.07E-04	1.08E-01	1.66E-08	1.40E-07
Tetrachloroethylene-Transport	2.97E-05	2.61E-05	1.99E-04	8.33E-12	1.36E-11
Butanol	1.44E-04	4.19E-03	5.12E-03	1.44E-10	1.41E-09
Isopropanol	1.34E-04	7.16E-04	3.03E-03	1.29E-10	2.11E-10
Ethyl acetate	2.26E-05	9.49E-04	1.25E-03	2.27E-11	3.21E-10
High-density polyethylene	2.81E-04	8.72E-04	2.65E-03	1.26E-10	2.06E-10
Electrified cleaning agent use	2.24E-02	3.97E-04	4.76E-02	2.12E-08	8.01E-08
Direct contribution	2.23E-02	0	4.70E-02	2.12E-08	8.00E-08
electricity	2.20E-06	3.18E-04	2.53E-05	1.38E-12	3.27E-12
Product transportation	8.96E-05	7.87E-05	6.00E-04	2.51E-11	4.10E-11

Electrified cleaning agent 【 Disposal】	1.47E-04	8.62E-03	1.24E-03	5.67E-11	1.37E-10
electricity	5.82E-05	8.43E-03	6.71E-04	3.67E-11	8.68E-11
Sludge	1.86E-05	1.29E-04	1.04E-04	4.36E-13	1.86E-11
Sludge-Transport	8.06E-07	7.08E-07	5.40E-06	2.26E-13	3.69E-13
Waste solvent-transportation	6.90E-05	6.06E-05	4.62E-04	1.93E-11	3.16E-11

According to the LCA results of electrified cleaning agent 【 production 】 (Figures 4 - 13), the results of various indicators are as follows:

- (1) For the GWP indicator, the three processes that contribute the most are the production of tetrachloroethylene (1.23 kg CO₂ eq), the production of D40 solvent oil (0.437 kg CO₂ eq), and electricity (electrified cleaning agent 【disposal】) (0.14 kg CO₂ eq).
- (2) Acidification (AP): The three processes that contribute the most are the production of tetrachloroethylene (5.12E-03 kg SO₂ eq), the production of D40 solvent oil (1.95E-03 kg SO₂ eq), and electricity (electrified cleaning agent 【disposal】) (7.89E-04 kg SO₂ eq).
- (3) Eutrophication potential (EP): The three most contributing processes are tetrachloroethylene production (4.45E-04 kg PO₄³⁻eq), D40 solvent oil production (2.79E-04 kg PO₄³⁻eq), and sludge landfill (7.89E-04 kg PO₄³⁻eq).
- (4) Inhalable inorganic matter (RI): The four processes that contribute the most are tetrachloroethylene production (1.04E-03 kg PM_{2.5} eq), D40 solvent oil production (3.17E-04 kg PM_{2.5} eq), electricity (electrified cleaning agent 【disposal】) (2.35E-04 kg PM_{2.5} eq), and isopropanol production (2.34E-04 kg PM_{2.5} eq).
- (5) Ozone depletion potential (ODP): The three processes that contribute the most are tetrachloroethylene production (4.88E-05 kg CFC-11 eq), D40 solvent oil production (2.42E-07 kg CFC-11 eq), and isopropanol production (6.30E-09 kg CFC-11 eq).
- (6) Photochemical ozone formation potential (POFP): The three processes that contribute the most are the environmental emissions caused by solvent volatilization during the process of electrified cleaning agent 【use】 (2.23E-02 kg NMVOC eq), the production of tetrachloroethylene (3.92E-03 kg NMVOC eq) , and D40 solvent oil production (1.77E-03 kg NMVOC eq).
- (7) Ionizing radiation-Human Health (IRP): The three processes that contribute the most are D40 solvent oil production (1.48E-02 kg U235 eq), electricity (electrified cleaning agent 【Disposal】) (8.43E-03 kg U235 eq), and D40 production (4.19E-03 kg U235 eq).
- (8) Ecotoxicity (ET): The three processes that contribute the most are the production of tetrachloroethylene (1.08E-01 CTUe), the production of D40 solvent oil (1.00E-01 CTUe), and the environment emissions caused by the volatilization of solvents in the process of electrified cleaning agent 【use】 (4.70E-02 CTUe).
- (9) Human toxicity-carcinogenic (HT-cancer): The three processes that contribute the most are the environmental emissions (2.12E-08 CTUh) caused by solvent volatilization during the process of the charged cleaner 【use】 , the production of tetrachloroethylene (1.66E-08 CTUh) , and D40 solvent oil production (4.82E-09 CTUh).
- (10) Human toxicity-non-carcinogenic (HT-non cancer): The three processes that contribute the most are the production of tetrachloroethylene (1.40E-07 CTUh), the

environmental emissions caused by solvent volatilization during the process of electrified cleaning agent 【use】 ($8.00E-08$ CTUh), and D40 solvent oil production ($7.88E-09$ CTUh).

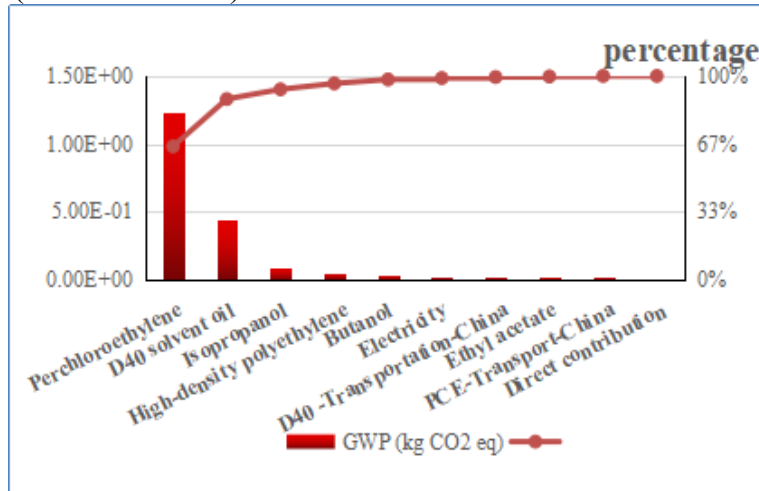


Figure 4. Global warming potential (GWP) results of electrified cleaning agent 【production】

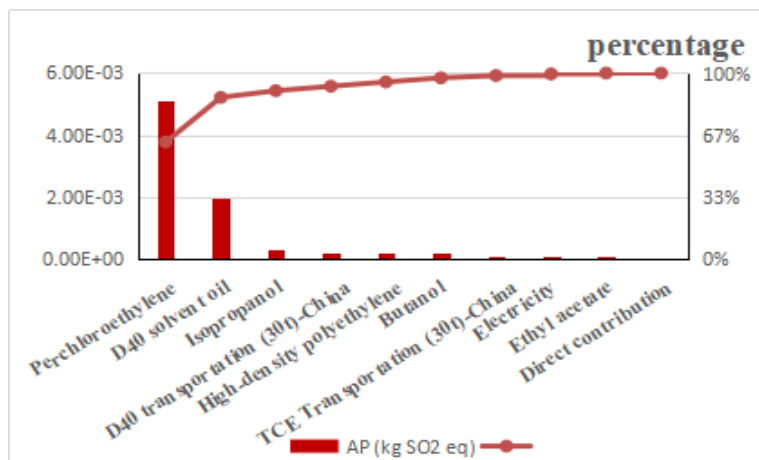


Figure 5. Acidification potential (AP) results of electrified cleaning agent 【production】

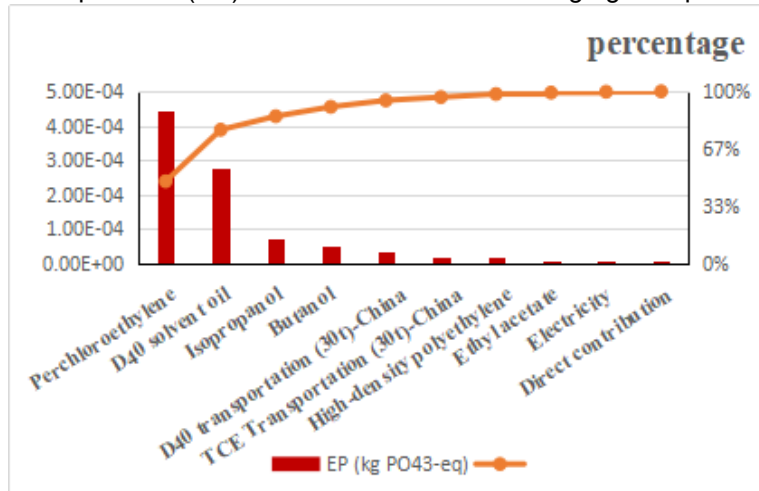


Figure 6. The eutrophication potential (EP) results of electrified cleaning agent 【production】

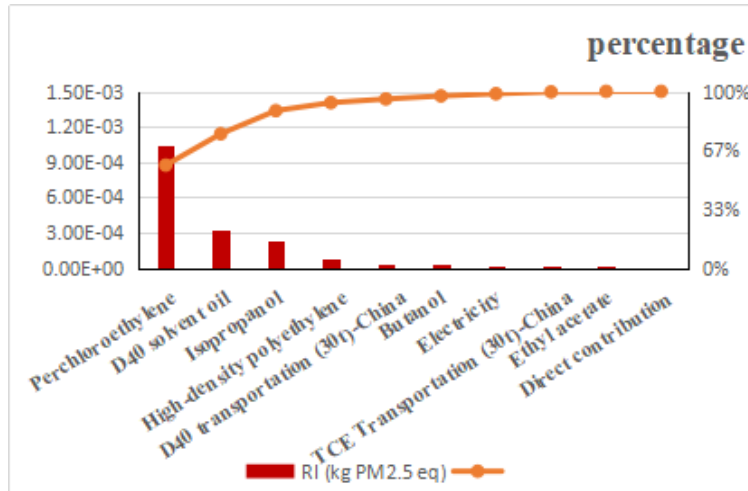


Figure 7. Inhalable inorganic matter (RI) results of electrified cleaning agent 【production】

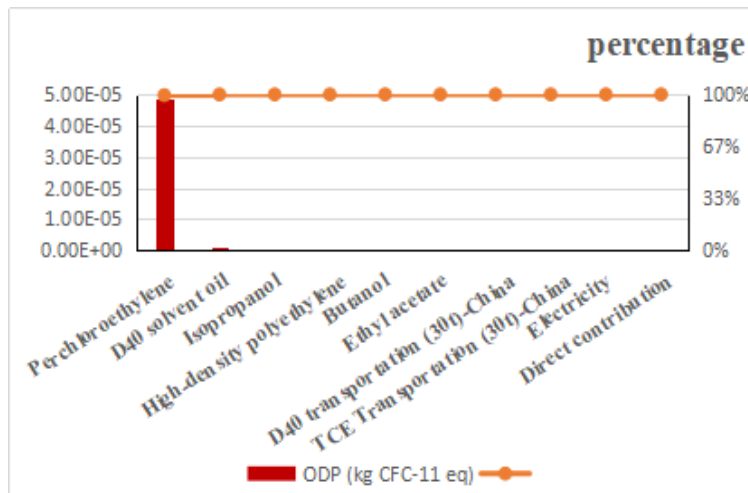


Figure 8. Ozone depletion (ODP) results of electrified cleaning agent 【production】

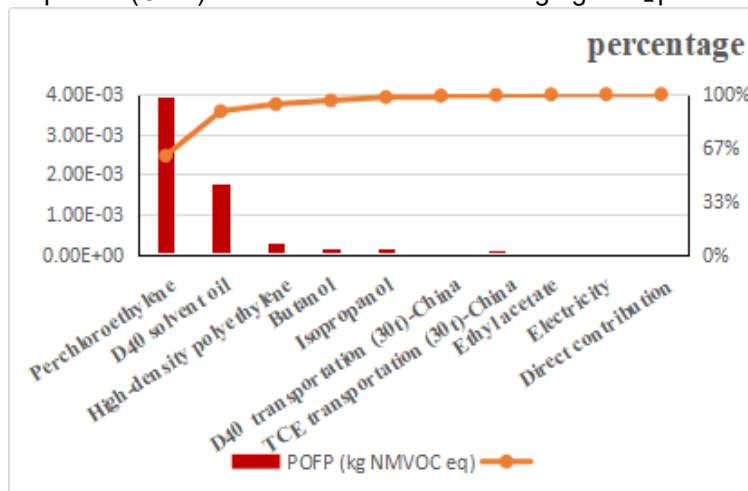


Figure 9. Photochemical ozone formation potential (POFP) results of electrified cleaning agent 【production】

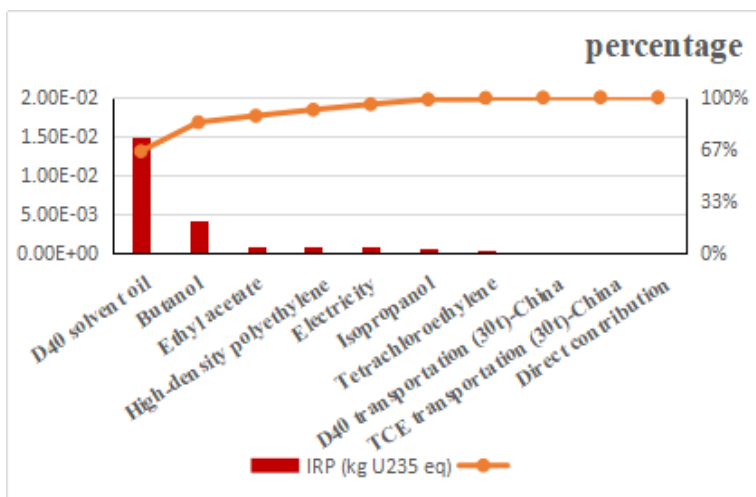


Figure 10. Ionizing radiation potential (IRP) results of electrified cleaning agent 【production】

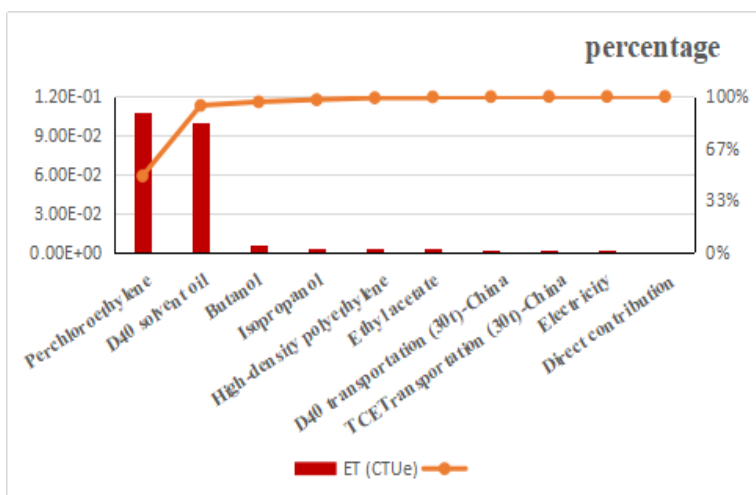


Figure 11. Ecotoxicity (ET) results of electrified cleaning agent 【production】

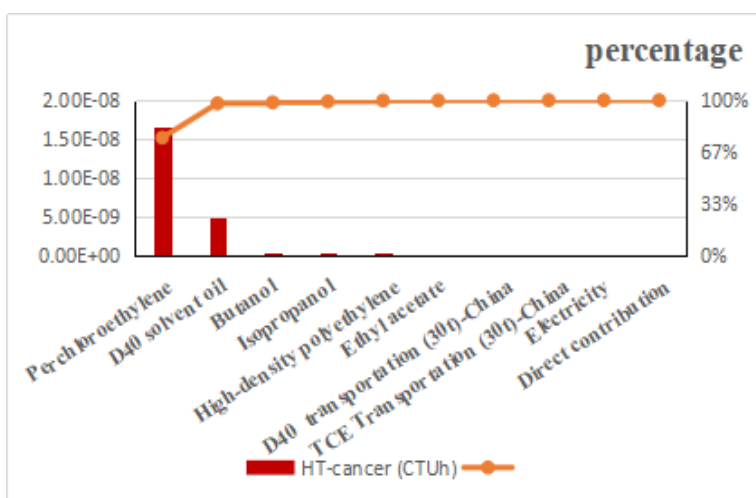


Figure 12. Human toxicity-carcinogenic (HT-cancer) results of electrified cleaning agent 【production】

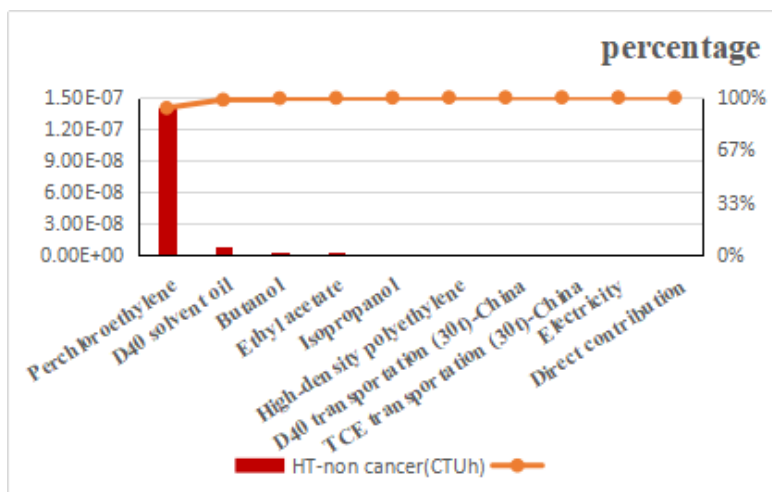


Figure 13. Human toxicity-HT-non cancer results of electrified cleaning agent 【production】

4.3 Sensitivity Analysis of Inventory Data

Inventory data sensitivity refers to the corresponding indicator change rate caused by the unit change rate of inventory data. By analyzing the sensitivity of the inventory data to each indicator and cooperating with the improvement potential evaluation, the most effective improvement points can be identified. Table 11 lists the inventory data with sensitivity > 0.5%.

According to the average sensitivity (contribution rate) analysis:

- (1) The five processes with the highest average sensitivity are tetrachloroethylene production 51.48%, D40 solvent oil production 12.66%, tetrachloroethylene environmental emissions 【use】 11.85%, butanol emissions 【use】 5.54%, and electricity 【disposal】 3.82%.
- (2) For the GWP, the top 5 processes with the highest sensitivity are tetrachloroethylene production 58.95%, D40 solvent oil production 20.96%, electricity 【Disposal】 6.71%, isopropanol production 4.31%, and high-density polyethylene 2.61% .
- (3) For the AP, the top five processes with the highest sensitivity are tetrachloroethylene production 53.90%, D40 solvent oil production 20.57%, electricity 【Disposal】 8.31%, product transportation 3.13%, and isopropanol production 3.10%.
- (4) For the EP, the top 5 processes with the highest sensitivity are tetrachloroethylene production 37.84%, D40 solvent oil production 23.73%, sludge landfill 8.34%, isopropanol production 6.24%, and product transportation 4.53%.
- (5) For the RI, the top 5 processes with the highest sensitivity are tetrachloroethylene production 48.77%, D40 solvent oil production 14.86%, electricity 【Disposal】 11.02%, isopropanol production 10.94%, and high-density polyethylene 3.78%.
- (6) For ozone depletion (ODP), the most sensitive processes are tetrachloroethylene production (99.46%) and the production of D40 solvent oil (0.49%).
- (7) For the POFP, the most sensitive processes are 44.31% of butanol environmental emissions, 17.37% of isopropanol environmental emissions, 13.57% of tetrachloroethylene production, 11.03% of tetrachloroethylene environmental emissions, and 6.12% of D40 solvent oil production.

Table 11. Sensitivity of inventory data (unit: %)

Process	GWP	AP	EP	RI	ODP	POFP	IRP	ET	HT-cancer	HT-non cancer	Average sensitivity
Electrified cleaning agent 【production】	90.1	85.64	79.26	83.67	99.99	22.03	71.45	81.85	50.71	65.23	72.08
Electrified cleaning agent 【use】	0.96	3.44	4.692	3.044	0.003	77.458	1.256	17.68	49.15	34.70	21.68
Electrified cleaning agent 【disposal】	8.93	10.91	16.043	13.284	0.003	0.508	27.290	0.461	0.131	0.060	6.23
Electrified cleaning agent 【production】											
Electricity	0.61	0.75	0.377	0.998	0.000	0.018	2.417	0.023	0.008	0.003	0.35
D40 solvent oil	20.96	20.56	23.728	14.86	0.494	6.122	46.842	37.22	11.176	3.414	12.66
D40 solvent Oil-transportation	0.46	2.05	2.974	1.723	0.002	0.203	0.163	0.146	0.038	0.012	0.93
Tetrachloroethylene	58.95	53.89	37.844	48.771	99.46	13.573	0.656	39.91	38.502	60.86	51.48
Tetrachloroethylene-Transport	0.23	1.04	1.505	0.872	0.001	0.103	0.083	0.074	0.019	0.006	0.47
Butanol	1.74	1.88	4.335	1.463	0.008	0.499	13.257	1.902	0.334	0.613	1.36
Isopropanol	4.31	3.09	6.235	10.940	0.013	0.464	2.268	1.125	0.299	0.091	3.18
Ethyl acetate	0.239	0.37	0.645	0.264	0.004	0.078	3.007	0.465	0.052	0.139	0.22
High-density Polyethylene	2.61	1.98	1.433	3.781	0.012	0.973	2.761	0.985	0.291	0.089	1.40
Electrified cleaning agent 【use】											
Electricity	0.25	0.31	0.157	0.416	0.000	0.008	1.007	0.009	0.003	0.001	0.14
Product Transportation	0.70	3.13	4.535	2.628	0.003	0.310	0.249	0.223	0.058	0.018	1.42
Tetrachloroethylene	0.000	0.000	0.000	0.000	0.000	11.032	0.000	17.45	49.088	34.68	11.85
Butanol	0.0	0.0	0.0	0.0	0.0	44.31	0.0	0.0	0.0	0.0	5.54
Isopropanol	0.0	0.0	0.0	0.0	0.0	17.37	0.0	0.0	0.0	0.0	2.17
Ethyl acetate	0.0	0.0	0.0	0.0	0.0	4.43	0.0	0.0	0.0	0.0	0.55
Electrified cleaning agent 【disposal】											
Electricity	6.71	8.31	4.168	11.024	0.001	0.202	26.687	0.249	0.085	0.038	3.82
Sludge	1.67	0.17	8.342	0.213	0.000	0.064	0.409	0.038	0.001	0.008	1.31
Sludge-Transport Waste	0.006	0.028	0.041	0.024	0.000	0.003	0.002	0.002	0.001	0.000	0.01
Solvent-vehicle Transportation	0.54	2.41	3.492	2.023	0.002	0.239	0.192	0.172	0.045	0.014	1.10

- (8) For the IRP, the most sensitive processes are D40 solvent oil production (46.84%), electricity 【Disposal】 (26.69%), and butanol production (13.26%).
- (9) For the eco-toxicity (ET), the most sensitive processes are 39.91% of tetrachloroethylene production, 37.22% of D40 solvent oil production, and 17.45% of environmental emissions of tetrachloroethylene 【use】 .
- (10) For Human toxicity-carcinogenic (HT-cancer), the most sensitive processes are tetrachloroethylene environmental emission 【use】 49.09%, tetrachloroethylene production 38.50%, and D40 solvent oil production 11.18%.

(11) For Human toxicity-HT-non cancer, the most sensitive processes are tetrachloroethylene production 60.86%, tetrachloroethylene environmental emissions 【use】 34.69%, and D40 solvent oil production 3.41%.

Comprehensive analysis shows that the four processes including tetrachloroethylene production, D40 solvent oil production, environmental discharge of tetrachloroethylene 【use】 and electricity 【product disposal】 have significant effects on each LCA indicator. So, they are the focus of process improvement. The environmental emission of butanol only affects the photochemical ozone formation potential (POFP).

4.4 Possible Process Improvement

- (1) Tetrachloroethylene and D40 solvent oil are the necessary active ingredients in electrified cleaner products. It is recommended to optimize the production process to reduce environmental emissions, or to develop a cleaner production process.
- (2) Efforts should be made to reduce the environmental emissions of tetrachloroethylene and other solvents during the use of the product, develop the efficient solvent recovery equipment, and improve operating procedures.
- (3) Distillation for the recovery of waste solvents is a process with high energy consumption. Renewable energy should be used to replace electricity as much as possible to obtain carbon credits.

4.5 The Impact of Electricity Consumption during Production on Carbon Footprint

In the original model, the energy consumption of heating, stirring, cooling, and material transportation during the production process is considered. The power consumption estimated is 0.05 MJ. The simulated production process did not consider other processes that may be used, such as the energy consumption of the filtration process. It is estimated that all production energy consumption should be less than 0.1 MJ. Table 15 shows the impact of increasing power consumption from 0.05 MJ to 1 MJ on total carbon emissions. It can be seen that when the energy consumption increases to 0.1 MJ, the total carbon emissions only increase by 0.96%. When the electricity consumption further increases 10 times to 1 MJ, carbon emissions will increase by about 12%. Therefore, under the premise of paying attention to energy conservation in the production process, electricity consumption has little effect on the carbon footprint.

Table 15. Impact of electricity consumption on carbon footprint

Power consumption /MJ	Production process GWP / $(\text{kg CO}_2 \text{ eq})$	Total carbon emissions GWP / $(\text{kg CO}_2 \text{ eq})$	Increase in carbon emissions /%
0.05(Benchmark)	1.88	2.08	-
0.1	1.89	2.10	+0.96
0.5	2.00	2.20	+5.77
1	2.13	2.33	+12.02

4.6 Impact of Transportation Distance on Carbon Footprint

In the original model, only the transportation of D40 solvent oil and tetrachloroethylene, which accounted for 64% and 33% of the components, respectively, was considered. The transportation distance was assumed to be 200 km, which is close to

the national average goods transportation distance of 187 km. The data in Table 16 shows that increasing the transportation distance of D40 solvent oil to 2000 km will only increase the total carbon emissions by 4.33%. Therefore, the transportation distance of raw materials has little effect on total carbon emissions.

Table 16. The impact of D40 solvent oil transportation distance on carbon footprint

Transport distance /km	Transport GWP /(kg CO ₂ eq)	Total carbon emissions GWP /(kg CO ₂ eq)	Increase in carbon emissions /%
200(Benchmark)	9.62E-03	2.08	-
500	2.40E-02	2.10	+0.40
1000	4.81E-02	2.12	+1.92
2000	9.62E-02	2.17	+4.33

In the original model, the product transport distance is 200 km. The data in Table 17 shows that when the product transportation distance is increased to 2000 km, the total carbon emissions only increase by 6.73%. Therefore, product transportation distance has little effect on total carbon emissions.

Table 17. Impact of product transportation distance on carbon footprint

Transport distance /km	Transport GWP /(kg CO ₂ eq)	Total carbon emissions GWP /(kg CO ₂ eq)	Increase in carbon emissions /%
200(Benchmark)	9.62E-03	2.08	-
500	2.40E-02	2.10	+0.40
1000	4.81E-02	2.12	+1.92
2000	9.62E-02	2.17	+4.33

4.7 Comparison with LCA Indicators of Other Electrified Cleaner Production Processes

The LCA results of this study is further compared with the LCA indicators of other three common electrified cleaner production processes, including trichloroethylene, tetrachloroethylene and n-bromopropane (data source is the Ecoinvent 3.1 database).

Table 18. Comparison of LCA indicators in the production process of electrified cleaning agent

Name	GWP	AP	EP	RI	ODP
Electrified cleaning agent [production]	1.88E+00	8.13E-03	9.32E-04	1.79E-03	4.91E-05
Trichloroethylene	4.92E-01	3.32E-02	2.01E-03	5.29E-03	4.00E-05
Change ratio (%)	-73.81	308.17	115.98	195.91	-18.49
Tetrachloroethylene	3.83E+00	1.62E-02	1.46E-03	3.30E-03	1.50E-04
Change ratio (%)	103.82	99.11	56.22	84.53	205.62
N-bromopropane	5.23E+00	2.62E-02	6.63E-03	4.41E-03	1.15E-06
Change ratio (%)	178.74	222.15	611.74	146.78	-97.65

Table 18. Comparison of LCA indicators in the production process of electrified cleaning agent (continued)

Name	POFP	IRP	ET	HT-cancer	HT-non cancer
Electrified cleaning agent [production]	6.36E-03	2.26E-02	2.21E-01	2.19E-08	1.51E-07
Trichloroethylene	1.91E-02	6.36E-03	4.47E-01	8.74E-08	4.44E-07
Change ratio (%)	200.75	-71.81	102.50	299.42	195.04
Tetrachloroethylene	1.25E-02	6.10E-03	3.59E-01	5.16E-08	4.38E-07
Change ratio (%)	96.72	-72.98	62.66	135.81	190.67
N-bromopropane	1.35E-02	5.83E-01	1.05E+00	1.70E-08	4.37E-07
Change ratio (%)	112.18	2484.36	374.82	-22.54	190.04

It can be seen from the results of the LCA analysis (Table 18) that although trichloroethylene has a small carbon footprint and ionizing radiation, it is not selected for use because it is a flammable liquid that can cause fire and explosion when exposed to open flames and high heat. In comparison, the carbon footprints of the commonly used single-solvent electrified cleaning agents of tetrachloroethylene and n-bromopropane are 103.8% and 178.7% higher than the carbon footprint of the electrified cleaning agent of this study. And most of the other LCA indicators of these two electrified cleaning agents are also higher. Therefore, the production of the electrified cleaning agent developed in this study has its own advantages in terms of carbon footprint and other environmental impact indicators.

4.8 The Impact of Waste Solvent Recovery Efficiency on LCA Indicators

In the benchmark model, the recovery ratio of waste solvents is assumed to be 80%, *i.e.*, 20% of tetrachloroethylene and D40 solvent oil are discharged as air emissions. Although the emission of D40 solvent oil is environmentally friendly, the emission of tetrachloroethylene has an obvious impact on photochemical ozone formation potential (POFP), ecological toxicity (ET), human toxicity-carcinogenic (HT-cancer), and human body Toxicity-non-carcinogenic (HT-non cancer) indicators. Moreover, the recovery efficiency is directly related to the waste solvent recovery process. Therefore, it is necessary to further study the influence of waste solvent recovery efficiency on various indicators of the whole life cycle.

Table 19. The effect of electrified cleaning agent recovery ratio on LCA indicators

Waste solution recovery ratio /discharge ratio (%)	GWP	AP	EP	RI	ODP
100/0	2.13E+00	9.77E-03	1.20E-03	2.21E-03	4.91E-05
80/20	2.08E+00	9.49E-03	1.18E-03	2.13E-03	4.91E-05
Change ratio (%)	-2.20	-2.89	-2.04	-3.51	0.00
50/50	2.03E+00	9.12E-03	1.14E-03	2.03E-03	4.91E-05
Change ratio (%)	-4.74	-6.63	-4.76	-8.03	0.00
20/80	1.97E+00	8.73E-03	1.11E-03	1.93E-03	4.91E-05
Change ratio (%)	-7.46	-10.62	-7.63	-12.85	0.00
0/100	1.90E+00	8.46E-03	9.87E-04	1.85E-03	4.91E-05
Change ratio (%)	-10.91	-13.45	-17.74	-16.29	0.00

Table 19. The effect of electrified cleaning agent recovery ratio on LCA indicators (continued)

Waste solution recovery ratio /discharge ratio (%)	POFP	IRP	ET	HT-cancer	HT-non cancer
100/0	2.57E-02	3.40E-02	2.23E-01	2.20E-08	1.51E-07
80/20	2.89E-02	3.16E-02	2.69E-01	4.32E-08	2.31E-07
【Change ratio】 /%	12.25	-7.07	20.97	96.28	53.08
50/50	3.36E-02	2.85E-02	3.40E-01	7.51E-08	3.51E-07
【Change ratio】 /%	30.74	-15.98	52.62	241.46	133.11
20/80	3.83E-02	2.53E-02	4.10E-01	1.07E-07	4.71E-07
【Change ratio】 /%	49.03	-25.57	83.93	385.15	212.32
0/100	4.15E-02	2.30E-02	4.57E-01	1.28E-07	5.51E-07
【Change ratio】 /%	61.31	-32.33	105.03	482.17	265.79

From the data in Table 19, the recovery ratio of electrified cleaning agent is directly related to the power consumption of the waste process and the toxicity caused by environmental emissions. The higher the recovery ratio, the higher the energy consumption of the solution recovery process, which in turn leads to an increase in the carbon footprint (GWP), AP, EP, RI and IRP indicators of the whole life cycle. On the contrary, if the solvent is allowed to discharge to the environment, it will cause a significant increase in environmental toxicity indicators such as POFP, ET, HT-cancer and HT-non cancer. Therefore, the full cycle emissions of any product and process are closely related to the technical details of the entire process. The goal of reducing carbon footprint and other environmental impact indicators can be achieved only by choosing a low-emission and reasonable process.

As far as this process is concerned, a low-energy waste solvent recovery process should be developed, the power consumption of the current distillation recovery device should be reduced as much as possible, and renewable energy can be used to replace fossil energy. At the same time, the solvent recovery device needs to be improved to increase efficiency and minimize direct environmental emissions.

4.9 Estimation of the Carbon Footprint of the Upstream Tetrachloroethylene Production Process

The study further estimated the carbon emissions of the two upstream production processes (tetrachloroethylene and D40 solvent oil) that have the largest impact on the carbon footprint. Tetrachloroethylene (molecular formula C_2Cl_4 , CAS-No. 127-18-4, also known as PCE or perchloroethylene) is a colorless and transparent liquid with an ester-like smell. It is not flammable and has no measurable flash point or flammability limit in air. Usually acetylene or ethylene is used as a raw material, and it is co-produced with trichloroethylene through chlorination and oxidation. The life cycle data of tetrachloroethylene comes from the Ecoinvent3.1 database of Europe, and the unit is 1 kg. The boundary map is as follows:

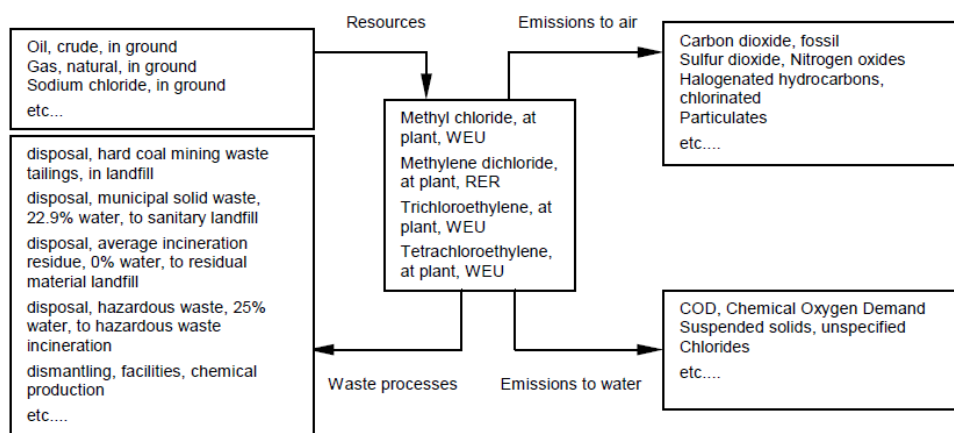


Figure 14. Process chain for the production of methyl chloride, methylene chloride, trichloroethylene and tetrachloroethylene

The chemical equation produced by tetrachloroethylene is as follows:

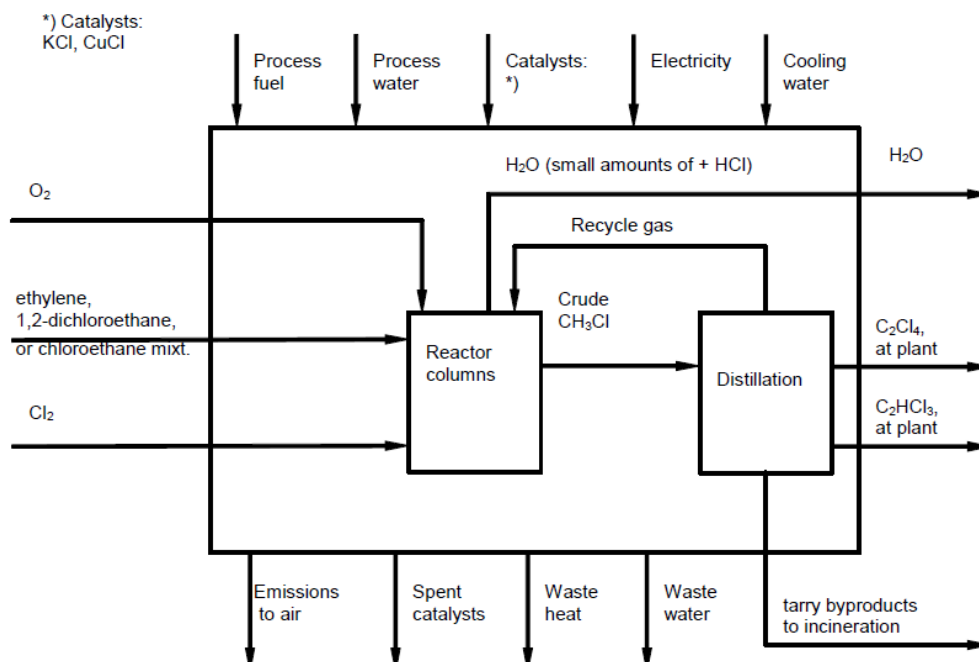


Figure 15. Simplified process for preparing tetrachloroethylene through the oxychlorination reaction (reactor)

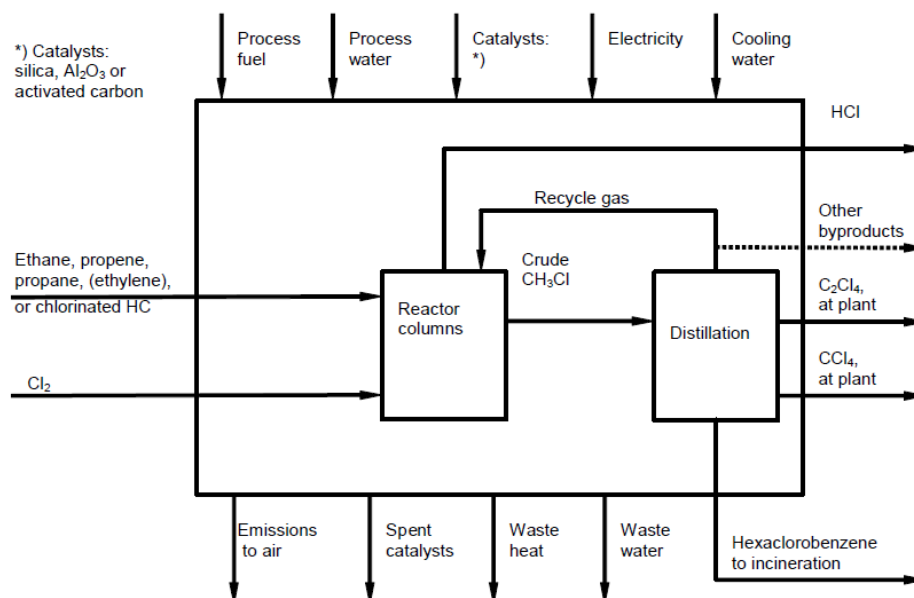


Figure 16. The process of preparing tetrachloroethylene by chlorinating solubilization

Due to the confidentiality of commercial databases, the possible sources of upstream emissions can only be inferred through possible raw materials and reaction pathways. Table 20 summarizes the carbon emission (GWP) data of 1 kg of ethylene (C_2H_2), chlorine (Cl_2), and tetrachloroethylene.

Table 20. Carbon footprint analysis of tetrachloroethylene production process (unit: kg)

Process	Carbon emission	Process	Carbon emission	Process	Carbon emission
Tetrachloroethylene C_2Cl_4 (1kg)	3.83 ^b	Ethylene (1kg)	1.08 ^c	Petroleum refined products (1kg)	0.52 ^c
		Natural gas production	0.52	Crude oil extraction	0.22
		Natural gas heating	0.347	electricity	0.108
		Petroleum Refined Products	0.14	By sea	0.0896
Ethylene (1kg)	1.78 ^a			Residual fuel oil combustion	0.0843
	1.37 ^b			Natural gas heating	0.022
	1.08 ^c				
Chlorine (1kg) process	1.68-2.51 ^a	Chlorine (1kg)	1.04 ^{c,d}		
	1.32-1.34 ^b	electricity	0.569		
Tetrachloroethylene C_2Cl_4 (1kg)	1.04 ^{c,d}	natural gas	0.257		
		NaCl	0.136		
Ethylene (1kg)		Coal	0.07		

Data source a: CLCD-China-ECER 0.8; b: Ecoinvent 3.1; c: USLCI; d: commercial database

Emissions from ethylene production originate from natural gas production, process heating, and oil refining. However, according to the analysis of the molecular formula and chemical reaction formula of tetrachloroethylene, ethylene production does not contribute much to the carbon footprint of the entire process. The main carbon emission of tetrachloroethylene comes from the chlorine production process. According to the production methods of different countries and regions, it can be seen that China uses the ion-exchange membrane method of chlor-alkali electrolysis to produce chlorine, producing carbon emissions of 1.68-2.51 kg CO₂ eq. The chlor-alkali electrolysis process (membrane technology), which is widely used in Europe and the United States, has a lower carbon emission of 1.04 kg CO₂ eq. According to the LCA boundary map (Figure 17) and analysis results given by the commercial database, it can be seen that the carbon footprint sources of the production of chlorine include electricity, natural gas combustion and the energy consumption of the NaCl production process.

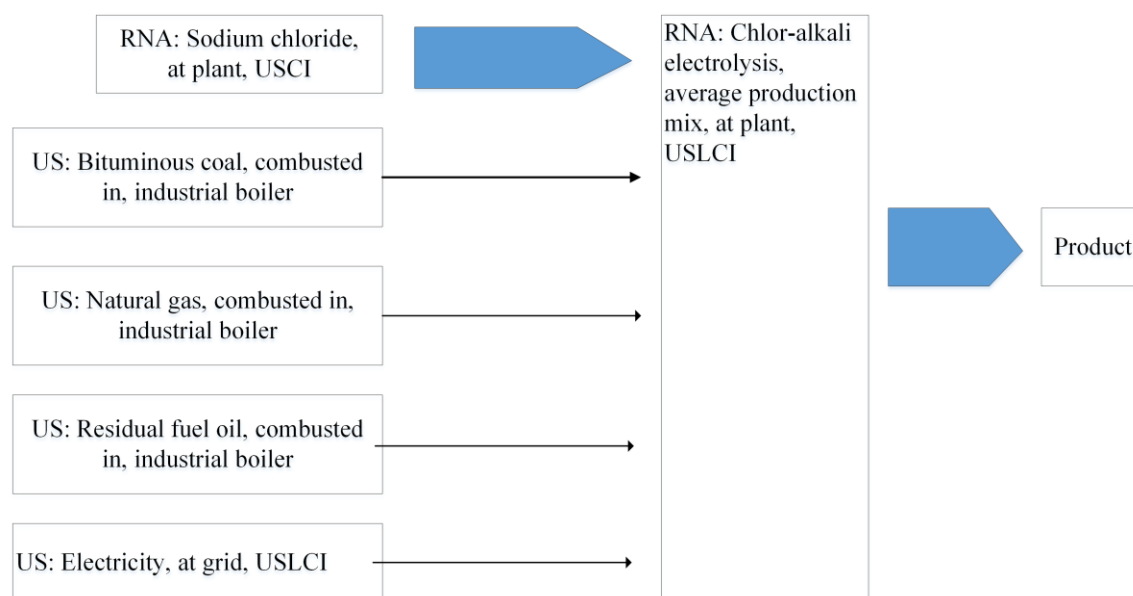


Figure 17. LCA boundary diagram of chlorine produced by electrolysis

The analysis shows that the main carbon emissions from the tetrachloroethylene production process are the electricity consumption of each process, the combustion of natural gas production and the combustion of other energy materials for heating. It is recommended to use renewable raw materials instead of crude oil to obtain carbon credits based on geographical advantages, and try to use production processes with lower carbon emissions, while the exhaust gas from the traditional production process is strictly absorbed and purified before being discharged.

4.10 Carbon Footprint Estimation of the Upstream D40 Solvent Oil Production Process

D40 solvent oil is made of distillate oil as raw material, after high-pressure hydrotreating and fractional distillation. Its main component is saturated alkanes, including nonane, decane and undecane. The production process is basically the same as naphtha. So in this study, the naphtha process was used instead of D40 solvent oil. The carbon footprint of the naphtha production process is estimated using data from

commercial databases. The process diagram is shown in Figure 18, and the data of several databases is summarized in Table 21.

It can be seen from the process diagram that petroleum refining is a complex process. The data set includes drilling, crude oil production, processing, transportation of crude oil through pipelines, and ship transportation to the refinery. The whole process requires a lot of fuel to generate heat, steam and electricity. These fuels may be refinery gas, heating oil (residual oil), gasoline coke, middle distillate oil and liquefied petroleum gas. The output of petroleum refining is a series of products, and the quality of the product is closely related to the composition of the crude oil, the region and the refining technology used.

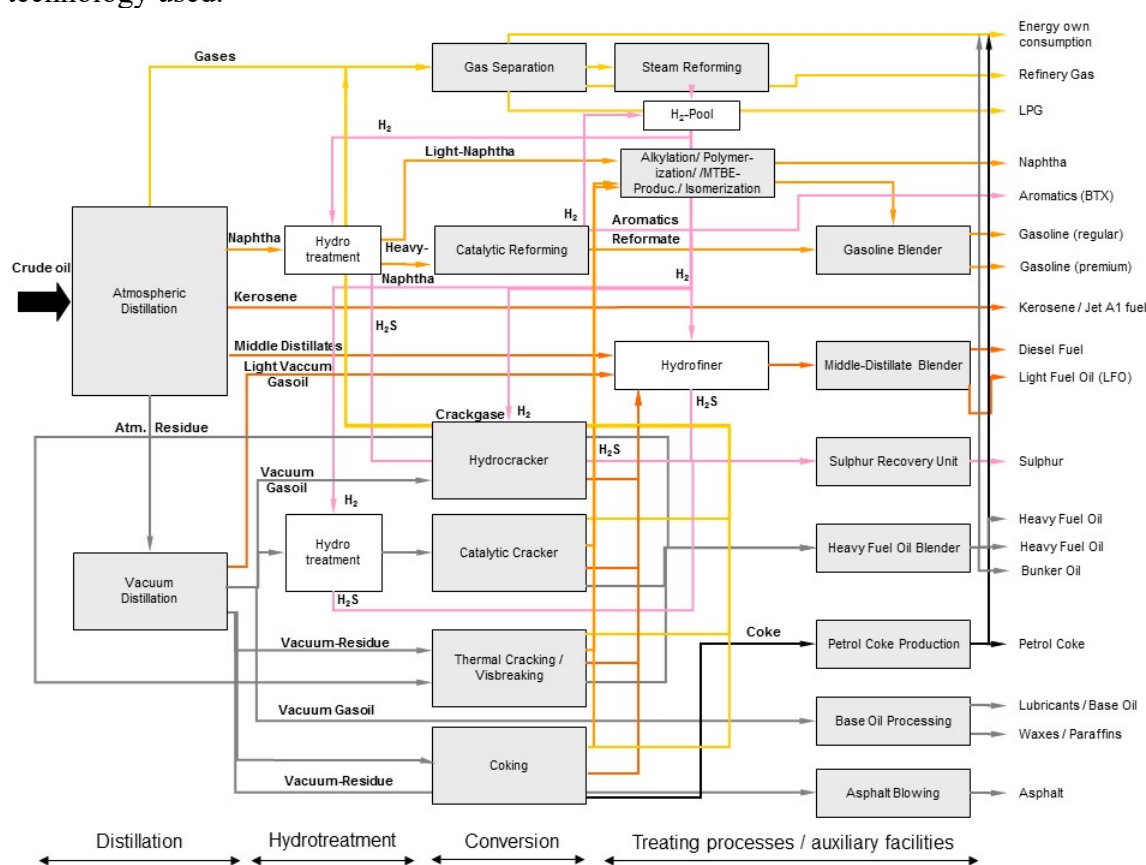


Figure 18. Schematic diagram of petroleum refining process

Table 24. Carbon footprint analysis of D40 solvent oil (naphtha) production process (Unit: kg)

Process	Carbon emission
Naphtha (1kg)	0.679 ^a
	0.363 ^b
	0.599 ^c

Data source: a: CLCD-China-ECER 0.8; b: Ecoinvent 3.1; c: commercial database

Analysis shows that the main carbon emissions from the production process of D40 solvent oil (naphtha) come from the production process of petroleum refining and natural gas production, and the emissions are closely related to the quality of crude oil and the refining process. It is recommended to improve the existing petroleum refining

process, purchase cleaner crude oil as the raw material, and discharge the exhaust gas after strict absorption and purification.

5. Life Cycle Explanation

5.1 Assumptions and Limitations

This study calculated the results of 10 indicators of the electrified cleaning agent production process. The detergent formula is determined by this research and does not represent the industry average. When simulating the calculation process, only the energy consumption of the core equipment is calculated. It is assumed that when the main equipment is increased, only electricity is consumed, and the process emissions are not increased. It is assumed that the production technology used for the raw materials is the same as the technology in commercial databases and public documents, and the emissions are the same.

5.2 Integrity Description

Strict mass balance and energy balance calculations were carried out for the production process of the electrified cleaning agent. The emission data were adopted from the literature and company measurement. The possible increase in power consumption in the process of production improvement has been discussed in detail in the carbon footprint analysis of power consumption in the section 4.5. The emission data of the production process and waste disposal was obtained from the public databases, and the emission data is highly reliable.

5.3 Data Quality Assessment

The report uses the CLCD quality assessment method to complete the uncertainty assessment of the model inventory data on the eFootprint system. The data quality evaluation results obtained are shown in Table 25.

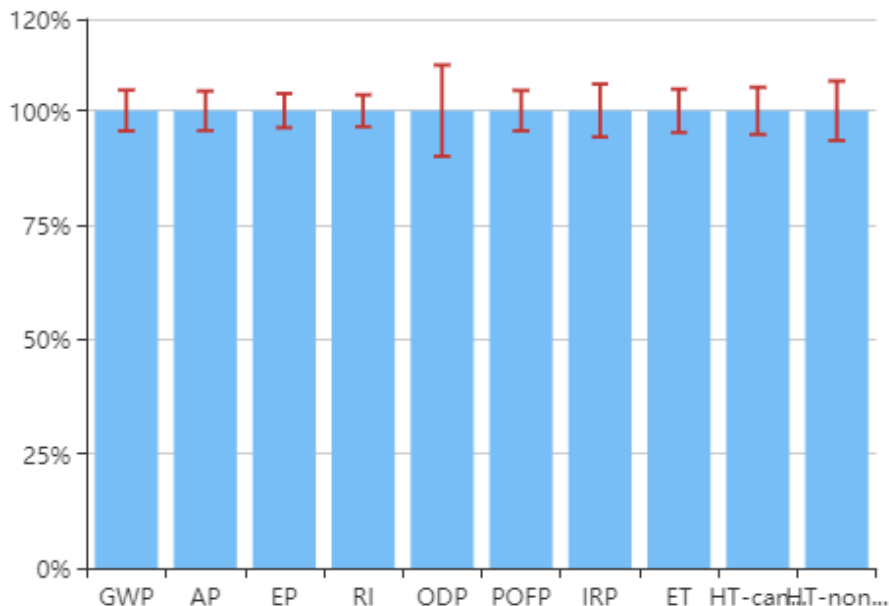


Figure 19. Uncertainty of LCA results

Table 25. LCA data quality assessment

Indicator name	Abbreviation (unit)	LCA results	Uncertainty of result	Results upper and lower limits (95% confidence interval)
Climate change	GWP (kg CO ₂ eq)	2.084E+000	4.44%	[1.99,2.18]
Acidification	AP (kg SO ₂ eq)	9.494E-003	4.31%	[9.08E-03,9.90E-03]
Eutrophication Potential	EP (kg PO ₄ ³⁻ eq)	1.175E-003	3.75%	[1.13E-03,1.22E-03]
Inhalable inorganic matter	RI (kg PM2.5 eq)	2.136E-003	3.46%	[2.06E-03,2.21E-03]
Ozone depletion	ODP (kg CFC-11 eq)	4.909E-005	9.95%	[4.42E-05,5.39E-05]
Photochemical ozone synthesis	POFP (kg NMVOC eq)	2.886E-002	4.39%	[0.03,0.03]
Ionizing radiation	IRP (kg U235 eq)	3.161E-002	5.79%	[0.03,0.03]
Ecotoxicity	ET (CTUe)	2.694E-001	4.73%	[0.26,0.28]
Human toxicity-carcinogenic	HT-cancer (CTUh)	4.316E-008	5.15%	[4.09E-08,4.53E-08]
Human toxicity-non-carcinogenic	HT-non cancer (CTUh)	2.307E-007	6.49%	[2.15E-07,2.45E-07]

6. Conclusions

This study analyzed the whole life cycle of the electrified cleaning agent developed. This electrified cleaning agent has the characteristics of non-phosphorus, green and environmental protection, and very broad market prospects. The life cycle model is cradle to grave, and the background data sets include power grid, transportation, high-density polyethylene, chemicals, etc. The production process uses computer simulation to carry out strict mass balance and energy consumption calculations. The study integrated the data from the manufacturer and the contents of the public literature to analyze the emissions.

- (1) The analysis of the whole life cycle model of the established model shows that the GWP of the life cycle of 1 kg of electrified cleaning agent is 2.08 kg CO₂ eq, AP is 9.49E-03 kg SO₂ eq, EP is 1.18E-03 kg PO₄³⁻eq, and RI is 2.13E-03 kg PM2.5 eq, ODP is 4.91E-05 kg CFC-11 eq, POFP is 2.89E-02 kg NMVOC eq, IRP is 3.16E-02 kg U235 eq, ET is 2.69E-01 CTUe, HT-cancer is 4.32E-08 CTUh, and HT-non cancer is 2.31E-07 CTUh. The uncertainty of the results is between 3.46-9.95%.
- (2) The four processes of tetrachloroethylene production, D40 solvent oil production, tetrachloroethylene environmental discharge 【 use 】 and electricity 【 product disposal 】 have significant effects on each LCA indicator, so they are the focus of process improvement.
- (3) Changes in power consumption during production and transportation distance of raw materials have little effect on total carbon emissions.

- (4) Compared with the production process of single-solvent electrified cleaning agent tetrachloroethylene and n-bromopropane, the production of the electrified cleaning agent developed in this study has its own advantages in terms of carbon footprint and other environmental impact indicators.
- (5) The higher the waste solvent recovery ratio, the higher the energy consumption of the solution recovery process, which in turn leads to an increase in the carbon footprint (GWP), AP, EP, RI and IRP indicators of the whole life cycle. On the contrary, if the solvent is allowed to discharge to the environment, it will cause a significant increase in environmental toxicity indicators such as POFP, ET, HT-cancer and HT-non cancer. It is necessary to develop a low-energy waste solvent recovery process, or improve the current distillation equipment to reduce energy consumption. At the same time, the solvent recovery device needs to be improved to increase efficiency and minimize direct environmental emissions.
- (6) Estimates of carbon emissions from major upstream production processes show that carbon emissions mainly come from the power consumption of each process, natural gas production and combustion, and other energy materials for heating. It is recommended to use renewable raw materials instead of crude oil to obtain carbon credits based on geographical advantages, and try to use production processes with lower carbon emissions, while the exhaust gas from the traditional production process is strictly absorbed and purified before being discharged.

Suggestions

- (1) The results of this study are not industry average, and the improved formula needs to be recalculated.
- (2) It is recommended to improve the existing petroleum refining process; purchase cleaner crude oil as raw materials; use renewable raw materials instead of crude oil to obtain carbon credits according to geographical advantages; and exhaust gas from the production process after strict absorption and purification before being discharged.
- (3) It is also necessary to pay attention to the recycling of packaging materials.

ACKNOWLEDGMENTS

We are grateful for the support from the School of Chemical Engineering and Pharmacy at the Wuhan Institute of Technology. We would also like to thank Mr. Rui Li from Mississippi State University for his assistance in the simulation of chemical processes.

CONFLICTS OF INTEREST

The authors declare that there is no conflict of interests regarding the publication of this paper.

REFERENCES

- [1] Rong, X. (2004) Key Performances and Developing Ideas of Cleanser for Electrified Cleaning. *Cleaning Technology*.
- [2] Ecoinvent 3.1. (other countries). Alex Primas.2014-11-13.
- [3] CLCD-China-ECER 0.8. Naphtha/Naphtha-Naphtha/Naphtha-Atmospheric Vacuum (China). He Qin.2013-02-09
- [4] CLCD-China-ECER 0.8. Isopropanol-(China). Fan Cidong. 2013-02-09
- [5] CLCD-China-ECER 0.8. East China Power Grid-East China Power Transmission (China). HouPing.2013-02-09.
- [6] CLCD-China-ECER 0.8. Truck transportation-heavy diesel truck transportation (30t)-China (China).yangjie.2013-02-09

Article copyright: © 2021 Peng Liu, Bo Zhang, Changyan Yang, Yu Gong, Yinhang Qu, Jiayi Li, Bohan Yang, and Yigang Ding. This is an open access article distributed under the terms of the [Creative Commons Attribution 4.0 International License](https://creativecommons.org/licenses/by/4.0/), which permits unrestricted use and distribution provided the original author and source are credited.



Pyrolysis-Gas Chromatography/Mass Spectrometry Analysis of Oils from Different Sources

Qi Qiu,* Yiting Zhang

College of Chemistry and Environmental Engineering, Shenzhen University, Shenzhen 518060, China

Received March 10, 2021; Accepted May 22, 2021; Published May 23, 2021

Regenerated gutter oil (*i.e.*, waste oil) accounts for 10% of the edible oil market, which has caused serious food safety issues. Currently, there is no standard protocol for the identification of the gutter oil. In this study, the pyrolysis-gas chromatography/mass spectrometry (Py-GC/MS) method was employed to analyze eleven oil samples including edible vegetable oils (tea oil, corn oil, olive oil, sunflower oil, peanut oil and blend vegetable oil) and waste oils (used frying oil, lard, chicken fat, inferior oil and kitchen waste grease). Three factors of pyrolysis temperature, reaction time and sample volume were investigated to optimize the analytical parameters. The optimal pyrolysis conditions were determined to be 600°C, 1 min and an injection volume of 0.3 μ L. Five characteristic components (tetradecane, *z,z*-9,12-octadecadienoic acid, decanoic acid-2-propenyl ester, 17-octadecenoic acid, and *z*-9-octadecenoic acid) were found in all oil samples. The existence of C11-C16 olefins in the pyrolytic products of the animal fats and the other low-quality oils could be utilized to distinguish vegetable oils from gutter oils.

Keywords: Pyrolysis; Gutter oil; GC/MS; Waste oil; Olefins

Introduction

In the past ten years, food safety issues related to the reuse of waste oil or grease (*i.e.*, gutter oil) have been frequently exposed [1]. It is estimated that the regenerated waste oil accounts for up to 10% of the cooking oil market, *i.e.*, about 2.5 to 3 million tons of waste oil returns to the dining table every year [2]. As edible oils are a necessity in everyday life, the National Health Department of China began to focus on strengthening the techniques to detect and analyze edible oils.

In addition to the conventional physical and chemical indicators, the current detection/analytical methods of waste oils include various chromatographic methods, spectroscopy, nuclear magnetic resonance, etc. [3-5]. However, due to the complicated sources of waste oil, the complex composition, different processing methods, and different refining degrees, there is no single specific indicator or standard to distinct waste oils from edible oils. Consequently, it is imperative to develop a standard analytical method for the detection of the waste oil.

Because of the high boiling point, food oils are hardly to be analyzed directly. Therefore, the oil or grease is usually methylated and then analyzed by gas chromatography (GC) or gas chromatography coupled with mass spectrometry (GC/MS) [6]. In terms of the pyrolysis-gas chromatography/mass spectrometry (Py-GC/MS)

*Corresponding author: qqiu@szu.edu.cn

technology, oils can be directly pyrolyzed and the small molecules produced by the pyrolysis process are further identified by GC/MS [7]. The obtained pyrolytic products are a very intuitive reflection of the cracked fragments of the oil, which is equivalent to a series of changes in the simulated oil under pyrolytic temperature conditions [8]. The pyrolysis reactor adopts a vertical micro-furnace structure to measure the temperature of the sample in real time. The pyrolysis results demonstrate good reproducibility and overcome the deficiency of easy loss of high-boiling substances, which is conducive to obtaining more accurate analysis results [9].

In this study, eleven different oil samples were collected. The samples included vegetable oils (tea oil, olive oil, peanut oil, corn oil, sunflower oil, and blend vegetable oil), animal fat/oils (lard and chicken fat), and some low-quality oils (used frying oil, kitchen waste grease, and inferior oil). Py-GC/MS was conducted to analyze the pyrolytic products and characteristic peaks of oils from different sources.

Materials and Methods

Sample Collection and Preservation

The samples of this study mainly included two categories: edible vegetable oils and waste oils (used frying oil, lard, chicken fat, inferior oil and kitchen waste grease). The edible vegetable oils were purchased from the supermarket. The used frying oil and animal oils (chicken fat and lard) were collected from the home kitchen following cooking. The inferior oil with a very low price was purchased from the market. The waste grease was collected from the dining hall of the University. The sample names and the sources are summarized in Table 1. All samples were stored at room temperature.

Table 1. The oil samples from different sources*

Number	Name	Brand or Source
1	Sunflower seed oil	Jinlongyu [®]
2	Corn oil	Jinlongyu [®]
3	Peanut oil	Hujihua [®]
4	Olive oil	Geely Tree [®]
5	Tea oil	Jingangshan [®]
6	Blend vegetable oil	Maidelong [®]
7	Frying oil	Home kitchen after cooking
8	Inferior oil	Market place
9	Waste grease	Dining hall of the University
10	Lard	Home kitchen after cooking
11	Chicken fat	Home kitchen after cooking

*The oil samples of 7 to 11 satisfied with the definition of the gutter oil or the waste oil.

Pretreatment of Oil Samples

The oil samples of 9-11 (*i.e.*, waste grease, lard, and chicken fat) contained a small amount of water. Therefore, a pretreatment was conducted to remove the moisture from these oils. Firstly, an appropriate amount of oil sample was poured into the centrifuge tube, and then an appropriate amount of anhydrous sodium sulfate was added to the centrifuge tube. The centrifuge tube was vortexed and the water absorption of the sodium sulfate can be observed. In case, if there is no floating matter aggregates, it is still necessary to add a small amount of sodium sulfate until granular particles appeared.

Finally, the centrifuge tube was centrifuged at 3000×G for 20 minutes. Then, the supernatant was carefully collected as the pretreated oil sample.

Pyrolysis Coupled with Gas Chromatograph/Mass Spectrometer (Py-GC/MS)

Pyrolysis of oil samples was conducted in a sample cup of Frontier PY-2020iD pyrolyzer (Fukushima, Japan). For each experiment, the pyrolyzer was pre-heated to the desired temperature (300°C, 400°C, 500°C or 600°C), and then purged with ultra-purity helium to remove oxygen. A certain amount of samples (0.1 μL, 0.3 μL, or 0.5 μL) was allowed to drop into the pyrolyzer, whereby the sample was pyrolyzed for 30 s, 1 min, 3 min or 5 min. The volatilized products were injected directly into a Shimadzu GCMS-QP2010 gas chromatograph/mass spectrometer (Shimadzu, Japan) equipped with a Frontier Ultra-Allov5 capillary column (Fukushima, Japan).

For GC/MS analysis, the carrier gas of helium (99.999% purity) with a flow rate of 1 mL·min⁻¹ and the split ratio of 50:1 were used. The inlet temperature of GC was maintained at 300°C. The temperature of the GC oven was initially set at 35°C and held at 35°C for 2 min, then ramped to 350°C at a rate of 15 °C·min⁻¹ and held at 350°C for 10 min. The pyrolytic products were identified by comparison with the NIST mass spectral library (National Institute of Standards and Technology, USA). The distribution of compounds was calculated as the peak area percentage.

Results and Discussions

This study attempted to optimize the detection method of the waste oils, mainly from the three influencing factors of pyrolysis temperature, the sample amount, and the pyrolysis residence time. The pyrolysis temperature refers to the temperature whose sample is pyrolyzed in the pyrolysis furnace, *i.e.*, the temperature before entering the GC column.

Determination of Pyrolysis Reaction Conditions

Impact of Pyrolysis Temperature

The direct pyrolysis of the waste oils without methyl esterification was performed by Py-GC/MS and the parameters were optimized accordingly. Firstly, the effect of the pyrolysis temperature was studied. Because the smoke point of edible oils starts at 170°C, a lower pyrolysis temperature of 150-200°C was first studied. However, it was found that the pyrolysis at the low temperature was difficult to obtain the volatile effluent, and almost no pyrolytic products appeared. Therefore, the pyrolysis temperature was further increased to 300°C, 400°C, 500°C and 600°C. Taking sunflower oil as an example, the experiments were carried out under the conditions of the sample volume of 1 μL and the pyrolysis time of 1 min. The total ion current (TIC) chromatograms are shown in Figures 1 and 2.

Comparison of Figure 1 with Figure 2 shows that as the pyrolysis temperature rose from 300°C to 600°C, the number of pyrolytic products gradually increased, resulting in more peaks on the TIC chromatogram. The resolution was higher at 600°C which is determined as the optimal pyrolysis temperature in this study.

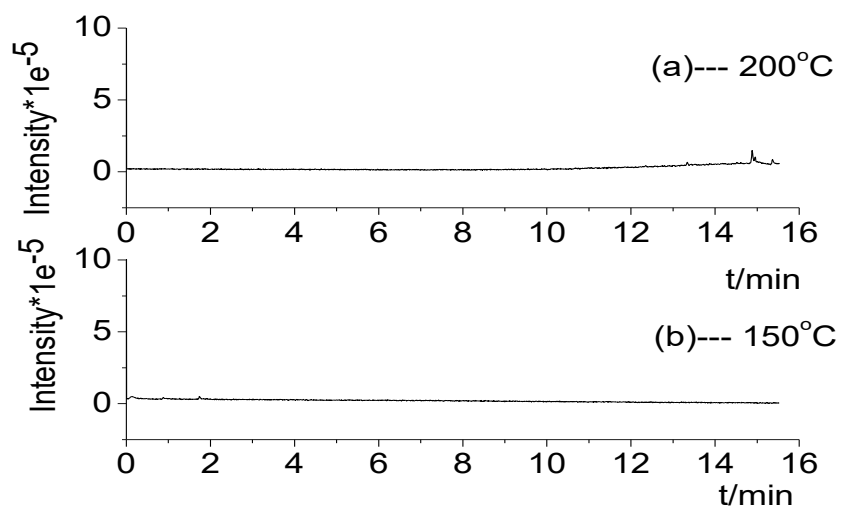


Figure 1. The pyrolysis TIC chromatogram of sunflower oil at (a) 200°C, (b) 150°C

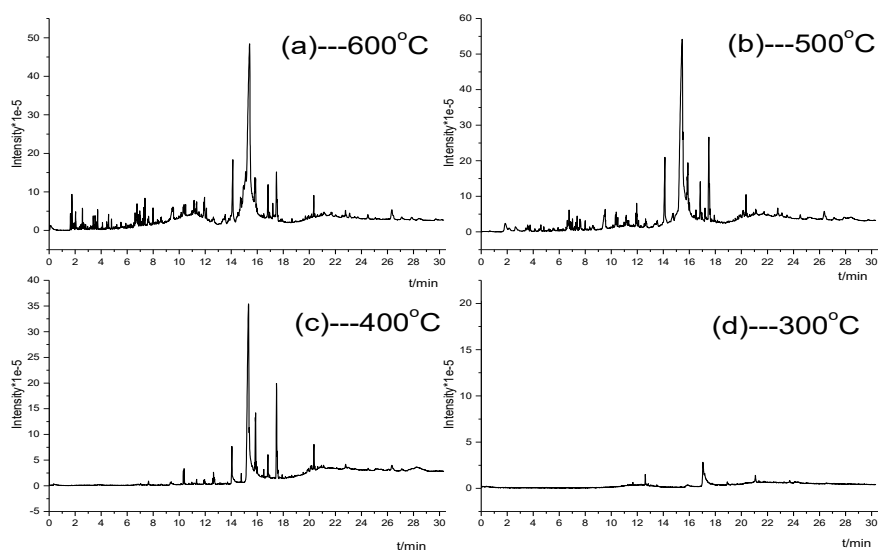


Figure 2. The pyrolysis TIC chromatogram of sunflower oil at (a) 600°C, (b) 500°C, (c) 400°C and (d) 300°C

Optimization of Sample Volume

To optimize the sample volume of pyrolysis, the oil samples of 0.1 μL , 0.3 μL and 0.5 μL were injected into the Py-GC/MS. After each pyrolysis, a blank experiment was performed under the same reaction conditions to check the residue remaining in the GC column. Taking the peanut oil as an example, all experiments were conducted at the pyrolysis temperature of 600°C for 1 min. The TIC chromatogram results are shown in Figures 3-5.

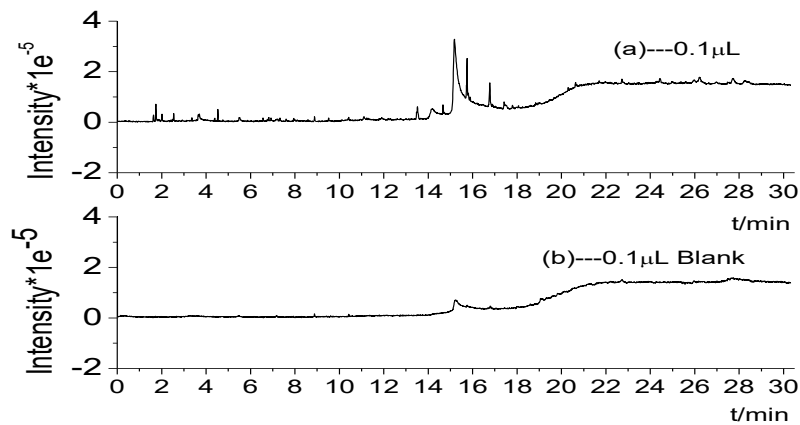


Figure 3. The pyrolysis TIC chromatogram of 0.1 µL peanut oil and the blank analysis after pyrolysis

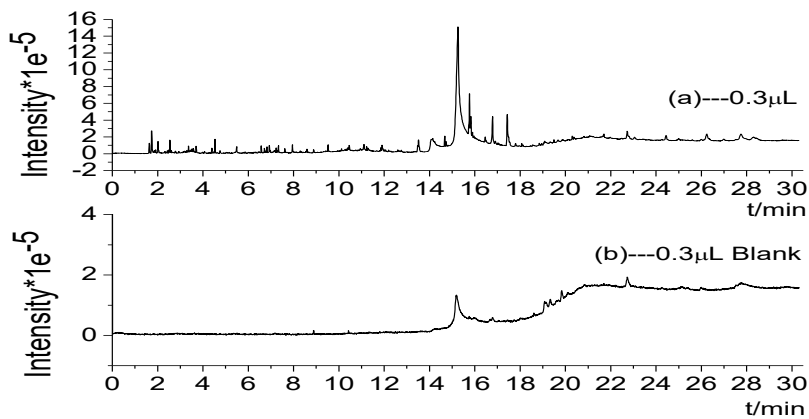


Figure 4. The pyrolysis TIC chromatogram of 0.3 µL peanut oil and the blank analysis after pyrolysis

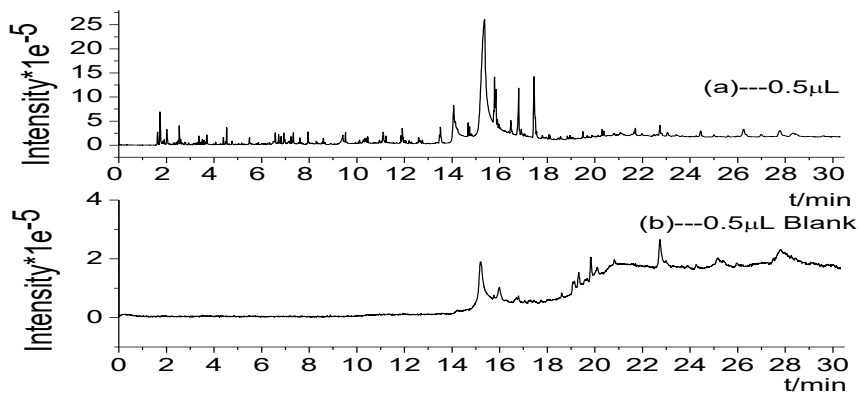


Figure 5. Pyrolysis TIC chromatogram of 0.5 µL peanut oil and the blank analysis after pyrolysis

The comparison with the blank chromatogram after pyrolysis shows that when the injection volume was 0.1 µL and 0.3 µL, the amount of residue in the GC column was

relative negligible. When the injection volume increased to 0.5 μL , the amount of residue in the column was more evident. This may affect the analytic results of the following samples. Additionally, the peaks of the TIC chromatogram were not clear for the sample injection of 0.1 μL . Therefore, the optimal injection volume was determined as 0.3 μL in this study.

Optimization of Pyrolysis Reaction Time

Pyrolysis time was investigated at the pyrolysis temperature of 600°C and an injection volume of 0.3 μL . Times studied were 30 s, 1 min, 3 min, and 5 min. The TIC chromatogram in Figure 6 shows very similar results under the reaction time of 0.5 to 5 min. However, when the pyrolysis time was greater than 1 min, the peak intensities of the total ion current were more evident than those of 0.5 min. Accordingly, the optimal pyrolysis time was determined as 1 min.

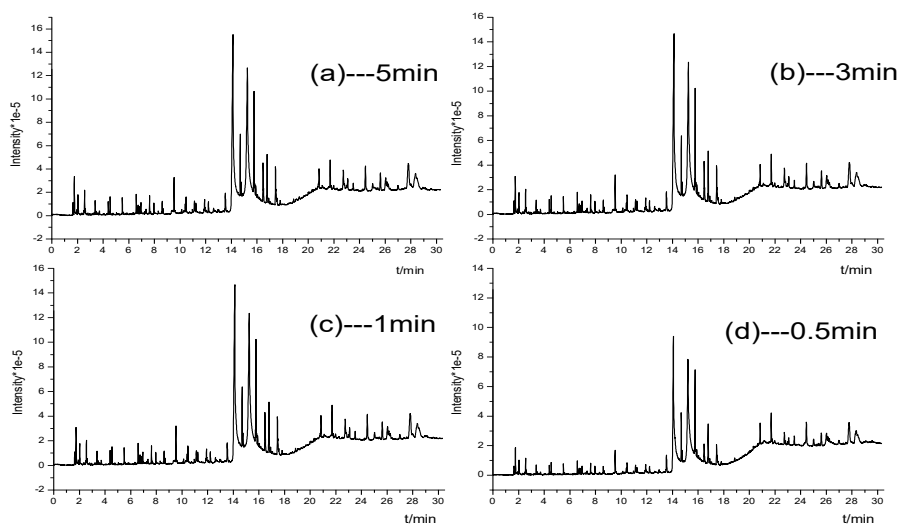


Figure 6. The pyrolysis TIC chromatogram of the inferior oil for (a) 5 min, (b) 3 min, (c) 1 min, (d) 0.5 min

Pyrolysis of Oils from Different Sources

The oil samples including tea oil, olive oil, peanut oil, corn oil, sunflower oil, vegetable blend oil, used frying oil, lard, chicken fat, inferior oil and kitchen waste grease were pyrolyzed at 600°C and a volume of 0.3 μL for 1 min. The TIC results are shown in Figures 7-17.

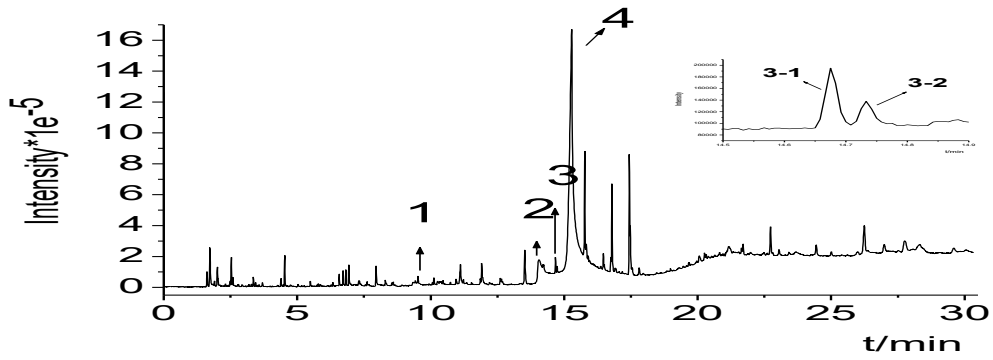


Figure 7. The pyrolysis TIC chromatogram of the tea oil

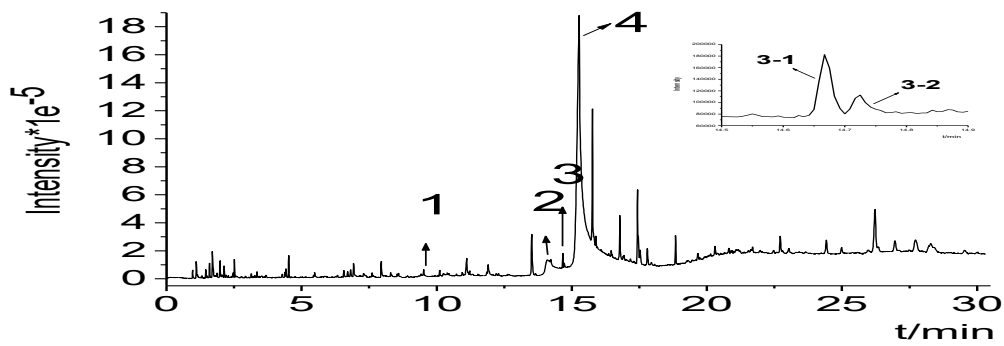


Figure 8. The TIC chromatogram of pyrolysis of the olive oil

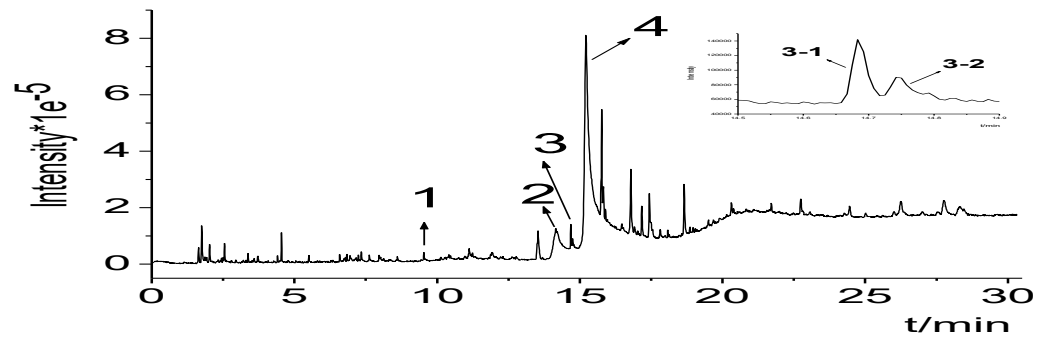


Figure 9. The pyrolysis TIC chromatogram of the peanut oil

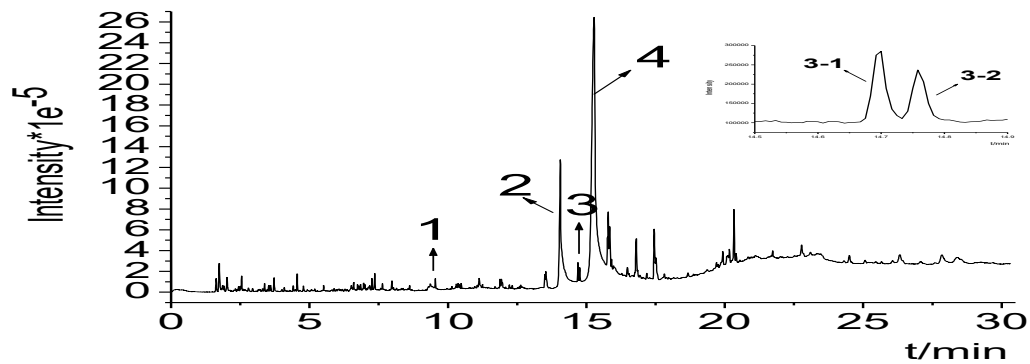


Figure 10. The pyrolysis TIC chromatogram of the corn oil

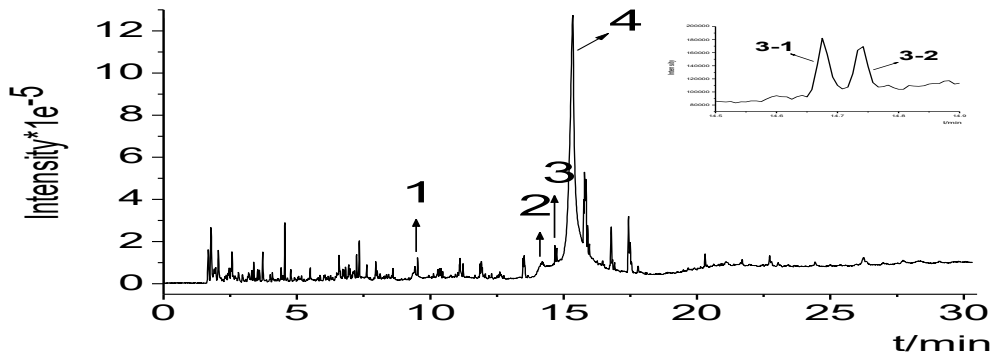


Figure 11. The pyrolysis TIC chromatogram of the sunflower oil

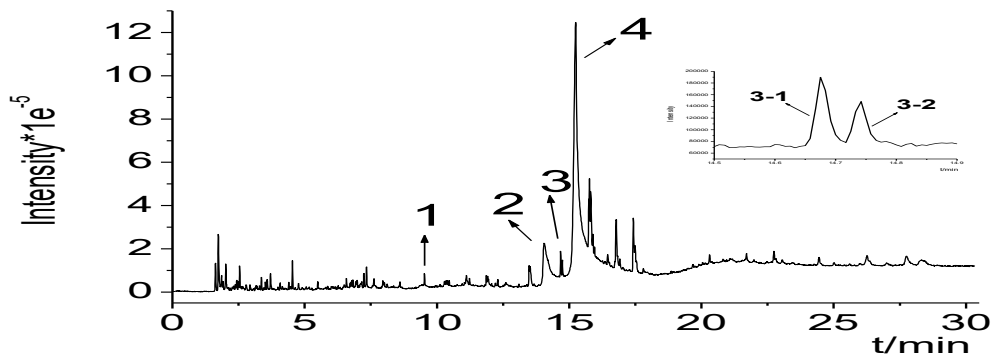


Figure 12. The TIC chromatogram results of pyrolysis of the blend vegetable oil

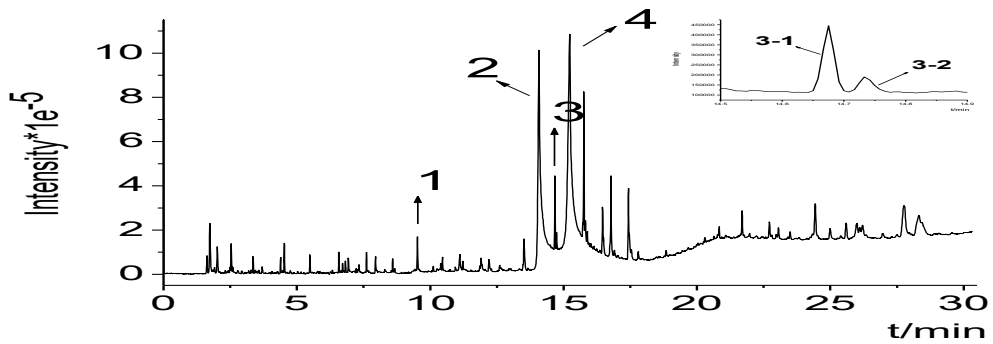


Figure 13. The pyrolysis TIC chromatogram of the used frying oil

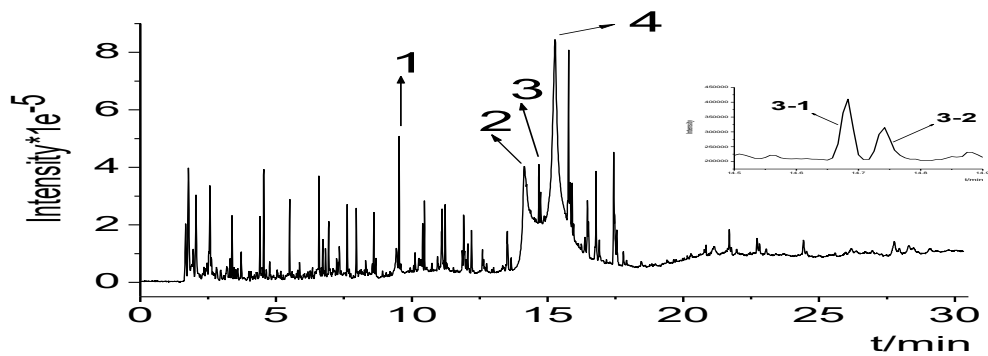


Figure 14. The pyrolysis TIC chromatogram of the lard

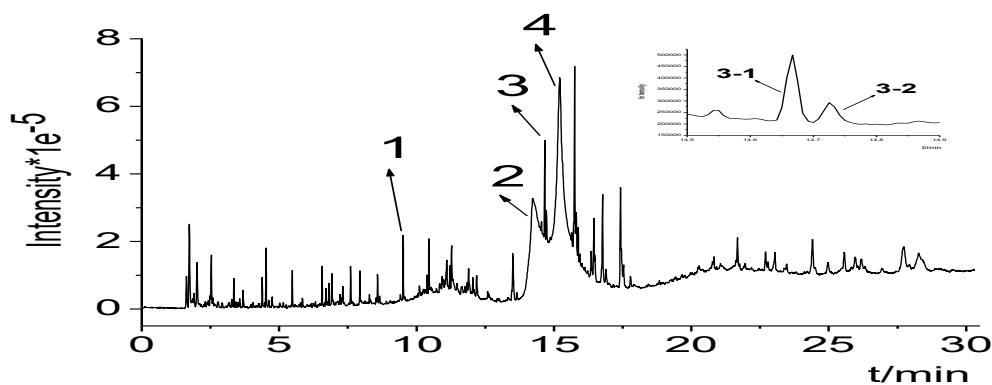


Figure 15. The pyrolysis TIC chromatogram of the chicken fat

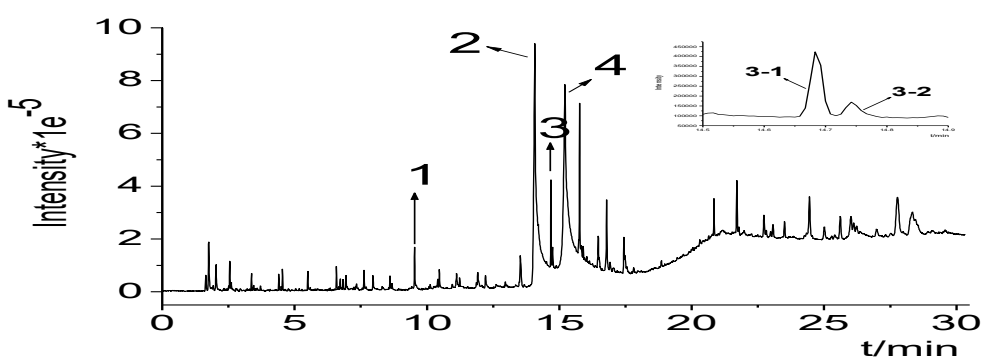


Figure 16. The pyrolysis TIC chromatogram of the inferior oil

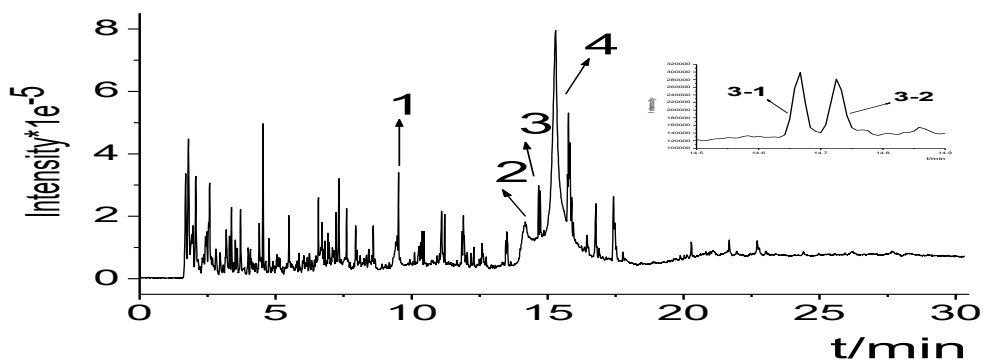


Figure 17. The pyrolysis TIC chromatogram of the kitchen waste grease

The TICs of all oil samples were quite complicated in terms of the number of peaks and the peak shape. Because vegetable oils or animal oils are essentially fatty acid glycerides, the resulting TICs after pyrolysis were very similar. Nevertheless, the TICs of oil samples from different sources could be distinguished by either the retention time for different compounds or the peak height/area for the same compound.

A specific peak, named as Peak 1 was observed at the retention time of 9.5 min. This peak was identified as tetradecane by searching through the NIST library. The comparison of Peak 1 of different oil samples is listed in Table 5.

Table 5. Comparison of Peak 1 of different samples

Sample	Retention time (min)	Peak area	Peak height	Similarity
Tea oil	9.524	6.74E+04	7.30E+04	92%
Olive oil	9.518	4.94E+04	6.69E+04	92%
Peanut oil	9.535	3.50E+04	4.17E+04	90%
Corn oil	9.545	1.14E+05	1.32E+05	92%
Sunflower oil	9.527	1.11E+05	1.24E+05	92%
Blend vegetable oil	9.529	8.60E+04	8.58E+04	92%
Used frying oil	9.519	2.31E+05	1.71E+05	96%
Chicken fat	9.51	2.52E+05	5.10E+05	97%
Lard	9.532	5.65E+05	2.21E+05	96%
Inferior oil	9.532	2.10E+05	1.70E+05	96%
Kitchen waste grease	9.517	3.38E+05	3.42E+05	95%

The area of Peak 1 of all edible vegetable oils was less than $2.0E+05$, and the peak height was less than $1.50E+05$. And the similarity of all edible vegetable oils in this peak was less than 92%, while the results of animal oils, used frying oil, inferior oil, and kitchen waste grease showed opposite trends. This feature may be employed as an evaluation indicator to distinguish vegetable oils from lard, chicken fat, kitchen waste grease, and inferior oil.

Two other distinct peaks appeared between 14 and 16 minutes were marked as Peak 2 and 4, respectively. These two peaks showed obvious higher peak intensities. A smaller peak between Peak 2 and 4 was marked as Peak 3. To be more specific, Peak 3 could be distinguished into two very close small peaks, labeled as Peaks 3-1 and 3-2. The height of these peaks of various oil samples is summarized in Table 6.

Table 6. The height of Peak 2, 3 and 4 of various oils and fats

Sample	H#2	H#3-1	H#3-2	H#4	Ratio of H#4/H#2
Tea oil	1.79E+05	1.95E+05	1.37E+05	1.67E+06	9.33
Olive oil	1.36E+05	1.82E+05	1.13E+05	1.89E+06	13.90
Peanut oil	1.28E+05	1.42E+05	9.47E+04	8.16E+05	6.38
Corn oil	1.27E+06	2.84E+05	2.43E+05	2.65E+06	2.09
Sunflower oil	1.06E+05	1.84E+05	1.69E+05	1.27E+06	11.98
Blend vegetable oil	2.27E+05	1.89E+05	1.48E+05	1.25E+06	5.51
Used frying oil	1.01E+06	4.50E+05	1.91E+05	1.09E+06	1.08
Chicken fat	4.04E+05	4.12E+05	3.18E+05	8.46E+05	2.09
Lard	3.33E+05	5.00E+05	2.92E+05	6.84E+05	2.05
Inferior oil	9.48E+05	4.25E+05	1.70E+05	1.86E+05	0.20
Kitchen waste grease	1.87E+05	3.04E+05	2.86E+05	7.95E+05	4.25

H: the peak height; #: the peak number

For most vegetable oils, the height of Peak 2 was shorter, but the height of Peak 4 was higher. In terms of the peak height ratio of these two peaks, the ratio of H#4/H#2 was the largest for vegetable oils. For animal oils and other low-quality oils, this ratio was small. For example, the height of Peak 2 of the inferior oil was slightly higher than that of Peak 4 with a ratio of 0.20. However, corn oil and kitchen waste oil did not

conform to the above rules. This ratio (2.09) for corn oil was not as large as other vegetable oils, while kitchen waste grease had a sufficient height difference with a ratio of 4.25. The height of Peak 3-2 of all oils and fats peaks was relatively close. But the height of Peak 3-1 was obviously different, *i.e.*, the peak heights of all edible vegetable oils were less than $3.00E+05$ and others were greater than $3.00E+05$. Therefore, edible vegetable oils can be distinguished from other fats.

Analysis of Pyrolytic Products of Oils from Different Sources

Because the structure of the pyrolytic products following Peak 4 was relatively complex and the similarities of the corresponding chemicals were low, this study specifically analyzed the pyrolytic products prior to Peak 4 and compared the similarity of various oils. The main ingredients (about 90%) are listed in the following Tables 7-17.

Table 7. Analysis of the pyrolytic products of tea oil

No.	Possible chemical	Similarity	Molecular Weight	Formula	Retention time
1	2-Acrylic aldehyde	96%	56	C ₃ H ₄ O	1.725
2	Cyclopentene	92%	68	C ₅ H ₈	1.9
3	Hexene	97%	84	C ₆ H ₁₂	2.009
4	Cyclohexene	94%	82	C ₆ H ₁₀	2.492
5	Heptene	98%	98	C ₇ H ₁₄	2.533
6	Octene	95%	112	C ₈ H ₁₆	3.358
7	E-1,4-octadiene	90%	110	C ₈ H ₁₄	3.7
8	Nonene	95%	126	C ₉ H ₁₈	4.392
9	Cyclooctene	98%	110	C ₈ H ₁₄	4.534
10	Decene	93%	140	C ₁₀ H ₂₀	5.492
11	1-Undecene	95%	154	C ₁₁ H ₂₂	6.575
12	2-Undecene	95%	154	C ₁₁ H ₂₂	6.717
13	1,4-Undecene	91%	152	C ₁₁ H ₂₀	6.933
14	E-1,8-Dodecadiene	91%	166	C ₁₂ H ₂₂	7.949
15	Tetradecene #1	92%	196	C ₁₄ H ₂₈	9.524
16	8-heptadecene	97%	238	C ₁₇ H ₃₄	11.908
17	Cis-9-hexadecenal	96%	238	C ₁₆ H ₃₀ O	13.525
18	Z,Z-9,12-octadecadienoic acid#2	87%	282	C ₁₈ H ₃₄ O ₂	14.042
19	Decanoic acid-2-propenyl ester#3-1	85%	212	C ₁₃ H ₂₄ O ₂	14.2
20	17-octadecenoic acid #3-2	86%	282	C ₁₈ H ₃₄ O ₂	14.233
21	Z-9-octadecenoic acid #4	96%	282	C ₁₈ H ₃₄ O ₂	15.284

#1---Peak 1; #2---Peak 2; #3-1---Peak 3-1; #3-2---Peak 3-2; #4---Peak 4

Table 8. Analysis of the pyrolytic products of olive oil

No.	Possible chemical	Similarity	Molecular Weight	Formula	Retention time
1	2-Acrylic aldehyde	94%	56	C ₃ H ₄ O	1.7
2	Hexene	96%	84	C ₆ H ₁₂	1.982
3	Heptene	97%	98	C ₇ H ₁₄	2.515
4	Octene	93%	112	C ₈ H ₁₆	3.35
5	Nonene	93%	126	C ₉ H ₁₈	4.382
6	Cyclooctene	97%	110	C ₈ H ₁₄	4.524
7	Decene	88%	140	C ₁₀ H ₂₀	5.483
8	Undecene	93%	154	C ₁₁ H ₂₂	6.566
9	2-Undecene	93%	154	C ₁₁ H ₂₂	6.699
10	E-1,4-Undecadiene	91%	152	C ₁₁ H ₂₀	6.926
11	E-1,8-Dodecadiene	90%	166	C ₁₂ H ₂₂	7.951
12	2E,4Z-Dodecadiene	93%	166	C ₁₂ H ₂₂	8.291
13	E-7-tetradecene	90%	196	C ₁₄ H ₂₈	8.591
14	Tetradecene #1	92%	196	C ₁₄ H ₂₈	9.517
15	8-heptadecene	94%	238	C ₁₇ H ₃₄	11.899
16	Cis-9-hexadecenal	96%	238	C ₁₆ H ₃₀ O	13.518
17	Z,Z-9,12-octadecadienoic acid#2	90%	280	C ₁₈ H ₃₂ O ₂	14.092
18	Decanoic acid-2-propenyl ester#3-1	86%	212	C ₁₃ H ₂₄ O ₂	14.666
19	17-octadecenoic acid #3-2	87%	282	C ₁₈ H ₃₄ O ₂	14.725
20	Z-9-octadecenoic acid #4	92%	282	C ₁₈ H ₃₄ O ₂	15.274

Table 9. Analysis of the pyrolytic products of peanut oil

No.	Possible chemical	Similarity	Molecular Weight	Formula	Retention time
1	2-propenaldehyde	93%	56	C ₃ H ₄ O	1.75
2	Hexene	95%	84	C ₆ H ₁₂	2.025
3	Heptene	96%	98	C ₇ H ₁₄	2.55
4	Octene	93%	112	C ₈ H ₁₆	3.375
5	Nonene	90%	126	C ₉ H ₁₈	4.409
6	Cyclooctene	96%	110	C ₈ H ₁₄	4.542
7	Decene	90%	140	C ₁₀ H ₂₀	5.5
8	Undecene	91%	154	C ₁₁ H ₂₂	6.591
9	6-Butyl-1,4-cycloheptadiene	89%	150	C ₁₁ H ₁₈	7.342
10	Dodecene	88%	168	C ₁₂ H ₂₄	7.626
11	Cetyl Alcohol	91%	242	C ₁₆ H ₃₄ O	9.533
12	Tetradecene #1	90%	196	C ₁₄ H ₂₈	9.535
13	Cis-9-hexadecenal	92%	238	C ₁₆ H ₃₀ O	13.533
14	Z,Z-9,12-octadecadienoic acid#2	87%	280	C ₁₈ H ₃₂ O ₂	14.158
15	Decanoic acid-2-propenyl ester#3-1	83%	212	C ₁₃ H ₂₄ O ₂	14.683
16	17-octadecenoic acid #3-2	86%	280	C ₁₈ H ₃₂ O ₂	14.742
17	Z-9-octadecenoic acid #4	88%	280	C ₁₈ H ₃₂ O ₂	15.209

Table 10. Analysis of the pyrolytic products of corn oil

No.	Possible chemical	Similarity	Molecular Weight	Formula	Retention time
1	2-Acrylic aldehyde	94%	56	C ₃ H ₄ O	1.733
2	Cyclopentene	92%	68	C ₅ H ₈	1.917
3	Hexene	97%	84	C ₆ H ₁₂	2.016
4	Cyclohexene	93%	82	C ₆ H ₁₀	2.508
5	Heptene	96%	98	C ₇ H ₁₄	2.55
6	3-methyl-cyclohexene	92%	96	C ₇ H ₁₂	2.942
7	Octene	93%	112	C ₈ H ₁₆	3.375
8	2-octene	94%	112	C ₈ H ₁₆	3.525
9	1,3-octadiene	94%	110	C ₈ H ₁₄	3.717
10	Nonene	91%	126	C ₉ H ₁₈	4.408
11	Cyclooctene	96%	110	C ₈ H ₁₄	4.55
12	1,3-nonadiene	90%	124	C ₉ H ₁₆	4.783
13	Decene	92%	140	C ₁₀ H ₂₀	5.508
14	Undecene	90%	154	C ₁₁ H ₂₂	6.6
15	6-Butyl-1,4-cycloheptene	92%	150	C ₁₁ H ₁₈	7.358
16	Dodecene	90%	168	C ₁₂ H ₂₄	7.633
17	Tridecene	91%	182	C ₁₃ H ₂₆	8.617
18	Tetradecene #1	92%	196	C ₁₄ H ₂₈	9.545
19	Cetyl Alcohol	92%	242	C ₁₆ H ₃₄ O	9.542
20	Z,Z-9,17-octadecadienal	93%	264	C ₁₈ H ₃₂ O	13.501
21	Cis-9-hexadecenal	92%	238	C ₁₆ H ₃₀ O	13.534
22	Z,Z-9,12-octadecadienoic acid#2	86%	284	C ₁₈ H ₃₆ O ₂	14.058
23	Decanoic acid-2-propenyl ester#3-1	86%	212	C ₁₃ H ₂₄ O ₂	14.7
24	17-octadecenoic acid #3-2	87%	254	C ₁₆ H ₃₀ O ₂	14.758
25	Z-9-octadecenoic acid #4	91%	280	C ₁₈ H ₃₂ O ₂	15.284

Table 11. Analysis of the pyrolytic products of sunflower oil

No.	Possible chemical	Similarity	Molecular Weight	Formula	Retention time
1	2-Acrylic aldehyde	93%	56	C ₃ H ₄ O	1.775
2	Cyclopentene	93%	66	C ₅ H ₈	1.95
3	Hexene	96%	84	C ₆ H ₁₂	2.059
4	Cyclohexene	95%	82	C ₆ H ₁₀	2.525
5	Heptene	97%	98	C ₇ H ₁₄	2.567
6	Octene	93%	112	C ₈ H ₁₆	3.383
7	2-octene	94%	112	C ₈ H ₁₆	3.525
8	1,3-octadiene	95%	110	C ₈ H ₁₄	3.717
9	Nonene	93%	126	C ₉ H ₁₈	4.408
10	Cyclooctene	98%	110	C ₈ H ₁₄	4.55
11	E-1,3-nonadiene	91%	124	C ₉ H ₁₆	4.767
12	Decene	93%	140	C ₁₀ H ₂₀	5.5
13	6-Butyl-1,4-cycloheptadiene	93%	150	C ₁₁ H ₁₈	7.342
14	3-dodecene	91%	166	C ₁₂ H ₂₄	7.616

15	Tridecene	91%	182	C ₁₃ H ₂₆	8.6
16	Tetradecene #1	92%	196	C ₁₄ H ₂₈	9.527
17	Z-6-pentadecenal	91%	226	C ₁₅ H ₃₀ O	10.35
18	Hexadecene	91%	224	C ₁₆ H ₃₂	11.225
19	9,17-octadecadienal	93%	264	C ₁₈ H ₃₂ O	13.475
20	Cis-9-hexadecenal	94%	238	C ₁₆ H ₃₀ O	13.516
21	Z,Z-9,12-octadecadienoic acid#2	88%	280	C ₁₈ H ₃₂ O ₂	14.2
22	Decanoic acid-2-propenyl ester#3-1	82%	212	C ₁₃ H ₂₄ O ₂	14.675
23	17-octadecenoic acid #3-2	87%	282	C ₁₈ H ₃₄ O ₂	14.741
24	Z-9-octadecenoic acid #4	89%	280	C ₁₈ H ₃₂ O ₂	15.335

Table 12. Analysis of the pyrolytic products of the blend vegetable oil

No.	Possible chemical	Similarity	Molecular Weight	Formula	Retention time
1	2-Acrylic aldehyde	95%	56	C ₃ H ₄ O	1.733
2	Hexene	97%	84	C ₆ H ₁₂	2.016
3	Heptene	97%	98	C ₇ H ₁₄	2.542
4	Octene	92%	112	C ₈ H ₁₆	3.367
5	2-octene	93%	112	C ₈ H ₁₆	3.509
6	1,3-octadiene	94%	110	C ₈ H ₁₄	3.708
7	Nonene	92%	126	C ₉ H ₁₈	4.4
8	Cyclooctene	97%	110	C ₈ H ₁₄	4.542
9	Decene	91%	140	C ₁₀ H ₂₀	5.492
10	6-Butyl-1,4-cycloheptene	92%	150	C ₁₁ H ₁₈	7.342
11	n-hexadecene	92%	224	C ₁₆ H ₃₂	9.525
12	Tetradecene #1	92%	196	C ₁₄ H ₂₈	9.529
13	Z-9,17-octadecadienal	94%	264	C ₁₈ H ₃₂ O	13.484
14	Z,Z-9,12-octadecadienoic acid#2	91%	280	C ₁₈ H ₃₂ O ₂	14.050
15	Decanoic acid-2-propenyl ester#3-1	86%	212	C ₁₃ H ₂₄ O ₂	14.675
16	17-octadecenoic acid #3-2	86%	282	C ₁₈ H ₃₄ O ₂	14.741
17	Z-9-octadecenoic acid #4	93%	280	C ₁₈ H ₃₂ O ₂	15.241

Table 13. Analysis of the pyrolytic products of used frying oil

No.	Possible chemical	Similarity	Molecular Weight	Formula	Retention time
1	2-Acrylic aldehyde	95%	56	C ₃ H ₄ O	1.733
2	Hexene	98%	84	C ₆ H ₁₂	2.016
3	Heptene	97%	98	C ₇ H ₁₄	2.542
4	Octene	95%	112	C ₈ H ₁₆	3.358
5	Nonene	96%	126	C ₉ H ₁₈	4.391
6	Cyclooctene	98%	110	C ₈ H ₁₄	4.525
7	Decene	95%	140	C ₁₀ H ₂₀	5.483
8	Undecene	96%	154	C ₁₁ H ₂₂	6.567
9	2-Undecene	93%	154	C ₁₁ H ₂₂	6.709
10	1,4-Undecadiene	90%	152	C ₁₁ H ₂₀	6.926
11	6-Butyl-1,4-cycloheptene	88%	150	C ₁₁ H ₁₈	7.326

12	Dodecene	96%	168	C ₁₂ H ₂₄	7.608
13	E-1,8-Dodecadiene	90%	166	C ₁₂ H ₂₂	7.95
14	Tridecene	95%	182	C ₁₃ H ₂₆	8.592
15	Tetradecene #1	96%	196	C ₁₄ H ₂₈	9.517
16	Pentadecene	92%	210	C ₁₅ H ₃₀	10.392
17	Pentadecane	93%	212	C ₁₅ H ₃₂	10.458
18	6-pentadecenol	94%	226	C ₁₅ H ₃₀ O	11.108
19	n-hexadecene	94%	224	C ₁₆ H ₃₂	11.226
20	8-heptadecene	94%	238	C ₁₇ H ₃₄	11.908
21	Cis-9-hexadecenal	96%	238	C ₁₆ H ₃₀ O	13.516
22	Z,Z-9,12-octadecadienoic acid#2	84%	284	C ₁₈ H ₃₆ O ₂	14.075
23	Decanoic acid-2-propenyl ester#3-1	87%	212	C ₁₃ H ₂₄ O ₂	14.675
24	17-octadecenoic acid #3-2	87%	282	C ₁₈ H ₃₄ O ₂	14.733
25	Z-9-octadecenoic acid #4	93%	282	C ₁₈ H ₃₄ O ₂	15.233

Table 14. Analysis of the pyrolytic products of chicken fat

No.	Possible chemical	Similarity	Molecular Weight	Formula	Retention time
1	2-Acrylic aldehyde	94%	56	C ₃ H ₄ O	1.733
2	Hexene	97%	84	C ₆ H ₁₂	2.009
3	Heptene	97%	98	C ₇ H ₁₄	2.534
4	Octene	96%	112	C ₈ H ₁₆	3.35
5	1,3-octadiene	94%	110	C ₈ H ₁₄	3.691
6	Nonene	97%	126	C ₉ H ₁₈	4.384
7	Cyclooctene	98%	110	C ₈ H ₁₄	4.525
8	Decene	96%	140	C ₁₀ H ₂₀	5.476
9	Undecene	96%	154	C ₁₁ H ₂₂	6.559
10	2-Undecene	94%	154	C ₁₁ H ₂₂	6.7
11	1,4-Undecadiene	91%	152	C ₁₁ H ₂₀	6.916
12	6-Butyl-1,4-cycloheptadiene	90%	152	C ₁₁ H ₁₈	7.316
13	Dodecene	96%	168	C ₁₂ H ₂₄	7.6
14	E-1,8-Dodecadiene	90%	166	C ₁₂ H ₂₂	7.942
15	2E,4Z-Dodecadiene	90%	166	C ₁₂ H ₂₂	8.283
16	Tridecene	96%	182	C ₁₃ H ₂₆	8.584
17	Tetradecene #1	97%	196	C ₁₄ H ₂₈	9.509
18	Pentadecene	93%	210	C ₁₅ H ₃₀	10.383
19	Pentadecane	95%	212	C ₁₅ H ₃₂	10.449
20	6-pentadecenal	91%	226	C ₁₅ H ₃₀ O	11.101
21	Hexadecene	92%	224	C ₁₆ H ₃₂	11.217
22	8-heptadecene	93%	238	C ₁₇ H ₃₄	11.9
23	Octadecenal	94%	266	C ₁₈ H ₃₆ O	12.183
24	Cis-9-hexadecenal	96%	238	C ₁₆ H ₃₀ O	13.501
25	Z,Z-9,12-octadecadienoic acid#2	91%	282	C ₁₈ H ₃₄ O ₂	14.225
26	Decanoic acid-2-propenyl ester#3-1	86%	212	C ₁₃ H ₂₄ O ₂	14.667
27	17-octadecenoic acid #3-2	93%	282	C ₁₈ H ₃₄ O ₂	14.725
28	Z-9-octadecenoic acid #4	89%	282	C ₁₈ H ₃₄ O ₂	15.208

Table 15. Analysis of the pyrolytic products of lard

No.	Possible chemical	Similarity	Molecular Weight	Formula	Retention time
1	2-Acrylic aldehyde	91%	56	C ₃ H ₄ O	1.775
2	Cyclopentene	95%	66	C ₅ H ₈	1.95
3	Hexene	97%	84	C ₆ H ₁₂	2.05
4	Heptene	97%	98	C ₇ H ₁₄	2.567
5	Octene	96%	112	C ₈ H ₁₆	3.384
6	2-octene	90%	112	C ₈ H ₁₆	3.517
7	1,3-octadiene	93%	110	C ₈ H ₁₄	3.717
8	Nonene	97%	126	C ₉ H ₁₈	4.408
9	Cyclooctene	98%	110	C ₈ H ₁₄	4.55
10	1,3-nonadiene	91%	124	C ₉ H ₁₆	4.767
11	Decene	96%	140	C ₁₀ H ₂₀	5.5
12	Undecene	93%	154	C ₁₁ H ₂₂	6.583
13	2-Undecene	94%	154	C ₁₁ H ₂₂	6.724
14	1,4-Undecadiene	91%	152	C ₁₁ H ₂₀	6.942
15	6-Butyl-1,4-cycloheptene	89%	150	C ₁₁ H ₁₈	7.333
16	Dodecene	96%	168	C ₁₂ H ₂₄	7.616
17	E-1,8-Dodecadiene	91%	166	C ₁₂ H ₂₂	7.958
18	Tridecene	96%	182	C ₁₃ H ₂₆	8.6
19	Tridecane	92%	184	C ₁₃ H ₂₈	8.675
20	Tetradecene #1	96%	196	C ₁₄ H ₂₈	9.533
21	Pentadecene	95%	210	C ₁₅ H ₃₀	10.4
22	Pentadecane	96%	212	C ₁₅ H ₃₂	10.467
23	6-pentadecenol	93%	226	C ₁₅ H ₃₀ O	11.116
24	Hexadecene	96%	224	C ₁₆ H ₃₂	11.233
25	8-heptadecene	96%	238	C ₁₇ H ₃₄	11.908
26	Octadecenal	95%	266	C ₁₈ H ₃₆ O ₂	12.2
27	Cis-9-hexadecenal	95%	238	C ₁₆ H ₃₀ O	13.516
28	Z,Z-9,12-octadecadienoic acid#2	87%	282	C ₁₈ H ₃₄ O ₂	14.141
29	Decanoic acid-2-propenyl ester#3-1	82%	212	C ₁₃ H ₂₄ O ₂	14.683
30	17-octadecenoic acid #3-2	88%	282	C ₁₈ H ₃₄ O ₂	14.742
31	Z-9-octadecenoic acid #4	84%	282	C ₁₈ H ₃₄ O ₂	15.275

Table 16. Analysis of the pyrolytic products of inferior oil

No.	Possible chemical	Similarity	Molecular Weight	Formula	Retention time
1	2-Acrylic aldehyde	94%	56	C ₃ H ₄ O	1.758
2	Hexene	97%	84	C ₆ H ₁₂	2.034
3	Heptene	97%	98	C ₇ H ₁₄	2.55
4	Octene	96%	112	C ₈ H ₁₆	3.375
5	1,3-octadiene	87%	110	C ₈ H ₁₄	3.708
6	Nonene	96%	126	C ₉ H ₁₈	4.4
7	Cyclooctene	97%	110	C ₈ H ₁₄	4.542
8	Decene	96%	140	C ₁₀ H ₂₀	5.5

9	Undecene	95%	154	C ₁₁ H ₂₂	6.583
10	2-Undecene	93%	154	C ₁₁ H ₂₂	6.725
11	1,4-Undecadiene	91%	152	C ₁₁ H ₂₀	6.942
12	6-Butyl-1,4-cycloheptene	86%	150	C ₁₁ H ₁₈	7.342
13	Dodecene	96%	168	C ₁₂ H ₂₄	7.624
14	Tridecene	95%	182	C ₁₃ H ₂₆	8.6
15	Tetradecene #1	96%	196	C ₁₄ H ₂₈	9.534
16	Pentadecene	93%	210	C ₁₅ H ₃₀	10.408
17	Pentadecane	95%	212	C ₁₅ H ₃₂	10.467
18	6-pentadecenol	93%	226	C ₁₅ H ₃₀ O	11.116
19	n-hexadecene	92%	224	C ₁₆ H ₃₂	11.234
20	8-heptadecene	95%	238	C ₁₇ H ₃₄	11.917
21	Tetradecenal	95%	212	C ₁₄ H ₂₈ O	12.208
22	Cis-9-hexadecenal	96%	238	C ₁₆ H ₃₀ O	13.524
23	Z,Z-9,12-octadecadienoic acid#2	88%	284	C ₁₈ H ₃₆ O ₂	14.075
24	Decanoic acid-2-propenyl ester#3-1	86%	212	C ₁₃ H ₂₄ O ₂	14.683
25	17-octadecenoic acid #3-2	84%	282	C ₁₈ H ₃₄ O ₂	14.742
26	Z-9-octadecenoic acid #4	91%	282	C ₁₈ H ₃₄ O ₂	15.209

Table 17. Analysis of the pyrolytic products of kitchen waste grease

No.	Possible chemical	Similarity	Molecular Weight	Formula	Retention time
1	2-Acrylic aldehyde	90%	56	C ₃ H ₄ O	1.784
2	Cyclopentene	96%	68	C ₅ H ₈	1.966
3	Hexene	96%	84	C ₆ H ₁₂	2.067
4	Heptene	98%	98	C ₇ H ₁₄	2.575
5	Octene	93%	112	C ₈ H ₁₆	3.375
6	2-octene	93%	112	C ₈ H ₁₆	3.517
7	1,3-octadiene	96%	110	C ₈ H ₁₄	3.708
8	Nonene	94%	126	C ₉ H ₁₈	4.4
9	Cyclooctene	97%	110	C ₈ H ₁₄	4.542
10	E-1,3-nonadiene	92%	124	C ₉ H ₁₆	4.758
11	Decene	93%	140	C ₁₀ H ₂₀	5.483
12	Undecene	89%	154	C ₁₁ H ₂₂	6.576
13	1,4-Undecadiene	89%	152	C ₁₁ H ₂₀	6.925
14	6-Butyl-1,4-cycloheptene	90%	150	C ₁₁ H ₁₈	7.325
15	Dodecene	93%	166	C ₁₂ H ₂₄	7.608
16	Tridecene	92%	182	C ₁₃ H ₂₆	8.592
17	Tetradecene #1	95%	196	C ₁₄ H ₂₈	9.517
18	Pentadecene	91%	210	C ₁₅ H ₃₀	10.392
19	Pentadecane	91%	212	C ₁₅ H ₃₂	10.45
20	Hexadecene	93%	224	C ₁₆ H ₃₂	11.217
21	E,8-Heptadecene	90%	238	C ₁₇ H ₃₄	11.9
22	Cis-9-hexadecenal	93%	238	C ₁₆ H ₃₀ O	13.5
23	Z,Z-9,12-octadecadienoic acid#2	88%	280	C ₁₈ H ₃₂ O ₂	14.174
24	Decanoic acid-2-propenyl ester#3-1	82%	212	C ₁₃ H ₂₄ O ₂	14.667

25	17-octadecenoic acid #3-2	87%	282	C ₁₈ H ₃₄ O ₂	14.725
26	Z-9-octadecenoic acid #4	90%	280	C ₁₈ H ₃₂ O ₂	15.375

According to these results, during the first 6.5 minutes, the pyrolytic products of all oil samples were quite similar, most of which were small-molecule chemicals such as 2-acrolein, hexene, heptane, aldehydes, and olefins. Moreover, these substances had a higher similarity, mostly over 90%.

For animal fat/oils, inferior oil, and kitchen waste grease, pentadecane (C15) was observed at the retention time of 10.4 min, and the similarity was higher than 90%. Other vegetable oils did not show pentadecane in the pyrolytic products.

Peak 2 was identified as z,z-9,12-octadecadienoic acid, while Peak 3-1 was identified as decanoic acid-2-propenyl ester. Due to its low strength, Peak 3-2 was identified as 17-octadecenoic acid, but the potential was low. For the used frying oil, animal fat/oils, and inferior oil, Peak 4 was mainly z-9-octadecenoic acid. But Peak 4 of vegetable oils could also be a mixture of z-9-octadecenoic acid and z,z-9,12-octadecadienoic acid.

As shown in the mass spectrum, not all olefins having a carbon number higher than 11 (undecane) were present in the pyrolytic products of vegetable oils. For example, dodecane, tridecane, and pentadecene were absent from the products of tea oil, olive oil, and peanut oil. But the products from animal fats, used frying oil, and inferior oil contained all kinds of C11-16 olefins (Table 18). The possible reason is that these oils have been used and recovered, wherein the C16-C18 fatty acids were degraded to a certain degree. So, the pyrolytic products of these low-quality oils contained all kinds of olefins. This can be used as a key indicator to distinguish inferior oils and animal fats from vegetable oils.

Table 18. Olefin present in the products

Oil	Undecene C11	Dodecene C12	Tridecene C13	Tetradecene C14	Pentadecene C15	Hexadecene C16
Tea oil	√			√		√
Olive oil	√			√		
Peanut oil	√	√		√		
Corn oil	√	√	√	√		
Sunflower oil			√	√		√
Blend vegetable oil				√		√
Used frying oil	√	√	√	√	√	√
Chicken fat	√	√	√	√	√	√
Lard	√	√	√	√	√	√
Inferior oil	√	√	√	√	√	√
Kitchen waste grease	√	√	√	√	√	√

CONCLUSIONS

The pyrolysis conditions of oil samples were optimized as the pyrolysis temperature of 600°C, the sample volume of 0.3 μL, and the reaction time of 1 min. According to the TIC of Py-GC/MS, when the retention time was less than or equal to 6.5

min, the pyrolytic products of all oil samples were similar. But at the retention time of 9.5 min, the area of Peak 1 (tetradecene) of the vegetable oils was less than $2.00E+05$ and the peak high was lower than $1.50E 05$. Dodecane, tridecane, and pentadecene were absent from the products of tea oil, olive oil, and peanut oil. The pyrolytic products from animal oils, used frying oil, inferior oil and kitchen waste grease contained C11-C16 olefins. Therefore, the Py-GC/MS technology could be used to distinguish vegetable oils from animal fat/oil, inferior oil, and kitchen waste grease.

ACKNOWLEDGMENTS

This work was partially supported by Natural Science Foundation of Guangdong Province (2017A030310133) and the College of Chemistry and Environmental Engineering at Shenzhen University.

CONFLICTS OF INTEREST

The authors declare that there is no conflict of interests regarding the publication of this paper.

REFERENCES

- [1] Li, J., Cui, N., and Liu, J. (2017). Gutter oil: an overview of Chinese food safety issues and policies. *Global Health Promotion*, 24(3), 75-78. DOI: 10.1177/1757975915623733
- [2] Lu, F., and Wu, X. (2014). China food safety hits the “gutter”. *Food Control*, 41, 134-138. DOI: <https://doi.org/10.1016/j.foodcont.2014.01.019>
- [3] López-Díez, E. C., Bianchi, G., and Goodacre, R. (2003). Rapid Quantitative Assessment of the Adulteration of Virgin Olive Oils with Hazelnut Oils Using Raman Spectroscopy and Chemometrics. *Journal of agricultural and food chemistry*, 51(21), 6145-6150. DOI: 10.1021/jf034493d
- [4] Lin, C., Liao, C., Zhang, Y., Xu, L., Wang, Y., Fu, C., Yang, K., Wang, J., He, J., and Wang, Y. (2018). Optofluidic gutter oil discrimination based on a hybrid-waveguide coupler in fibre. *Lab on a Chip*, 18(4), 595-600. DOI: 10.1039/c8lc00008e
- [5] Tian, K., Wang, W., Yao, Y., Nie, X., Lu, A., Wu, Y., and Han, C. (2018). Rapid identification of gutter oil by detecting the capsaicin using surface enhanced Raman spectroscopy. *Journal of Raman Spectroscopy*, 49(3), 472-481. DOI: <https://doi.org/10.1002/jrs.5306>
- [6] Zhang, B., Wu, J., Yang, C., Qiu, Q., Yan, Q., Li, R., Wang, B., Wu, J., and Ding, Y. (2018). Recent Developments in Commercial Processes for Refining Bio-Feedstocks to Renewable Diesel. *BioEnergy Research*, 11(3), 689-702. DOI: 10.1007/s12155-018-9927-y
- [7] Qiu, Q., Cai, Y., Ye, Q., and Lv, W. (2019). Catalytic Pyrolysis of Kapok Fiber for Production of Olefins. *Trends in Renewable Energy*, 5(2), 218-228. DOI: 10.17737/tre.2019.5.2.0097
- [8] Zhang, B., and Wang, Y. (2013). *Biomass Processing, Conversion and Biorefinery*, Nova Science Publishers, Inc., New York.

- [9] Yang, C., Li, R., Qiu, Q., Yang, H., Zhang, Y., Yang, B., Wu, J., Li, B., Wang, W., Ding, Y., and Zhang, B. (2020). Pyrolytic behaviors of *Scenedesmus obliquus* over potassium fluoride on alumina. *Fuel*, 263, 116724. DOI: <https://doi.org/10.1016/j.fuel.2019.116724>

Article copyright: © 2021 Qi Qiu, Yiting Zhang. This is an open access article distributed under the terms of the [Creative Commons Attribution 4.0 International License](https://creativecommons.org/licenses/by/4.0/), which permits unrestricted use and distribution provided the original author and source are credited.



Exergy and Energy Analysis of Wind-Thermal System

Nima Norouzi*

Department of Energy Engineering and Physics, Amirkabir University of Technology (Tehran Polytechnic),
424 Hafez Avenue, PO Box 15875-4413, Tehran, Iran

Received August 3, 2021; Accepted August 25, 2021; Published August 30, 2021

Current wind systems are intermittent and cannot be used as the baseload energy source. The research on the concept of wind power using direct thermal energy conversion and thermal energy storage, called wind powered Thermal Energy System (WTES), opened the door to a new energy system called Wind-thermal, which is a strategy for developing baseload wind power systems. The thermal energy is generated from the rotating energy directly at the top of the tower by the heat generator, which is a simple and light electric brake. The rest of the system is the same as the tower type concentrated solar power (CSP). This paper's results suggest that the energy and exergy performance of the WTES (62.5% and 29.8%) is comparable to that of conventional wind power, which must be supported by the backup thermal plants and grid enhancement. This cogeneration nature of the WTES system makes this system suitable for using wind power as a direct heat source in several heat-demanding processes such as chemical production. Also, the light heat generator reduces some issues of wind power, such as noise and vibration, which are two main bottlenecks of the wind power technology.

Keywords: ORC cycle; Wind turbine; Energy analysis; Wind Thermal; Exergy analysis

Introduction

Due to the industrialization of most cities, energy demand grew significantly. The continuous increase in energy demand has led to the widespread use of carbon-containing fossil fuels, which has caused significant damage to the environment and human health. In recent years, many efforts and programs have been made to reduce the use of fossil fuels. Renewable energy sources such as solar and wind energy have been introduced as reliable sources for clean energy production for use. Solar power plant technology using parabolic-linear concentrators is the most significant method among thermal-electric methods for renewable energy production.

Recently, Gupta *et al.* [1] proposed a system consisting of an organic Rankin cycle with a triple pressure level absorption system and a parabolic-linear solar collector system in 2020. This system generates electricity and refrigeration simultaneously at two different temperatures. In this study, the effect of different inlet parameters such as solar radiation, turbine inlet pressure, turbine outlet pressure, and evaporator temperature on the designed schematic subsystems was investigated. Kerme *et al.* [2] thermodynamically analyzed a multiple power generation system using the thermal energy from a solar system with a parabolic-linear solar collector. The results showed that increasing the turbine inlet temperature increased the efficiency and decreased overall energy losses.

*Corresponding author: n.nima1376@gmail.com

The results also showed that the two main sources of exergy losses are the solar system and the desalination unit.

Alirahmi *et al.* [3] proposed a multiple generation system based on the geothermal energy and a parabolic-linear solar collector system for simultaneous electricity generation, cooling load, freshwater, hydrogen, and heat. To optimize the objectives of their research, EES (engineering equation solver) and MATLAB software were interconnected using the Dynamic Exchange Data method. Finally, the system exergy efficiency and total unit cost were 29.95% and 129.7 \$/GJ, respectively. Alotaibi *et al.* [4] investigated the performance of a conventional steam power plant with a regenerative system equipped with a parabolic-linear solar collector system. The system analysis results showed that the removal of the low-pressure (LP) turbine increases the performance of the steam power plant up to 9.8 MW/h. The optimal area for the solar system in these conditions was estimated at 25,850 square meters. Ehyaei *et al.* [5] conducted thermodynamic analysis, energy and exergy, and economic analysis on a linear parabolic solar collector. The optimization results showed that the exergy efficiency, energy efficiency, and costs were 29.29%, 35.55%, and \$0.0142/kWh, respectively. Toghyani *et al.* [6] used a nanofluid as a cooling fluid in a parabolic-linear solar collector to cool the solar system and produce hydrogen. The results showed that hydrogen production increases under higher solar intensities because the Rankin cycle transfers more energy to the PEM.

AlZahrani and Dincer [7], in 2018, studied the energy and exergy of parabolic-linear solar collectors as part of a solar power plant under different design and performance conditions. Finally, the energy and exergy efficiency rates of 35.66% and 38.55% were reported, respectively. In 2019, Yilmaz [8] reviewed the comprehensive thermodynamic performance and economic evaluation of a combined ocean thermal energy system and a wind farm. The results showed that the hybrid system's overall energy and exergy efficiencies are 12.27% and 34.34%, respectively. The cost of the proposed system was reported to be \$3.03 per hour. Ishaq and Dincer [9] proposed a new idea for hydrogen production from methanol using the wind energy. The proposed system used industrial carbon emissions to produce methanol. EES and Aspen Plus software was used to model the system and comprehensively analyze it. Bamisile *et al.* [10] modeled a power generation system using wind, solar and biogas energy, and analyzed the energy and exergy of the system. The results showed that the system's overall energy efficiency varies from 64.91% to 71.06%, while the exergoeconomic efficiency increases from 31.80% to 53.81%. In 2018, Kianfard *et al.* [11] investigated a renewable system based on thermal energy to produce fresh water and hydrogen. The economic analysis results showed that the investment costs per unit of reverse osmosis desalination plant were 56%. The cost of producing freshwater was estimated at 32.73 cents per cubic meter.

Alirahmi and Assareh [12] analyzed the energy, exergy, and economy and multi-objective optimization of multiple energy systems, including hydrogen production, freshwater, cooling, heating, hot water, and electricity generation of Dezful city. The two objective functions of this study were exergy and total cost, which were optimized by a genetic algorithm. Finally, the best value for the exergy efficiency was 31.66%, and the total unit rate was 21.9 \$/GJ. In 2020, Mohammadi *et al.* [13] designed a combined cycle gas turbine to generate electricity, freshwater, and cooling. The results showed that the use of reverse osmosis is more economical than a combined multi effect distillation and reverse osmosis (MED-RO) system. System costs for electricity, water, and cooling were

also reported at \$ 0.0648 per kilowatt-hour, \$ 0.7219 per cubic meter, and \$ 0.0402 per hour, respectively.

In the aforementioned studies, there is no numerical modeling for wind turbines. It is often assumed that the wind turbine is working under a steady operation condition, and the effect of the changing parameters of the wind turbine on the system was not studied.

In this study, a numerical modeling method is used to model a horizontal axis wind turbine coupled with a direct heat generator and a phase change material (PCM) storage to enhance baseload reliability of the wind system, including an organic Rankine cycle (ORC), a wind turbine, and a PCM storage. The model studied the effects of the different wind turbine's operation conditions on the performance of the described system based on the energy and exergy efficiencies (2E analysis), and finally evaluated the operating conditions for the best overall technical performance of the system.

Materials and Methods

Case Study

The installation of renewable energy sources in the electricity grid creates many problems, because most renewables are intermittent [14]. This article describes a new idea called Wind Thermal Power (WTES), which was first proposed to solve network problems.

Concentrated Solar Power (CSP) is attracting attention due to its susceptibility to scattering. Some plants can operate with continuous power generation 24 hours a day. Thermal energy storage has already become the second-largest energy storage system in the United States after hydrogen. Solana, which has been online since 2013, has a massive 1,680 megawatt-hour power reserve. Total thermal energy storage will almost double in 2015 [3]. Proposals using this practical thermal energy storage are gradually increasing [4-6]. The use of energy storage is also studied from various aspects [7, 8].

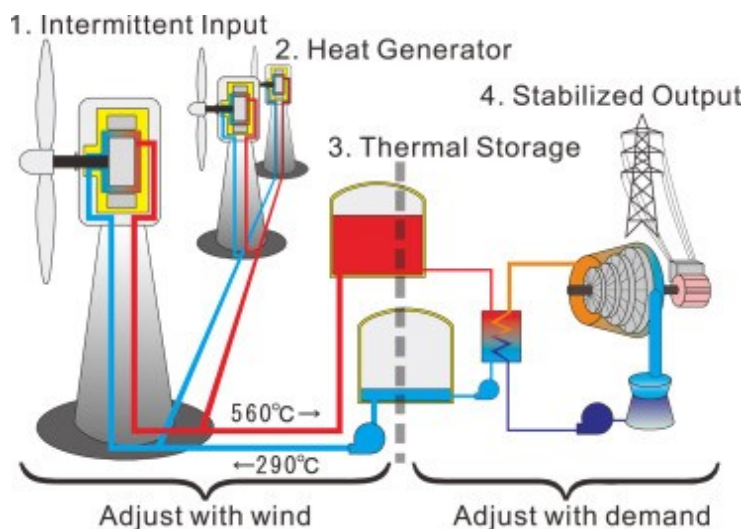


Fig. 1. Schematic of the system

The use of this thermal energy storage and a low-cost and lightweight heat generator are key points of WTES. A typical shape of a “specialized thermal type” WTES is shown in Fig. 1. The rotational energy is converted into thermal energy just above the tower. The rest of the system is of the same type as the CSP turret [9]. The thermal energy generated is transferred to the base facilities by means of a heat transfer fluid (HTF) and produces steam to power the turbine generator when required.

This system is sub-divided into three subsystems and studied in the term of exergy and energy. The mentioned subsystems are wind turbine, storage system, and wind turbine system.

Wind Turbine Energy Analysis

If we consider a wind turbine consisting of three general parts of blades, mechanical equipment, and generator (as shown in Fig. 2), then to analyze the power in each part, energy analysis must be used. The result of using energy analysis is the following Eqs 1 to 4 for turbine power [13].

$$p_w = \frac{1}{2} \rho A v^3 \quad (1)$$

$$p_m = p_w \eta_b \quad (2)$$

$$p_G = p_m \eta_m \quad (3)$$

$$Q_G = p_G \eta_g = \frac{1}{2} \rho A v^3 \eta_m \eta_G \eta_b \quad (4)$$

In the above equations, η_b stands for blade efficiency, η_m is mechanical efficiency of turbine, η_g is generator's efficiency, V is wind speed, A is effective area of wind turbine, ρ is air density, Q_G is turbine output heat, p_G is power received by the generator, p_m is power received by mechanical parts, and p_w is maximum power of the wind [14].

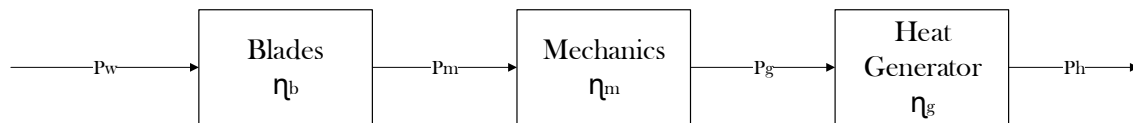


Fig. 2. Schematic of the general parts of a wind turbine

Wind Turbine Exergy Analysis

The exhaust air outlet of the turbine is shown in Eq. (5):

$$EX_{air} = EX_{kinetic} + EX_{potential} + EX_{ph} + EX_{ch} \quad (5)$$

where EX symbolizes the exergy in the above relation, and the substrates of each symbol represent the relevant part (kinetic, potential, physical, and chemical). If we consider the environment as 298 K and air at 1 atm pressure, the chemical and physical exergy of the air will be zero. Because the height of the air does not change, the potential exergy will be zero. So, the air exergy is calculated from $EX_{air} = EX_{kinetic}$, and mass flow and airflow exergy are obtained from the following Eqs 6 and 7 [15]:

$$m = \rho A V_r \quad (6)$$

$$EX_{kinetic} = \frac{V_r^2}{2} \quad (7)$$

where M , R , and V_r are equal to mass flow, rotor radius, and wind speed at high relationships, respectively. If we consider the turbine in the simplified form of Fig. 3, in this figure, the wind turbine consists of blades (which are assumed to be without friction), mechanical equipment (including shaft, bearing, and gearbox with η_m efficiency) and

heat generator with η_G efficiency is considered. As can be seen from the figure, the energies in the flow are in the form of kinetic, work-oriented, and electrical forms that can be fully converted to work, *i.e.*, the current exergy is equal to the content of the flow energy. If for analysis, we consider the system only as a turbine set, then the feed exergy of the system is equal to the state 1 exergy flow and the product exergy flow is equal to the exergy flow of the state 2. The flows are marked with a number on the figure. The exergy of the flows will be in the form of the following Eqs 7 to 12 [16]:

$$EX_1 = m\left(\frac{V_{in}^2}{2}\right) \quad (7)$$

$$EX_2 = m\left(\frac{V_{out}^2}{2}\right) \quad (8)$$

$$EX_3 = EX_1 - EX_2 \quad (9)$$

$$EX_4 = \eta_m EX_3 \quad (10)$$

$$EX_5 = \text{constant in let water} \sim 0 \quad (11)$$

$$EX_6 = \eta_G EX_5 \left(1 - \frac{T_5}{T_6}\right) \quad (12)$$

In the above equations, EX represents the flow of exergy (multiplied by mass flow), and V_{in} and V_{out} are equal to the velocity of the inlet and outlet winds, respectively.

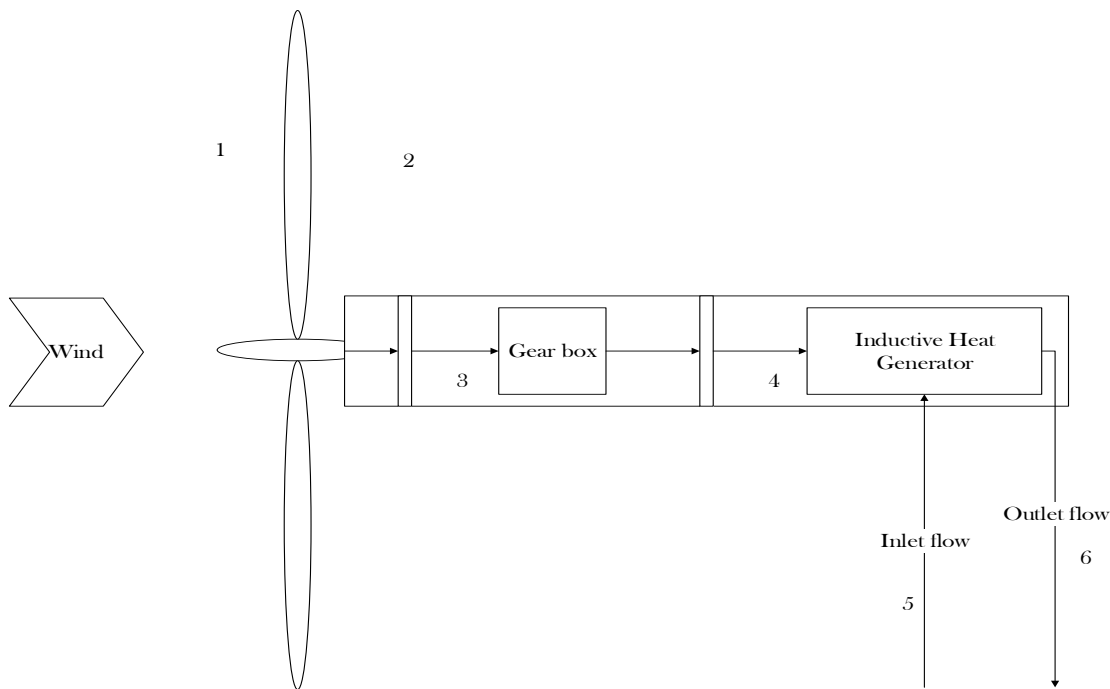


Fig. 3. Schematic of a wind turbine with a display of exergy flows in the turbine assembly

In a wind turbine, the part of the input wind power that is out of the turbine's reach is called the exergy loss and will be equal to the flow exergy of state 1. Also, the part of the exergy, which is lost in the equipment and different parts of the conversion turbine due to friction and inefficiencies of that component and turns into other forms of energy (such as heat), is called exergy destruction which is equal to the difference in exergy level between inlet and output flow (as defined by Eq. (13) [17]):

$$EX_D = EX_{in} - EX_{out} \quad (13)$$

In the above relation, EX_{in} , EX_{out} , and EX_D are equal to the output current exergy, the input current exergy, and the exergy degradation, respectively. Therefore, the

degradation of the exergies of different parts in a turbine can be calculated from Eqs 14 to 16:

$$EX_D = EX_3 - EX_4 = EX_3 - \eta_m EX_3 = EX_3(1 - \eta_m) \quad (14)$$

$$EX_{DG} = EX_4 - EX_6 = \eta_m EX_3 - \eta_G EX_4 = \eta_m EX_3 - \eta_G \eta_m \left(1 - \frac{T_5}{T_6}\right) EX_3 \quad (15)$$

$$EX_{DG} = EX_3 \eta_m \left(1 - \eta_G \left(1 - \frac{T_5}{T_6}\right)\right) \quad (16)$$

where EX_D , EX_{DG} and EX_D are the total exergy damage, the generator exergy degradation, and the exergy degradation of the mechanical part, respectively. For each part, a quantity called the degradation ratio is defined, which is equal to the degradation ratio of that part to the system feed exergy. It is defined in Eqs 17 to 20 [18]:

$$y_{D,t} = \frac{E_{D,t}}{E_f} \quad (17)$$

$$y_{D,G} = \frac{E_{D,G}}{E_f} \quad (18)$$

$$y_{D,m} = \frac{E_{D,m}}{E_f} \quad (19)$$

$$y_{D,tot} = \frac{E_{D,tot}}{E_f} \quad (20)$$

where $y_{D,t}$ is equal to the degradation ratio in the t part and t can be equal to G, m and tot, which represent the generator, the mechanical part and the whole system, respectively. Also, the exergy efficiency of the whole turbine system is defined as the ratio between the output current exergy to the feed flow exergy as calculated in Eq. (21):

$$\text{exergy efficiency}_{sys} = \frac{e_p}{e_f} = \frac{EX_6}{EX_1} = \frac{\eta_G \eta_m \left(1 - \frac{T_5}{T_6}\right)}{EX_1} \quad (21)$$

Replacing the new system requires an analysis of many different aspects. Therefore, in the first step of designing the power generation system, the desired system should be adapted to thermodynamics' rules and principles. Due to the CHP system's combination with two different types of generators as the prime movers, energy analysis must be performed. The purpose of these calculations is to determine the best type of combination with the highest output power, recycled heat, overall efficiency, and the lowest fuel consumption of the system.

Storage Exergy Analysis

Having some practical considerations, a commercial PCM melting point of which is 250 °C (PlusICE H250) is used as a case study. The supplied exergy by HTF during the charging period, the output exergy at discharging cycle, and the exergetic efficiency of PCM storage can be expressed by the following equations, where T_0 , T_6 , T_7 , and T_m refer to temperatures of ambient, HTF inlet, HTF outlet, and PCM melting point, respectively. Storage heat-loss is considered to be negligible [19]:

Charging is calculated in Eq. (22):

$$EX_{pcm,i} = \dot{m}_{HTF} C_{HTF} [(T_6 - T_7) - T_0 \ln(T_6/T_7)] \quad (22)$$

Discharging is calculated in Eq. (23):

$$EX_{pcm.o} = \dot{m}_{HTF} C_{HTF} [(T_7 - T_6) - T_0 \ln(T_7/T_6)] \quad (23)$$

Charge and Discharge are calculated in Eq. (24):

$$T_7 = T_m + (T_7 - T_m)e^{-(h_{pcm}A_{pcm}/\dot{m}_{pcm}C_{pcm})} \quad (24)$$

Exergetic PCM storage efficiency is calculated in Eq. (25):

$$\eta_{pcm} = EX_{pcm.o}/EX_{pcm.i} \quad (25)$$

where $\dot{m}_{HTF} = 6.2$ (kg/s). Also, it is assumed that the isothermal PCM melts, and the sensible heat of the PCM is negligible. Moreover, to minimize any unsatisfactory conditions, it is considered that the controlling system would block the storage tank's path as soon as the difference between T_7 and T_m falls below 30°C. The total exergetic outcome of the system with PCM storage is determined as shown in Eq. (26):

$$\text{Total output exergy} = EX_u + EX_{pcm.o} \quad (26)$$

Finally, the overall exergetic efficiency of the whole system is measured by dividing the sum of all output exergy by the amount of input exergy of the solar system.

Results showed that using "PlusICE H250" as the latent heat storage (LHS) for the Shiraz power plant is suitable due to both PCM physical properties and power plant working conditions, such as HTF temperature (see Table 1)[20].

Table 1. Selected LHS with PlusICE H250 exergetic analysis results

Parameter	unit	value
Exergetic efficiency	(%)	85.54
Exergy Loss	(W)	30200
$EX_{pcm.o}$	(W)	103448
$EX_{pcm.i}$	(W)	133567
Density	(kg/m ³)	2380
Latent heat	(kJ/kg)	280
Specific heat	(kJ/kg K)	1.525
Max working temperature	(°C)	600
Melting point	(°C)	250
Material		PlusICE H250

Rankin cycle

The heat given to the ORC heat exchanger can be calculated by balancing the energy between the operating fluid and the wind tower fluid at the heat exchanger inlet and outlet obtained from Eq. (27) (see Fig. 4).

$$\dot{Q}_6 = \dot{m}_{turbine}(h_7 - h_5) = \dot{m}_{ORC}(h_8 - h_{11}) \quad (27)$$

where $\dot{m}_{turbine}$ is the mass flow rate of geothermal water, and \dot{m}_{ORC} is the mass flow rate of the ORC cycle. By applying the energy balance, the production capacity of the turbine is obtained from Eq. (28).

$$\dot{W}_t = \dot{W}_{t,isen} \eta_t = \eta_t \dot{m}_{ORC} ((h_8 - h_9)) \quad (28)$$

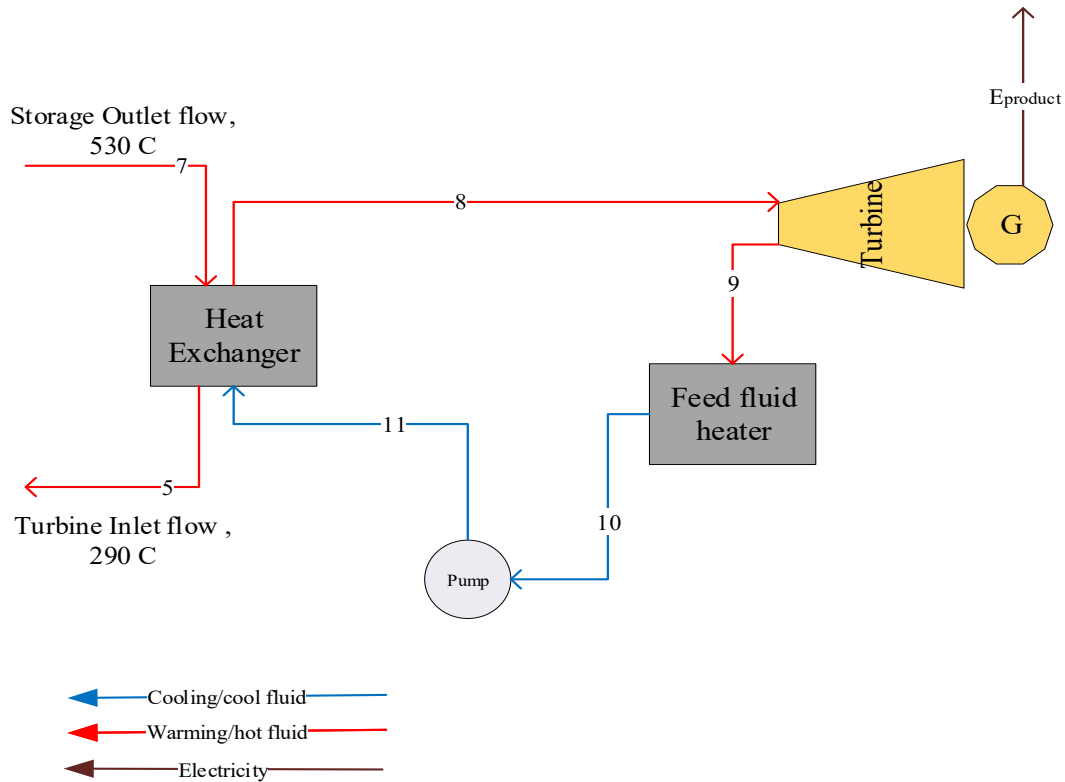


Fig. 4. Schematic of a Rankine system used in the wind turbine system

The heat given to the cooling water in the condenser is calculated from Eq. (29).

$$\dot{Q}_C = \dot{m}_{ORC} (h_{10} - h_9) \quad (29)$$

The consumption of pumps in the cycle is calculated from Eq. (30).

$$\dot{W}_P = \dot{W}_{P1} = \frac{\dot{m}_{ORC}}{\eta_P} (h_{11} - h_{10}) \quad (30)$$

The net generated power of the ORC cycle is obtained from the algebraic sum of the turbine-generated power and the pump consumption, which is injected into the grid directly as $E_{product}$ calculated in Eq. (31).

$$\dot{W}_{net} = \dot{W}_t - \dot{W}_P = \dot{E}_{Product} \quad (31)$$

The energy efficiency of the Rankine cycle is calculated from Eq. (32)[21].

$$\eta_{ORC} = \frac{\dot{W}_{net}}{\dot{Q}_{HX}} \quad (32)$$

Results and Discussion

Validation

In this section, before presenting the results, the values and results obtained are first validated. The purpose of accreditation is to ensure the simulation and its results.

Implementing the 2E method can allow us to make satisfactory predictions about the energy produced under different conditions and calculate the wind speed behind the wind turbines to measure the energy and energy efficiency.

Figure 5 shows the comparison between the real-state power measurement and the power calculated by the 2E code. As shown in Figure 5, the 2E code has a good ability to predict the power output. Increasing the wind speed from 4 m/s to 15 m/s results in a

higher power output at all three tilt angles, whereas after reaching a peak at wind speeds of 11.5 m/s, it has an opposite effect on the power output. On the other hand, increasing the bank angle decreases the power output at all wind speeds. This reduction makes more sense at higher wind speeds. Wind turbines are expected to have the highest performance at a wind speed of 12 m/s and a tilt angle of 5 degrees, producing a power of 140 kW.

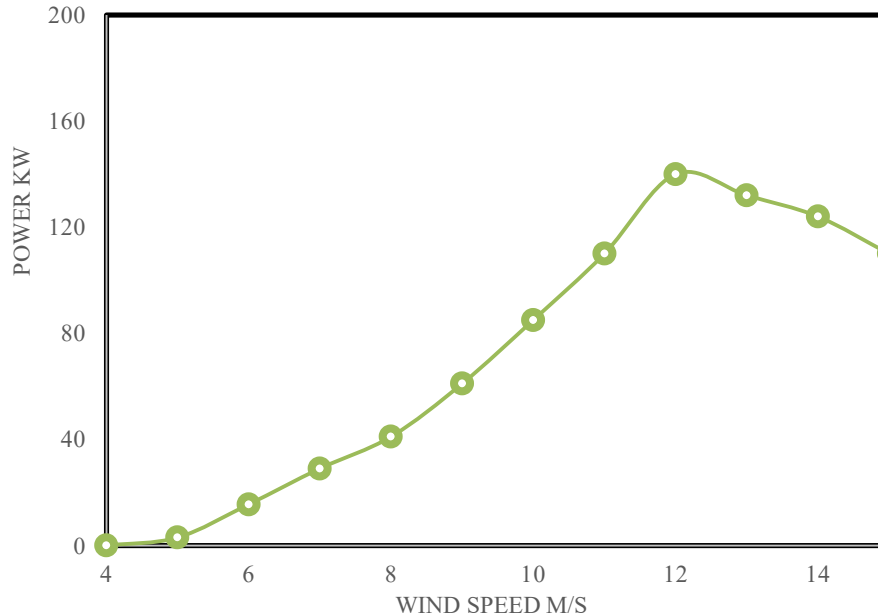


Fig. 5. Comparison of output power between BEM model and experimental data

Wind Turbine's Energy and Exergy Analyses

As seen in Table 2, the wind speed significantly affects the wind turbine's performance based on energy and exergy efficiencies. It causes a steady rise in exergy flow and destruction. The maximum exergy and energy efficiencies are 44.9 % and 46.7 % at wind speed 11.5 m/s, respectively.

Table 2. 2E analysis for wind system in different wind speeds

Wind speed (m/s)	Energy efficiency (%)	Exergy efficiency (%)	Exergy flow (W)	Exergy destruction (W)
6	15.1	13.8	55833.8	12037.2
7	34.7	31.5	86571.5	18203.9
8	43.8	41.6	127209.6	24587.9
9	44.8	43.1	179150	33692.4
10	46.8	45.2	243812.1	44596.7
11	45.7	44.4	322612.5	56701.1
12	46.7	44.9	416960.3	71283.5
13	32.8	32.1	528321.2	74462.9
14	25	24.6	658063.4	75354.3
15	18.3	18	807607.5	71847.3

Table 3 shows that increasing the pressure change can decrease the wind turbine exergy efficiency while increasing the temperature can increase the exergy efficiency from 42.1% at 5°C to 43% at 35°C. However, these changes are not noticeable from the velocity's affect on the wind turbine's exergy efficiency.

Table 3. The effect of pressure changes and temperature on the exergy efficiency of wind turbine

Variables	Exergy efficiency (%)
P= 100 Kpa	44.9
P= 150 Kpa	44.7
P= 200 Kpa	44.6
P= 250 Kpa	44.2
T= 5°C	44.5
T= 20°C	44.7
T= 25°C	44.9
T=35°C	45.2

Results of the System

By comparing the references and the present work presented in Table 4, it can be seen that there is a good accuracy for the results of the calculated parameters in the present work.

Table 4. Performance parameters of organic Rankine cycle with feed fluid recovery and heating

Parameter	value
Fluid agent	R236fa
Heat Exchanger load (kW)	112
Condenser load (kW)	34.9
Turbine output power (kW)	77.0
Pump power consumption (kW)	2.9
Net power output (kW)	69.9
Energy efficiency (%)	62.4
Mass flow rate of operating fluid (kg/s)	1.1

Table 5 shows the performance characteristics of the system. All these values are calculated for four different operating fluids. It is observed that the operating fluid R245fa has the highest energy and exergy efficiency with 49.8% and 27.8%, respectively. Operating fluids R114, R600 and R236fa are also in the next categories in terms of performance characteristics. Table 5 shows the lost exergy rate of system components for all operating fluids. Examining the system's exergy based on the above tables shows that the exchanger and the inductive generator have the highest exergy destruction (heat degradation), because both fluids' exergy flow rate and temperature differences are very high. It is also observed that with the change of operating fluid, the exergy loss in the exchanger decreases. This trend is to increase the power by reducing the loss of exergy in the exchanger. Comparing the operating fluids exergically, it is observed that the operating fluid R245fa has the lowest exergy loss and the operating fluid R236fa has the highest exergy loss in the exchanger. Therefore, it can be concluded that the operating fluid that has less exergy loss in the exchanger produces more power and produces higher exergy loss in the wind turbine (see Table 6).

Table 5. System performance characteristics

Performance characteristic	R236fa	R600	R114	R245fa
Direct power to grid (kW)	69.9	69.9	69.9	69.9
exchanger heat (kW)	112	112	112	112
Condensing heat (kW)	36.99	36.52	34.93	35.56
Turbine power (kW)	75.01	75.48	77.07	76.44
Pump power (kW)	5.11	5.58	7.17	6.54
Total thermal efficiency (%)	67.0	67.4	68.8	68.3
Rankine cycle exergy efficiency (%)	63.7	64	65.4	64.9
Exergy efficiency with wind system (%)	28.7	28.8	29.4	29.2

Table 6. Loss of exergy rate of different system components

System components	R236fa	R600	R114	R245fa
Pump	5.21	5.66	7.33	6.54
Storage	12.76	13.21	13.44	13.51
Turbine	5.24	6.64	5.97	6.71
Condenser	116.2	114.1	109.6	109.2
Generator	45.3	46.1	46.4	47.1

CONCLUSIONS

Thermal backup systems and plants or some energy storage systems are essential, when a considerable amount of wind power is injected into the grid. The findings of other studies showed energy costs of the wind with backup thermal, the wind with battery energy storage, and Wind Powered Thermal Energy System (WTES), which employs inductive heat generators and thermal energy storage systems, are comparable. Also, the results of this study show that the energy and exergy performance of the WTES system is also comparable with conventional wind and other energy storage systems. The results of the 2E analysis show that the exergy efficiency of the system is 28.9%, which is more than solar thermal system exergy efficiency. WTES becomes much more attractive when constructed besides CSP and/or bio-mass plants since many elements can be shared. The configuration of WTES has many variations. Employment of the electric and heat generator enables flexible operation. It can even absorb surplus energy from the grid. Employment of the superconducting heat generator realizes high working temperature, *i.e.*, high thermal to electric conversion efficiency. Those variations, including simple thermal specialized types, have lots of room to be investigated.

Data Availability Statement

The data that support the findings of this study are available from the corresponding author upon reasonable request.

Nomenclature			
Turbine	Turbine fluid	h	Specific enthalpy (kJ/kgK)
C	condenser	EX	Exergy flow, (kW or W)
m	Mechanical	m	Mass flow rate (kg/s or kg/h)
cold	Cold stream	N	Molar flow (mol/s)
HX	Exchanger	R	Universal gas constant (kJ/kgK)
in	inlet	T _m	melting point temperature, °C
out	outlet	T _o	environment temperature, °C
G	Heat generator	T _i	inner temperature, °C
p	pump	EX _{pcm.i}	exergy supplied to the PCM during charging, kW
ref	Working fluid		
t	turbine	EX _{pcm.o}	exergy output from the PCM during discharging, kW
P	Pressure (kPa)		
q	Specific heat(kJ/kg)		
Q	Heat rate (kW)		
s	Specific entropy (kJ/kgK)		
T ₀	Ambient temperature (K)		
η	Efficiency (%)		
E _{product}	Power to the grid (kW)		
mean	average		

REFERENCES

- [1] Gupta, D. K., Kumar, R., and Kumar, N. (2020). Performance analysis of PTC field based ejector organic Rankine cycle integrated with a triple pressure level vapor absorption system (EORTPAS). *Engineering Science and Technology, an International Journal*, 23(1), 82-91. DOI: <https://doi.org/10.1016/j.jestch.2019.04.008>
- [2] Kerme, E. D., Orfi, J., Fung, A. S., Salilih, E. M., Khan, S. U.-D., Alshehri, H., Ali, E., and Alrasheed, M. (2020). Energetic and exergetic performance analysis of a solar driven power, desalination and cooling poly-generation system. *Energy*, 196, 117150. DOI: <https://doi.org/10.1016/j.energy.2020.117150>
- [3] Alirahmi, S. M., Rahmani Dabbagh, S., Ahmadi, P., and Wongwises, S. (2020). Multi-objective design optimization of a multi-generation energy system based on geothermal and solar energy. *Energy Conversion and Management*, 205, 112426. DOI: <https://doi.org/10.1016/j.enconman.2019.112426>
- [4] Alotaibi, S., Alotaibi, F., and Ibrahim, O. M. (2020). Solar-assisted steam power plant retrofitted with regenerative system using Parabolic Trough Solar Collectors. *Energy Reports*, 6, 124-133. DOI: <https://doi.org/10.1016/j.egy.2019.12.019>
- [5] Ehyaei, M. A., Ahmadi, A., El Haj Assad, M., and Salameh, T. (2019). Optimization of parabolic through collector (PTC) with multi objective swarm optimization (MOPSO) and energy, exergy and economic analyses. *Journal of Cleaner Production*, 234, 285-296. DOI: <https://doi.org/10.1016/j.jclepro.2019.06.210>
- [6] Toghyani, S., Afshari, E., Baniasadi, E., and Shadloo, M. S. (2019). Energy and exergy analyses of a nanofluid based solar cooling and hydrogen production combined system. *Renewable Energy*, 141, 1013-1025. DOI: <https://doi.org/10.1016/j.renene.2019.04.073>

- [7] AlZahrani, A. A., and Dincer, I. (2018). Energy and exergy analyses of a parabolic trough solar power plant using carbon dioxide power cycle. *Energy Conversion and Management*, 158, 476-488. DOI: <https://doi.org/10.1016/j.enconman.2017.12.071>
- [8] Yilmaz, F. (2019). Energy, exergy and economic analyses of a novel hybrid ocean thermal energy conversion system for clean power production. *Energy Conversion and Management*, 196, 557-566. DOI: <https://doi.org/10.1016/j.enconman.2019.06.028>
- [9] Ishaq, H., and Dincer, I. (2020). Evaluation of a wind energy based system for co-generation of hydrogen and methanol production. *International Journal of Hydrogen Energy*, 45(32), 15869-15877. DOI: <https://doi.org/10.1016/j.ijhydene.2020.01.037>
- [10] Bamisile, O., Huang, Q., Li, J., Dagbasi, M., Desire Kemena, A., Abid, M., and Hu, W. (2020). Modelling and performance analysis of an innovative CPVT, wind and biogas integrated comprehensive energy system: An energy and exergy approach. *Energy Conversion and Management*, 209, 112611. DOI: <https://doi.org/10.1016/j.enconman.2020.112611>
- [11] Kianfard, H., Khalilarya, S., and Jafarmadar, S. (2018). Exergy and exergoeconomic evaluation of hydrogen and distilled water production via combination of PEM electrolyzer, RO desalination unit and geothermal driven dual fluid ORC. *Energy Conversion and Management*, 177, 339-349. DOI: <https://doi.org/10.1016/j.enconman.2018.09.057>
- [12] Alirahmi, S. M., and Assareh, E. (2020). Energy, exergy, and exergoeconomics (3E) analysis and multi-objective optimization of a multi-generation energy system for day and night time power generation - Case study: Dezful city. *International Journal of Hydrogen Energy*, 45(56), 31555-31573. DOI: <https://doi.org/10.1016/j.ijhydene.2020.08.160>
- [13] Mohammadi, K., Khaledi, M. S. E., Saghafifar, M., and Powell, K. (2020). Hybrid systems based on gas turbine combined cycle for trigeneration of power, cooling, and freshwater: A comparative techno-economic assessment. *Sustainable Energy Technologies and Assessments*, 37, 100632. DOI: <https://doi.org/10.1016/j.seta.2020.100632>
- [14] Okazaki, T., Shirai, Y., and Nakamura, T. (2015). Concept study of wind power utilizing direct thermal energy conversion and thermal energy storage. *Renewable Energy*, 83, 332-338. DOI: <https://doi.org/10.1016/j.renene.2015.04.027>
- [15] Razmi, A. R., and Janbaz, M. (2020). Exergoeconomic assessment with reliability consideration of a green cogeneration system based on compressed air energy storage (CAES). *Energy Conversion and Management*, 204, 112320. DOI: <https://doi.org/10.1016/j.enconman.2019.112320>
- [16] Rashidi, H., and Khorshidi, J. (2018). Exergoeconomic analysis and optimization of a solar based multigeneration system using multiobjective differential evolution algorithm. *Journal of Cleaner Production*, 170, 978-990. DOI: <https://doi.org/10.1016/j.jclepro.2017.09.201>
- [17] Nemati, A., Sadeghi, M., and Yari, M. (2017). Exergoeconomic analysis and multi-objective optimization of a marine engine waste heat driven RO desalination system integrated with an organic Rankine cycle using zeotropic working fluid. *Desalination*, 422, 113-123. DOI: <https://doi.org/10.1016/j.desal.2017.08.012>

- [18] Naseri, A., Bidi, M., Ahmadi, M. H., and Saidur, R. (2017). Exergy analysis of a hydrogen and water production process by a solar-driven transcritical CO₂ power cycle with Stirling engine. *Journal of Cleaner Production*, 158, 165-181. DOI: <https://doi.org/10.1016/j.jclepro.2017.05.005>
- [19] Norouzi, N. (2021). The Pahlev Reliability Index: A measurement for the resilience of power generation technologies versus climate change. *Nuclear Engineering and Technology*, 53(5), 1658-1663. DOI: <https://doi.org/10.1016/j.net.2020.10.013>
- [20] Khajehpour, H., Norouzi, N., Bashash Jafarabadi, Z., Valizadeh, G., & Hemmati, M. H. (2021). Energy, exergy, and exergoeconomic (3E) analysis of gas liquefaction and gas associated liquids recovery co-process based on the mixed fluid cascade refrigeration systems. *Iranian Journal of Chemistry and Chemical Engineering (IJCCE)*. 'Article in Press' DOI: 10.30492/ijcce.2021.141462.4442
- [21] Habibollahzade, A., Gholamian, E., Ahmadi, P., and Behzadi, A. (2018). Multi-criteria optimization of an integrated energy system with thermoelectric generator, parabolic trough solar collector and electrolysis for hydrogen production. *International Journal of Hydrogen Energy*, 43(31), 14140-14157. DOI: <https://doi.org/10.1016/j.ijhydene.2018.05.143>

Article copyright: © 2021 Nima Norouzi. This is an open access article distributed under the terms of the [Creative Commons Attribution 4.0 International License](https://creativecommons.org/licenses/by/4.0/), which permits unrestricted use and distribution provided the original author and source are credited.



Information Technology, Artificial Intelligence and Machine Learning in Smart Grid – Performance Comparison between Topology Identification Methodology and Neural Network Identification Methodology for the Branch Number Approximation of Overhead Low-Voltage Broadband over Power Lines Network Topologies

Athanasios G. Lazaropoulos^{1,2,*}

1: School of Electrical and Computer Engineering / National Technical University of Athens / 9 Iroon Polytechniou Street / Zografou, GR 15780

2: Department of Industrial Design and Production Engineering / School of Engineering / University of West Attica / 250 Thivon & P. Ralli / Athens, GR 12244

Received September 16, 2021; Accepted October 7, 2021; Published October 13, 2021

Broadband over Power Lines (BPL) networks that are deployed across the smart grid can benefit from the usage of machine learning, as smarter grid diagnostics are collected and analyzed. In this paper, the neural network identification methodology of Overhead Low-Voltage (OV LV) BPL networks that aims at identifying the number of branches for a given OV LV BPL topology channel attenuation behavior is proposed, which is simply denoted as NNIM-BNI. In order to identify the branch number of an OV LV BPL topology through its channel attenuation behavior, NNIM-BNI exploits the Deterministic Hybrid Model (DHM), which has been extensively tested in OV LV BPL networks for their channel attenuation determination, and the OV LV BPL topology database of Topology Identification Methodology (TIM). The results of NNIM-BNI towards the branch number identification of OV LV BPL topologies are compared against the ones of a newly proposed TIM-based methodology, denoted as TIM-BNI.

Keywords: Smart Grid; Broadband over Power Lines (BPL) networks; Power Line Communications (PLC); Distribution and Transmission Power Grids; Neural Networks; Machine Learning; IT; Modeling; Artificial Intelligence

1. Introduction

The evolution of the today's traditional power grid hastens the coexistence of this grid with an intelligent IP-based communications network enhanced with a plethora of broadband applications, which is widely referred to as the smart grid [1-5]. Broadband over Power Lines (BPL) technology lies among the available communications alternatives that may support the required information flow of smart grid. The two strongest points of BPL networks compared to the other communications

*Corresponding author: AGLazaropoulos@gmail.com

solutions, such as Radio Frequency (RF) mesh, modified Long Term Evolution (LTE), Code Division Multiple Access (CDMA) at sub GHz bands, dedicated fiber along transmission / distribution lines and 5G communications, are: (i) their easiness to support a communications channel upon the already installed wired power grid infrastructure, and (ii) their interoperability with the aforementioned communications solutions by exploiting the BPL wireline / wireless interfaces [6-10].

Since BPL networks are deployed upon the wired power grid infrastructure that is not a transmission medium designed for communications signals, BPL signals are subjected to various inherent deficiencies, such as high and frequency-selective channel attenuation and noise [11-19]. As the modeling of signal transmission and propagation across BPL channels is concerned, a variety of BPL channel models has been proposed in the literature. BPL channels may follow either a deterministic approach or a statistical approach or a bottom-up approach or a top-down approach or appropriate syntheses of the aforementioned approaches [5], [11-14], [20-36]. Among the available state-of-art BPL channel models of the literature, the deterministic hybrid model (DHM) has extensively been employed to describe the channel behavior of various multiconductor transmission line (MTL) configurations in transmission and distribution BPL network topologies and is also adopted in this paper [11-14], [20], [23], [25, 26], [30]. The outputs of DHM, such as channel attenuation and capacity, are crucial broadband performance metrics of the BPL topologies that further act as the big data feed for the supported broadband applications of smart grid, like Fault and Instability Identification Methodology (FIIM) [3], [37], Main Line Fault Localization Methodology (MLFLM) [4], Topology Identification Methodology (TIM) [3], [38], etc. As TIM is applied in this paper, TIM is considered to be among the most useful piecewise monotonic data approximation (PMA) broadband applications and approximates the exact topological characteristics (*i.e.*, number of branches, length of branches, length of main lines and branch terminations) of an examined BPL topology by exploiting channel attenuation measurements of the examined BPL topology and TIM BPL topology database. In fact, the OV LV BPL topology database of TIM that is used in this paper assigns topological characteristics to respective channel attenuation measurements for a myriad of OV LV BPL topologies. Although there is the great number of OV LV BPL topologies in the TIM OV LV BPL topology database, a TIM-based methodology is proposed here, which exploits channel attenuation measurements and is denoted as TIM-BNI. The purpose is to approximate the number of branches when the OV LV BPL topology with known channel attenuation measurements is not among the OV LV BPL topologies of the TIM OV LV BPL topology database.

As already been mentioned, the leading philosophy behind the BPL channel characterization literature concentrates on following either a deterministic approach or a statistical approach or a bottom-up approach or a top-down approach or appropriate syntheses of the aforementioned approaches, but artificial intelligence (AI) and machine learning (ML) aspire to derive the input-output relations of the BPL channels by learning and capturing information from big data such as those stored in TIM OV LV BPL topology database [39-41]. Among the available AI and ML schemes, neural networks are chosen in this paper due to: (i) their popularity in the communications research field; (ii) their ease of implementation in various architectures; and (iii) their ability to be trained through the backpropagation learning process [42, 43]. By exploiting the available big data of the TIM OV LV BPL topology database and the backpropagation learning process, neural networks are going to be deployed in order to

discover BPL system properties and provide crucial broadband performance metrics for the BPL topologies in the future by deriving relations and revealing hidden states among the BPL system phenomena [40], [44]. Hence, the portfolio of the available supported BPL broadband applications of smart grid is enriched in this paper with the proposed neural network identification methodology for the branch number identification (NNIM-BNI); more specifically, NNIM-BNI of OV LV BPL topologies aims at approximating the number of branches for a given OV LV BPL topology channel attenuation behavior when NNIM-BNI ignores the topological characteristics of the examined OV LV BPL topology. Similarly to the TIM-BNI, NNIM-BNI is going to approximate the number of branches when the OV LV BPL topology, whose channel attenuation measurements are considered, is not among the OV LV BPL topologies of the TIM OV LV BPL topology database. The approximation performances of the two proposed branch number identification methodologies of this paper, *i.e.*, TIM-BNI and NNIM-BNI, are going to be assessed and compared for indicative OV LV BPL topologies that lie outside the TIM OV LV BPL topology database when different operation settings are examined.

The rest of this paper is organized as follows: Section 2 briefly presents the OV LV MTL configurations and the indicative OV LV BPL topologies that are going to be used during the benchmark process of this paper. Also, this Section summarizes the basics of DHM and TIM. Section 3 initially describes TIM-BNI as well as the corresponding performance metrics for its evaluation. Then, a brief description of neural networks is given, while NNIM-BNI with its corresponding performance metrics is also demonstrated. Section 4 presents the performance metrics results for TIM-BNI and NNIM-BNI for the indicative OV LV BPL topologies when different operation settings are assumed. Section 5 concludes this paper.

2. OV LV MTL Configurations, Indicative OV LV BPL Topologies, DHM and TIM and TIM-BNI

In this Section, the basics concerning the propagation and transmission of BPL signals across the OV LV power grid are first given. More specifically, OV LV MTL configurations and the indicative OV LV BPL topologies, which are going to be used for the assessment of TIM-BNI and NNIM-BNI, are presented. Then, the channel model of DHM is briefly analyzed by focusing on its main output of the channel attenuation of OV LV BPL topologies, which is of interest in this paper. Since the topological characteristics and the channel attenuation of OV LV BPL topologies are well defined, TIM and TIM OV LV BPL topology database are demonstrated.

2.1 OV LV MTL Configurations and Indicative OV LV BPL Topologies

In accordance with [45], the typical OV LV MTL configuration that is examined in this paper is illustrated in Fig. 1(a). The examined OV LV MTL configuration consists of four parallel non-insulated conductors (*i.e.*, $n^{OV LV} = 4$), which are spaced each other by a vertical distance $\Delta_{OV LV}$. The upper conductor is the neutral conductor with a radius of $r_{OV LV, n}$, while the lower three conductors are the three LV phases, each with a radius of $r_{OV LV, p}$. The lowest phase conductor is hung at the height $h_{OV LV}$ above the ground, which is considered to be the reference conductor of the OV LV MTL configuration.

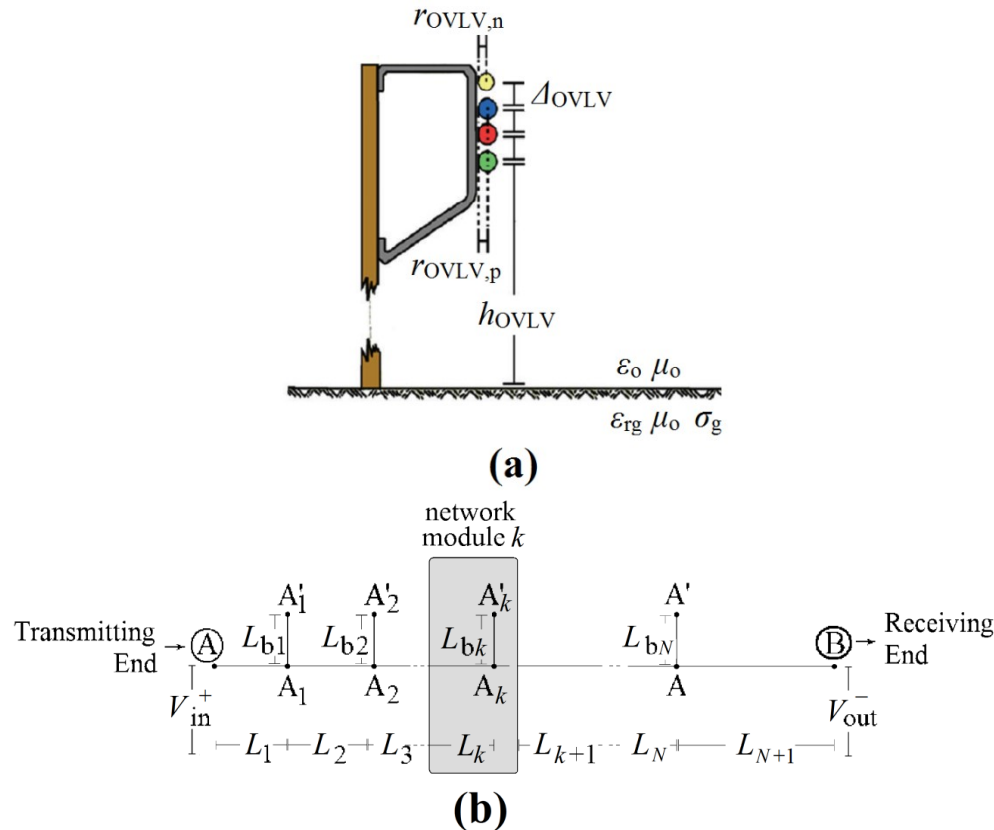


Fig. 1. (a) OV LV MTL configuration [20], [45]. Typical OV LV BPL topology with N branches [36].

The exact dimensions, the material of the conductors, the structure of the conductors and the properties of the imperfect lossy ground are reported in [11], [20], [23], [45-47], while their impact on the BPL signal propagation has been analyzed in [48-50].

To further study the BPL signal transmission across the OV LV BPL network, each network may be divided into cascaded OV LV BPL topologies bounded by the transmitting and receiving ends, while a generic OV LV BPL topology is illustrated in Fig. 1(b). Across the BPL signal transmission path, N branches with their respective terminations, which are assumed to be open-circuit terminations in this paper, may be encountered. The arbitrary k , $k=1, \dots, N$ branch has length equal to L_{bk} and is located at distance $\sum_{i=1}^k L_i$ from the transmitting end. The typical length $\sum_{i=1}^{N+1} L_i$ of 1000 m is assumed between the transmitting and receiving ends.

In accordance with the literature [9], [20], five indicative OV LV BPL topologies (*i.e.*, LOS, rural, suburban, urban A and urban B) are usually used, so that a general study of all OV LV BPL topology classes may be fulfilled. In Table 1, these five indicative OV LV BPL topologies are reported in terms of their topological characteristics and their branch number that is a parameter of interest in this paper. More specifically, the four indicative OV LV BPL topologies shown in green background color in Table 1 (*i.e.*, urban case A, suburban case, rural case and LOS case) are going to be further adopted, so that the approximation performances of the two proposed branch number identification methodologies of this paper, say, NNIM-BNI and TIM-BNI

Table 1
Indicative OV LV BPL Topologies

OV LV BPL Topology Name	Branch Number (N)	Length of Main Lines	Length of Branches
Urban case A (Typical urban case)	3	$L_1=500\text{m}, L_2=200\text{m},$ $L_3=100\text{m}, L_4=200\text{m}$	$L_{b1}=8\text{m}, L_{b2}=13\text{m}, L_{b3}=10\text{m}$
Urban case B (Aggravated urban case)	5	$L_1=200\text{m}, L_2=50\text{m},$ $L_3=100\text{m}, L_4=200\text{m},$ $L_5=300\text{m}, L_6=150\text{m}$	$L_{b1}=12\text{m}, L_{b2}=5\text{m}, L_{b3}=28\text{m},$ $L_{b4}=41\text{m}, L_{b5}=17\text{m}$
Suburban case	2	$L_1=500\text{m}, L_2=400\text{m},$ $L_3=100\text{m}$	$L_{b1}=50\text{m}, L_{b2}=10\text{m}$
Rural case	1	$L_1=600\text{m}, L_2=400\text{m}$	$L_{b1}=300\text{m}$
Line-of-Sight (LOS) case	0	$L_1=1000\text{m}$	-

may be assessed. Note that: (i) the urban case A, suburban case and rural case will be excluded from the TIM OV LV BPL topology database, so that NNIM-BNI and TIM-BNI blindly approximate their branch numbers; (ii) The LOS case is included in the TIM OV LV BPL topology database, because it is unique. Note that there can be no blind approximation by NNIM-BNI and TIM-BNI in the LOS case and for that reason is examined for verification issues; and (iii) The urban case B of 5 branches has been excluded for a further examination due to the high delay that imposes to the TIM OV LV BPL topology database preparation.

2.2 DHM and TIM

DHM can be considered to be a synthetic BPL channel model where a fine module concatenation of a bottom-up, a top-down, a coupling scheme and other performance metric computation modules occurs [9], [11-14], [20], [45]. By the interconnection of the first two DHM modules (*i.e.*, the bottom-up and the top-down module), the propagation and transmission problem of the BPL signal across an OV LV BPL topology for a given OV LV MTL configuration is well defined, thus permitting the computation of the line channel transfer function matrix $\mathbf{H}^{\text{OVLV}}\{\cdot\}$, since more than 2 conductors are encountered in the OV LV MTL configuration of interest. Actually, the $n^{\text{OVLV}} \times n^{\text{OVLV}}$ line channel transfer function matrix $\mathbf{H}^{\text{OVLV}}\{\cdot\}$ that relates line quantities with modal ones is given by

$$\mathbf{H}^{\text{OVLV}}\{\cdot\} = \mathbf{T}_V^{\text{OVLV}} \cdot \mathbf{H}^{\text{OVLV,m}}\{\cdot\} \cdot (\mathbf{T}_V^{\text{OVLV}})^{-1} \quad (1)$$

where $\mathbf{H}^{\text{OVLV,m}}\{\cdot\}$ is the $n^{\text{OVLV}} \times n^{\text{OVLV}}$ modal channel transfer function matrix that mainly depends on the examined OV LV MTL configuration and OV LV BPL topology, and $\mathbf{T}_V^{\text{OVLV}}$ is a $n^{\text{OVLV}} \times n^{\text{OVLV}}$ transformation matrix that depends on the physical properties of the MTLs and the geometry of the OV LV MTL configuration. Since modal channel transfer function and transformation matrices are frequency dependent, this implies that the line channel transfer function is also a frequency dependent parameter. On the basis of the first two DHM modules, the third DHM module arranges the way that the BPL signals are injected into and extracted from the TLs of the MTL configurations; say, the third DHM module mathematically describes the different coupling schemes of the BPL signal injection / extraction [51, 52]. With reference to eq. (1), the coupling

scheme channel transfer function, which is the mathematical expression of the interconnections of the first three DHM modules relating output BPL signals and input ones is given by

$$H^{\text{OVLV},C}\{\cdot\} = [\mathbf{C}^{\text{out}}]^{\text{OVLV},C} \cdot \mathbf{H}^{\text{OVLV}}\{\cdot\} \cdot [\mathbf{C}^{\text{in}}]^{\text{OVLV},C} \quad (2)$$

for given coupling scheme where $[\cdot]^C$ denotes the applied coupling scheme, \mathbf{C}^{in} is the input coupling $n^{\text{OVLV}} \times 1$ column vector dealing with the BPL signal injection process and \mathbf{C}^{out} is the output coupling $1 \times n^{\text{OVLV}}$ line vector dealing with the BPL signal extraction process. More details concerning the available coupling schemes and the respective involved conductors of the examined OV LV MTL configuration are detailed in [51, 52]. Other DHM performance metric computation modules are outside the scope of this paper and are not further analyzed here. It is evident from eq. (2) that the coupling scheme channel transfer function is a frequency dependent parameter and depends on the topological characteristics of the examined OV LV BPL topology. Thus, for given OV LV MTL configuration and coupling scheme, their corresponding coupling scheme channel transfer functions can be computed by DHM by only adjusting the topological characteristics of OV LV BPL topologies.

The aforementioned collection of topological characteristics and corresponding coupling scheme channel transfer functions for a variety of OV LV BPL topologies may act as the big data feed of the supported smart grid broadband applications, such as TIM of this paper [3], [38]. In accordance with [3], TIM can identify an OV LV BPL topology with respect to its topological characteristics (*i.e.*, number of branches, length of branches, length of main distribution lines and branch terminations) when its corresponding coupling scheme transfer function behavior is known. In fact, by appropriately storing and retrieving the previous collection of OV LV BPL topologies to / from the TIM OV LV BPL topology database, TIM can identify an OV LV BPL topology even if significant measurement differences may occur by appropriately exploiting piecewise monotonic data approximations [53, 54]. As the TIM OV LV BPL topology database is concerned in this paper, no measurement differences are assumed. Depending on the examined scenario of accuracy degree, corresponding TIM OV LV BPL topology database specifications can be assumed for the database preparation; say, the maximum number of branches N_{max} , the length spacing L_s for both branch distance and branch length, and the maximum branch length $L_{b,\text{max}}$ for the OV LV BPL topologies that are going to be stored in the database. Finally, for each OV LV BPL topology of the TIM OV LV BPL topology database, the following data are maintained for the further analysis of this paper: (i) its ID number p in the TIM OV LV BPL topology database when P is the number of all OV LV BPL topologies in the TIM OV LV BPL topology database; (ii) the actual number of branches N ; and (iii) the coupling scheme channel transfer function values with respect to the frequency.

3. TIM-BNI and NNIM-BNI

In this Section, the proposal of TIM-BNI and NNIM-BNI is theoretically detailed. Suitable performance metrics, which allow the approximation assessment of the branch numbers of the indicative OV LV BPL topologies in each methodology, are reported. Note that prior to the presentation of NNIM-BNI, an introduction of neural networks in OV LV BPL networks is also given.

3.1 TIM-BNI

With reference to Sec. 2.2, the TIM OV LV BPL topology database may consist of a plethora of OV LV BPL topologies whose number depends on the required accuracy degree or, in other words, the TIM OV LV BPL topology database specifications applied (*i.e.*, the maximum number of branches N_{\max} , the length spacing L_s for both branch distance and branch length and the maximum branch length $L_{b,\max}$, operation frequency range, etc). Since indicative OV LV BPL topologies of Table 1 are not included in the TIM OV LV BPL topology database by definition except LOS case, TIM-BNI is going to approximate the branch number of the examined indicative OV LV BPL topology by comparing its coupling scheme channel transfer function values with respect to the frequency, which are known for the branch number identification problem of this paper, against the respective ones of all the OV LV BPL topologies of the TIM OV LV BPL topology database. To identify the OV LV BPL topologies of the TIM OV LV BPL topology database that better approximate the channel attenuation behavior of the examined indicative OV LV BPL topology, the performance metric of the root-mean-square deviation (RMSD) of the amplitude of coupling scheme channel transfer functions in dB is first going to be computed as follows:

$$RMSD_{\text{TIM-BNI},p} = \sqrt{\frac{\sum_{q=1}^Q \left(\left| H_{\text{TIM},p}^{\text{OVLV,C}}(f_q) \right|_{\text{dB}} - \left| H_{\text{indicative}}^{\text{OVLV,C}}(f_q) \right|_{\text{dB}} \right)^2}{Q}} \quad (3)$$

where

$$f_q = 3\text{MHz} + (q - 1) \cdot f_s, q = 1, \dots, Q \quad (4)$$

is the flat-fading subchannel start frequency, f_s is the flat-fading subchannel frequency spacing, Q is the number of subchannels in the examined frequency range, $H_{\text{indicative}}^{\text{OVLV,C}}(f_q)$ is the coupling scheme channel transfer function of the indicative OV LV BPL topology at frequency f_q and $H_{\text{TIM},p}^{\text{OVLV,C}}(f_q)$ is the coupling scheme channel transfer function of the p -th OV LV BPL topology of the TIM OV LV BPL topology database at frequency f_q . The average value of the branch numbers of the R OV LV BPL topologies of the TIM OV LV BPL topology database that present the R lowest RMSDs among the P computed ones defines the TIM-BNI approximation of the branch number of the examined indicative OV LV BPL topology $N_{\text{TIM-BNI}}$. It is evident that the TIM-BNI performance towards the branch number identification of OV LV BPL topologies, that is numerically assessed in Section 4, is affected by the required accuracy degree of the TIM OV LV BPL topology database and the number R of the lowest RMSDs that are taken into account during the approximation.

3.2 Neural Networks and NNIM-BNI

As an application tool of the ML philosophy, neural networks can acquire knowledge and unveil hidden system properties or patterns from the simple output observations during the system operation. Neural networks have already been adopted in [55] for the channel attenuation determination of BPL networks. As already been mentioned, a main advantage of the neural networks is their ease of implementations in parallel or concurrent architectures [40], while neural networks become more accurate during their approximations as the backpropagation learning process exists [42, 43], [56].

In Fig. 2, the structure of the fully connected neural network with HL hidden layers of neurons that is adopted by NNIM-BNI in this paper is shown. More specifically,

this neural network receives as input the $Q \times 1$ column vector $\Delta \mathbf{H}_{\text{TIM},p,hl=0}^{\text{OVLV},C}\{\cdot\}$ that is given by

$$\Delta \mathbf{H}_{\text{TIM},p,hl=0}^{\text{OVLV},C}\{\cdot\} = [|H_{\text{TIM},p}^{\text{OVLV},C}(f_1)|_{\text{dB}} - |H_{\text{LOS}}^{\text{OVLV},C}(f_1)|_{\text{dB}} \cdots |H_{\text{TIM},p}^{\text{OVLV},C}(f_q)|_{\text{dB}} - |H_{\text{LOS}}^{\text{OVLV},C}(f_q)|_{\text{dB}} \cdots |H_{\text{TIM},p}^{\text{OVLV},C}(f_Q)|_{\text{dB}} - |H_{\text{LOS}}^{\text{OVLV},C}(f_Q)|_{\text{dB}}]^T \quad (5)$$

Note that the column vector $\Delta \mathbf{H}_{\text{TIM},p,hl=0}^{\text{OVLV},C}\{\cdot\}$ concerns the arbitrary p -th OV LV BPL topology of the TIM OV LV BPL topology database at frequencies f_q , $q = 1, \dots, Q$.

In eq. (5), $|H_{\text{LOS}}^{\text{OVLV},C}\{\cdot\}|_{\text{dB}}$ is the amplitude of the coupling scheme channel transfer functions of the LOS case of Table 1 in dB and $[\cdot]^T$ denotes the transpose of the matrix. After the input layer, the hidden layers occur. For the arbitrary hl hidden layer, its output $Q \times 1$ column vector $\Delta \mathbf{H}_{\text{TIM},p,hl}^{\text{OVLV},C}\{\cdot\}$ is given by

$$\Delta \mathbf{H}_{\text{TIM},p,hl}^{\text{OVLV},C}\{\cdot\} = \sigma(\mathbf{w}_{hl} \cdot \Delta \mathbf{H}_{\text{TIM},p,hl-1}^{\text{OVLV},C}\{\cdot\} + \mathbf{b}_{hl}) \quad (6)$$

where $\sigma(\cdot)$ is the activation function, \mathbf{w}_{hl} is the the $Q \times Q$ array of weights of the hl hidden layer and \mathbf{b}_{hl} is the the $Q \times Q$ array of biases of the hl hidden layer. The output of the fully connected neural network that coincides with the output of the HL hidden layer is the NNIM-BNI approximation of the branch number of the examined indicative OV LV BPL topology $N_{\text{NNIM-BNI}}$.

Actually, NNIM-BNI exploits the MATLAB neural network training program of [43], [57] that is based on the architecture of the fully connected neural network demonstrated in Fig. 2. In accordance with [43], [57], NNIM-BNI is going to train neural networks of variable numbers of hidden layers by using the input and output data contained in the TIM OV LV BPL topology database with respect to eqs. (5) and (6). In accordance with [43], [57], NNIM-BNI is going to randomly split the supplied data of the OV LV BPL topologies of the TIM OV LV BPL topology database into three phase, *i.e.*, training, validation and testing. According to [43], [57], the Levenberg-Marquardt algorithm is adopted during the training phase of NNIM-BNI, while the performance metric of RMSD of the amplitude of the differences of coupling scheme channel transfer functions in dB as described in eq. (5) is computed for the OV LV BPL topologies of the TIM OV LV BPL topology database during the testing phase. In general terms, the parameters of the neural networks with smaller RMSDs per hidden layer are those that are selected for the testing where the four indicative OV LV BPL topologies of Table 1 are concerned. Hence, apart from the RMSD of the OV LV BPL topologies of the TIM OV LV BPL topology database selected for the testing phase, the MATLAB neural network training program of [43], [57] can also compute RMSD of the indicative OV LV BPL topologies for different numbers of the hidden layers. Therefore, NNIM-BNI gives the NNIM-BNI approximation value of the branch numbers $N_{\text{NNIM-BNI}}$ of the examined indicative OV LV BPL topologies as well as their approximation RMSDs for the aforementioned topologies per hidden layer as output. It is evident that the NNIM-BNI performance towards the branch number identification of OV LV BPL topologies, which is also numerically assessed in Section 4 in comparison with the TIM-BNI performance, is affected by the required accuracy degree of the TIM OV LV BPL topology database and the participation percentage of the three phases (*i.e.*, training, validation and testing) during the operation of its MATLAB neural network training program.

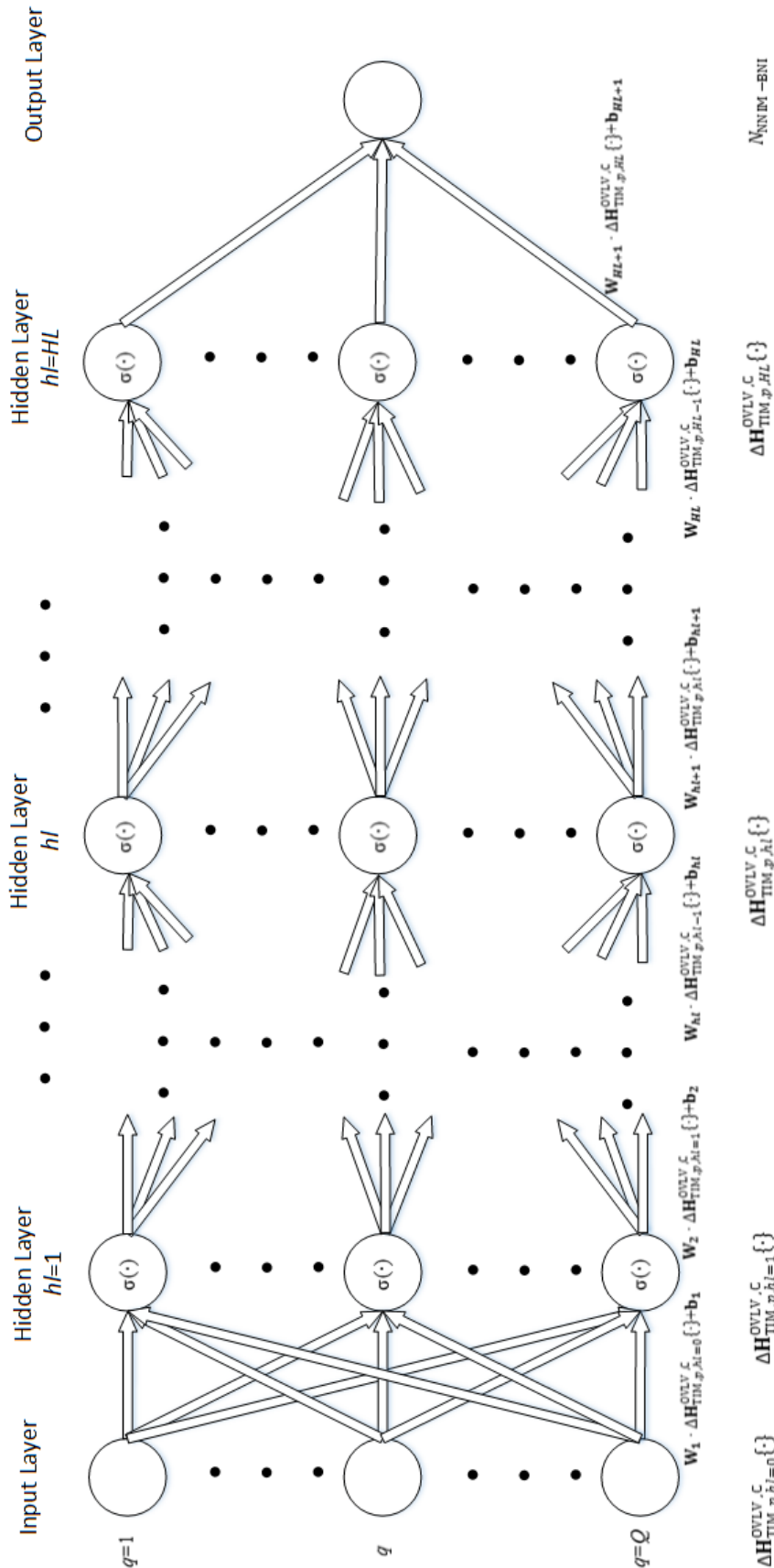


Fig. 2. Architecture of the fully connected neural network with HL hidden layers.

4. Numerical Results and Discussion

In this Section, numerical results concerning the performance of TIM-BNI and NNIM-BNI are presented as well as their comparison. On the basis of the default operation settings of the base scenario given in Sec.4.1, the performance metric of RMSD is applied in order to assess TIM-BNI and NNIM-BNI approximations. In Sec. 4.2, the impact of higher detail (*e.g.*, wider operation frequency range) during the preparation of the OV LV BPL topologies of the TIM OV LV BPL topology database is assessed when TIM-BNI and NNIM-BNI are applied. Also, the issue of the representativeness of the TIM OV LV BPL topology database is addressed. In Sec. 4.3, the role of the number of OV LV BPL topologies of the TIM OV LV BPL topology database that are considered during the computation of the average value of the branch numbers is investigated during the operation of TIM-BNI. In Sec. 4.4, the role of the participation percentages of the three phases (*i.e.*, training, validation and testing) during the operation of NNIM-BNI is examined.

4.1 Base Scenario and Default Operation Settings

As the base scenario of the cooperation of the TIM OV LV BPL topology database, TIM-BNI and NNIM-BNI are concerned, and the following default operation settings are assumed:

- As the preparation of the TIM OV LV BPL topology database is regarded, the OV LV MTL configuration of Fig. 1(a) and the typical OV LV BPL topology with N branches of Fig. 1(b) are assumed. On the basis of the required parameters of the TIM OV LV BPL topology database [3], [38], during the preparation of the TIM OV LV BPL topology database, its OV LV BPL topologies considered comprises from 0 (say “LOS” case) up to 3 branches in accordance with Sec. 2.1 and Table 1. The length spacings for branch distance and branch length are assumed to be equal to 100 m and 25 m, respectively, while the branch line length may range from 0 m to 100 m. Note that the distribution line length has already been assumed to be the typical one in Sec. 2.1 thus being equal to 1000 m. The frequency range is assumed equal to 3-30 MHz, while the flat-fading subchannel frequency spacing is equal to 1 MHz. For each OV LV BPL topology of the P ones of the TIM OV LV BPL topology database, its ID number p in the TIM OV LV BPL topology database, its number of branches, and the amplitude of its coupling scheme channel transfer function in dB with respect to the frequency are stored in the TIM OV LV BPL topology database.
- As the operation of the TIM-BNI is concerned, the performance metric of RMSD of the amplitudes of coupling scheme channel transfer functions in dB of the OV LV BPL topologies of the TIM OV LV BPL topology database with respect to the ones of each of the indicative OV LV BPL topologies of Table 1 is applied as described in eq. (3). For the base scenario where default operation settings are assumed, the average value of the branch numbers of the $R=5$ OV LV BPL topologies of the TIM OV LV BPL topology database that presents the 5 lowest RMSDs among the P computed ones defines the TIM-BNI approximation of the branch number $N_{\text{TIM-BNI}}$ of each of the examined indicative OV LV BPL topologies of Table 1. For each of the examined indicative OV LV BPL topologies of Table 1, the TIM-BNI performance assessment is going to be fulfilled through the comparison between the TIM-BNI approximated branch

number value $N_{\text{TIM-BNI}}$ and the actual one while the performance metric of RMSD again assess the overall TIM-BNI approximation for the four examined indicative OV LV BPL topologies of Table 1.

- As the operation of the NNIM-BNI is concerned, NNIM-BNI is based on the MATLAB neural network training program of [43], [57]. In accordance with [43], [57], the division of the available OV LV BPL topologies of the TIM OV LV BPL topology database is random, while the default participation percentage of the three phases of the MATLAB neural network training program of [43] and [57] (*i.e.*, training, validation and testing) during the operation of NNIM-BNI are assumed to be equal to 70%, 15% and 15%, respectively. Given the amplitudes of coupling scheme channel transfer functions in dB for each of the four examined indicative OV LV BPL topologies of Table 1, NNIM-BNI gives the respective NNIM-BNI approximation of the branch numbers $N_{\text{NNIM-BNI}}$ per hidden layer as output, where the maximum number of hidden layers HL is assumed to be equal to 5. Since the behavior and performance of the machine learning algorithms and the neural network approaches are referred to as stochastic, three executions of NNIM-BNI are going to be reported in each examined case given the participation percentage of the three phases. Similarly to TIM-BNI, for each of the examined indicative OV LV BPL topologies of Table 1, the TIM-BNI performance assessment is going to be fulfilled through the comparison between the TIM-BNI approximated branch number value $N_{\text{TIM-BNI}}$ and the actual one while the performance metric of RMSD will again assess the overall NNIM-BNI approximation.

In Table 2, the branch number approximations of TIM-BNI and NNIM-BNI are reported, when the aforementioned default operation settings are assumed. Apart from the branch number approximations, the actual branch numbers of the four examined OV LV BPL topologies of Table 1 are presented for comparison reasons, while the RMSDs of TIM-BNI and NNIM-BNI for the four examined OV LV BPL topologies are also computed. Note that three executions of NNIM-BNI are reported for each of the four examined OV LV BPL topologies.

From Table 2, several interesting initial remarks concerning the performance of TIM-BNI and NNIM-BNI can be pointed out. More specifically:

- With reference to the performance metric of RMSD and given the default operation settings of the base scenario, TIM-BNI seems to better approximate in general the branch number of the four indicative OV LV BPL topologies of Table 1. Indeed, the branch number approximations of TIM-BNI are closer to the actual number of branches in the cases of the urban case A, rural case and LOS case, which are anyway highlighted in green color in Table 2, in comparison with the branch number approximations of NNIM-BNI. In contrast, NNIM-BNI only better approximates the branch number of the suburban case, which is again highlighted with green color in Table 2, when 5 hidden layers are assumed.

Table 2.

Branch Number Approximations of TIM-BNI and NNIM-BNI for the Default Operation Settings

Indicative OV LV BPL Topologies of Table 1		Urban case A (Typical urban case)	Suburban case	Rural case	LOS case	RMSD	Notes
Actual Number of Branches N		3	2	1	0	-	-
TIM-BNI (Approximated Number of Branches) $N_{TIM-BNI}$		3	3	2	0.80	0.81	Default Operation Settings
NNIM-BNI (Approximated Number of Branches) $N_{NNIM-BNI}$	1 st execution	2.94	2.81	2.82	2.82	1.73	Default Operation Settings + 1 hidden layer
	2 nd execution	2.95	2.81	2.83	2.83	1.73	
	3 rd execution	2.94	2.80	2.82	2.82	1.72	
	1 st execution	8.26	1.35	2.72	2.70	3.09	Default Operation Settings + 2 hidden layers
	2 nd execution	5.58	2.79	2.72	2.72	2.10	
	3 rd execution	5.72	2.68	2.70	2.69	2.12	
	1 st execution	2.87	2.86	2.84	2.83	1.74	Default Operation Settings + 3 hidden layers
	2 nd execution	3	2.93	2.85	2.85	1.76	
	3 rd execution	2.81	3.01	2.80	2.80	1.74	
	1 st execution	3.01	-15.36	2.72	2.70	8.82	Default Operation Settings + 4 hidden layers
	2 nd execution	2.96	-97.39	2.29	2.17	49.71	
	3 rd execution	2.90	3	2.90	2.90	1.81	
	1 st execution	354.21	2.15	2.06	2.19	175.61	Default Operation Settings + 5 hidden layers
	2 nd execution	3.07	-159.30	2.69	2.41	80.66	
	3 rd execution	3.04	-526.56	3.24	1.76	264.28	

- Since the TIM-BNI approximation of the branch number $N_{TIM-BNI}$ of each of the examined OV LV BPL topologies is equal to the average value of the branch numbers of the 5 OV LV BPL topologies of the TIM OV LV BPL topology database that present the 5 lowest RMSDs among the P computed ones, the TIM-BNI approximation of the branch number of the LOS case is the mean value of the LOS case, which is unique, and of four OV LV BPL topologies of one branch.

- By assuming up to 5 hidden layers and up to 3 executions per hidden layer, it is clearly shown the stochastic nature of NNIM-BNI, namely:
 - Above the third hidden layer, NNIM-BNI becomes unstable, as high or negative numbers of branches in OV LV BPL topologies are demonstrated. In fact, the differences among the NNIM-BNI branch number approximations of the different executions for given OV LV BPL topology and hidden layer are significant high, when the assumed hidden layers are above three. The previous observation is also verified by the high values of RMSD during the NNIM-BNI approximations, when the assumed hidden layers are above three.
 - When the hidden layers are below or equal to 3, RMSDs of NNIM-BNI remain low (*i.e.*, in the majority of the cases below 2) and comparable to the one of TIM-BNI (*i.e.*, 0.81). In addition, by comparing RMSD values of NNIM-BNI among the different executions, it is shown that these RMSD values remain also low and comparable among them for given number of hidden layers when hidden layers below or equal to 3 are assumed. Note that the NNIM-BNI approximations do not present negative or irrational high branch number values, when below or equal to 3 hidden layers are assumed.
- Due to the default operation settings concerning the preparation of the TIM OV LV BPL topology database, the number of OV LV BPL topologies with 3 branches is significantly higher than the number of OV LV BPL topologies with 2 branches that is again significantly higher than the number of OV LV BPL topologies with 1 branch. Note that the LOS case, which is an OV LV BPL topology with no branches, is unique. The aforementioned distribution has no impact on the performance of TIM-BNI but greatly affects the approximations and the performance of NNIM-BNI (*e.g.*, the approximation values present almost equal values, when 1 hidden layer is assumed). Therefore, the structure of the TIM OV LV BPL topology database mainly affects the NNIM-BNI performance.
- Apart from the structure of the TIM OV LV BPL topology database, the randomness during the three phases of the operation of NNIM-BNI, which comes from the participation percentages, justifies the stochastic nature of NNIM-BNI. In general, the participation percentages of the three phases of the operation of NNIM-BNI imply that different OV LV BPL topologies of the TIM OV LV BPL topology database are considered during the training of the neural networks that further affect the arrays of weights and biases of the hidden layers as denoted in eq. (6). Anyway, the NNIM-BNI approximation differences remain low, when hidden layers below or equal to 3 are assumed as it is shown among the different executions for given hidden layer number.

Apart from the operation settings of TIM-BNI and NNIM-BNI, it is obvious from the previous observations that the accuracy detail and the structure of the TIM OV LV BPL topology database critically affect the performance of both methodologies. In the following subsection, the impact of the accuracy detail and the structure of the TIM OV LV BPL topology database are assessed according to the performance of TIM-BNI and NNIM-BNI.

4.2 The Impact of TIM OV LV BPL Topology Database on TIM-BNI and NNIM-BNI Performance

In this subsection, the impact of TIM OV LV BPL topology database on the performance of TIM-BNI and NNIM-BNI is presented. First, it is evident that a more detailed TIM OV LV BPL topology may have a positive effect on the RMSDs of TIM-BNI and NNIM-BNI. Similarly to Table 2, the branch number approximations of TIM-BNI and NNIM-BNI are reported in Table 3. When the aforementioned default operation settings are assumed, but the frequency span remains equal to 1 MHz, the wider frequency range is 3-88 MHz. Apart from the branch number approximations, the actual branch numbers of the four examined OV LV BPL topologies of Table 1 and the RMSDs of TIM-BNI and NNIM-BNI for the four examined OV LV BPL topologies are presented. Again as in Table 2, three executions of NNIM-BNI are reported for each of the four examined OV LV BPL topologies.

By comparing Tables 2 and 3, the following remarks can be pointed out:

- The wider frequency range of 3-88 MHz for each of the OV LV BPL topologies of the TIM OV LV BPL topology database implies that 86 checks should occur during the operation of TIM-BNI and NNIM-BNI in Table 3 instead of the respective 28 checks of Table 2. Hence, a more rigorous approximation with higher accuracy is expected in Table 3, which is anyway reflected on the better RMSD values of both identification methods; say, the best RMSDs of TIM-BNI and NNIM-BNI are equal to 0.65 and 1.31 in Table 3 in contrast with 0.81 and 1.72 in Table 2, respectively. TIM-BNI again better approximates the branch numbers of the indicative OV LV BPL topologies in Table 3. Note that the best branch number approximation per examined OV LV BPL topology is highlighted in green color in Table 3 as well the best RMSD.
- As the branch number approximations of the four indicative OV LV BPL topologies are discussed, the higher accuracy of the TIM OV LV BPL topology database of Table 3 helps as follows:
 - NNIM-BNI accurately approximates the branch number of the urban case A. Now, TIM-BNI and NNIM-BNI can accurately identify the 3 branches of the urban case A.
 - The approximation performance of both identification methodologies remains almost the same, when the suburban case is examined.
 - Significant improvement of the approximation performance is achieved by TIM-BNI, when the rural case is investigated (*i.e.*, from 2 to 0.80 branches when the actual branch number of rural case is equal to 1). Here, it should be noted that the result of TIM-BNI is a deterministic approximation. Conversely, the accuracy performance of NNIM-BNI as reported in Table 3 remains almost the same with the one of Table 2 in the rural case.
 - As the LOS case is examined, the approximation performance of both identification methodologies remains almost the same.
- When below or equal to 3 hidden layers are examined, RMSD values of NNIM-BNI steadily remain low and comparable to the one of TIM-BNI. Anyway, for the following analysis, only one execution is going to be applied during the performance assessment of NNIM-BNI.

Table 3.
Branch Number Approximations of TIM-BNI and NNIM-BNI for the Default Operation Settings but for the Frequency Range of 3-88MHz

Indicative OV LV BPL Topologies of Table 1		Urban case A (Typical urban case)	Suburban case	Rural case	LOS case	RMSD	Notes
Actual Number of Branches N		3	2	1	0	-	-
TIM-BNI (Approximated Number of Branches) $N_{TIM-BNI}$		3	3	0.80	0.80	0.65	Default Operation Settings (Frequency Range 3-88MHz)
NNIM-BNI (Approximated Number of Branches) $N_{NNIM-BNI}$	1 st execution	3	2.46	2.46	2.46	1.45	Default Operation Settings (Frequency Range 3-88MHz) + 1 hidden layer
	2 nd execution	3	2.27	2.27	2.27	1.31	
	3 rd execution	2.47	2.47	2.47	2.47	1.48	
	1 st execution	-1894.52	-1894.01	2.70	2.38	1341.22	Default Operation Settings (Frequency Range 3-88MHz) + 2 hidden layers
	2 nd execution	-338.59	-1041.68	3.47	2.47	549.08	
	3 rd execution	3.28	2.89	2.73	2.72	1.68	
	1 st execution	3.35	2.72	2.70	2.69	1.64	Default Operation Settings (Frequency Range 3-88MHz) + 3 hidden layers
	2 nd execution	-4.47	45.72	2.73	2.71	22.23	
	3 rd execution	3.13	4.20	2.65	2.48	1.86	
	1 st execution	-23.31	38.16	2.61	2.52	22.41	Default Operation Settings (Frequency Range 3-88MHz) + 4 hidden layers
	2 nd execution	2.99	48.46	2.90	2.10	23.27	
	3 rd execution	4.46	0.71	3.46	1.90	1.83	
	1 st execution	-0.21	51.89	2.76	2.25	25.04	Default Operation Settings
	2 nd execution	6.44	3.47	2.59	2.52	2.39	

	execution						(Frequency
	3 rd execution	2.47	25.95	2.62	2.37	12.06	Range 3- 88MHz) + 5 hidden layers

Similarly to Table 2, RMSDs of NNIM-BNI approximations remain greater than the RMSD of TIM-BNI regardless of the number of the hidden layers and the number of executions considered. In fact, the approximated numbers of branches of suburban case, rural case and LOS case remain almost the same during the most successful NNIM-BNI approximations. This is because of the preparation of TIM OV LV BPL topology database. Due to the operation settings of TIM OV LV BPL topology database, 0.0035%, 0.19%, 4.75% and 95.05% of the OV LV BPL topologies of the TIM OV LV BPL topology database of Table 3 are OV LV BPL topologies of 0, 1, 2 and 3 branches, respectively. The aforementioned participation percentage of OV LV BPL topologies in TIM OV LV BPL topology affects the approximation performance of stochastic approximations of NNIM-BNI, thus explaining the almost equal approximated numbers of branches of the suburban case, rural case and LOS case.

Although the performance of both identification methodologies significantly depends on the accuracy degree of the TIM OV LV BPL topology database as shown in Table 3, the RMSD values can get improved even more especially in the cases of the stochastic NNIM-BNI approximations, when representative sets of the TIM OV LV BPL topology database are applied. A good representative set should capture the most information from the original TIM OV LV BPL topology database [58]. Algorithms (such as Maximum Coverage, k-medoid clustering, etc [59, 60]) can generate balanced subsets that capture original information from the initial TIM OV LV BPL topology database. Here, three representative sets of the TIM OV LV BPL topology database of Table 3 are applied, where the number of OV LV BPL topologies of 1, 2 and 3 branches remains the same in the representative sets. The selection of OV LV BPL topologies with 2 and 3 branches is random among the available ones from the TIM OV LV BPL topology database of Table 3. In Table 4, the branch number approximations of TIM-BNI and NNIM-BNI are reported, when the aforementioned default operation settings of Sec.4.1 are assumed but for three representative sets of the TIM OV LV BPL topology database of Table 3. Apart from the branch number approximations, the actual branch numbers of the four examined OV LV BPL topologies of Table 1 are again presented. Also, RMSDs of TIM-BNI and NNIM-BNI for the four examined OV LV BPL topologies are demonstrated. Note that the three representative sets consist of random OV LV BPL topologies of 2 and 3 branches from the initial TIM OV LV BPL topology database, so the different deterministic TIM-BNI and stochastic NNIM-BNI approximations are expected in Table 4.

Table 4.
Branch Number Approximations of TIM-BNI and NNIM-BNI for the Default Operation Settings but for Frequency Range 3-88MHz and Three Representative Sets of OV LV BPL Topologies from the TIM OV LV BPL Topology Database

Indicative OV LV BPL Topologies of Table 1		Urban case A (Typical urban case)	Suburban case	Rural case	LOS case	RMSD	Notes
Actual Number of Branches N		3	2	1	0	-	-
TIM-BNI (Approximated Number of Branches) $N_{TIM-BNI}$	1 st representative set	2.40	2.20	0.80	0.80	0.52	Default Operation Settings (Frequency Range 3-88MHz + Representative Sets)
	2 nd representative set	3	2.80	0.80	0.80	0.57	
	3 rd representative set	2.60	2.40	0.80	0.80	0.50	
NNIM-BNI (Approximated Number of Branches) $N_{NNIM-BNI}$	1 st representative set	2.46	1.76	1.57	1.56	0.88	Default Operation Settings (Frequency Range 3-88MHz + Representative Sets) + 1 hidden layer
	2 nd representative set	3.42	2	0.99	0.94	0.52	
	3 rd representative set	3.59	1.81	1.06	1.01	0.590	
	1 st representative set	14.32	1.10	1.07	0.650	5.69	Default Operation Settings (Frequency Range 3-88MHz + Representative Sets) + 2 hidden layers
	2 nd representative set	1.94	1.85	1.85	1.84	1.15	
	3 rd representative set	3.83	2.09	0.930	0.870	0.61	
	1 st representative set	2.92	1.95	1.03	0.980	0.490	Default Operation Settings (Frequency Range 3-88MHz + Representative Sets) + 3 hidden layers
	2 nd representative set	2.02	2.02	2.02	2.02	1.23	
	3 rd representative set	3.05	2.03	1.06	1.03	0.52	
	1 st representative set	4.77	2.77	1	0.920	1.07	Default Operation Settings (Frequency
	2 nd representative set	2.93	1.94	1.30	1.29	0.66	

	representative set						Range 3-88MHz + Representative Sets) + 4 hidden layers
	3 rd representative set	2.45	1.81	1.37	1.36	0.76	
	1 st representative set	1.60	1.68	1.83	1.84	1.24	Default Operation Settings (Frequency Range 3-88MHz + Representative Sets) + 5 hidden layers
	2 nd representative set	3.56	5.62	1	0.68	1.86	
	3 rd representative set	5.64	2.24	1.01	0.94	1.41	

By comparing Tables 2-4, it is clear that the approximation performances of TIM-BNI and NNIM-BNI have significantly been improved, while RMSDs of NNIM-BNI become comparable to the ones of TIM-BNI. Indeed, the best RMSDs of TIM-BNI and NNIM-BNI after the selection of representative sets from the TIM OV LV BPL topology database of Table 3 are equal to 0.50 and 0.52, respectively, which are the best RMSDs among the Tables 2, 3 and 4. Among the indicative OV LV BPL topologies of Table 1, TIM-BNI better approximates the branches of urban case A (*i.e.*, the best TIM-BNI approximation is equal to 3, while the actual number of branches is equal to 3), whereas NNIM-BNI better approximates the branches of suburban, rural and LOS case A (*i.e.*, the best NNIM-BNI approximations are equal to 2, 1 and 0.68 when the actual numbers of branches are equal to 2, 1 and 0, respectively). In addition, the representative sets from the TIM OV LV BPL topology database first differentiate the NNIM-BNI approximations among the suburban rural and LOS cases and second improve the NNIM-BNI performance, when high number of hidden layers are applied. Note that the best branch number approximation per examined OV LV BPL topology is highlighted in green color in Table 4 as well the best RMSD. In general, the findings of this subsection highlight the problem of AI bias while the representative sets can define cleaner datasets from conscious or unconscious prejudices thus allowing more accurate approximations.

In this subsection, the performance improvement of TIM-BNI and NNIM-BNI has been highlighted when: (i) higher accuracies for the preparation of TIM OV LV BPL topology database, and (ii) representative sets depending on the examined indicative OV LV BPL topologies are applied. Apart from the impact of more sophisticated TIM OV LV BPL topology databases on TIM-BNI and NNIM-BNI performance, significant improvement can be achieved when the operation settings of TIM-BNI (*i.e.*, see Sec.4.3) and NNIM-BNI (*i.e.*, see Sec.4.4) are further explored as follows.

4.3 The Impact of R on TIM-BNI Performance

Apart from the operation settings that affect the preparation of the TIM OV LV BPL topology database and, thus, the performance of TIM-BNI and NNIM-BNI,

the operation settings of TIM-BNI that affect its approximation performance is studied in this subsection.

As already been mentioned in Sec. 3.1, the TIM-BNI branch number approximation $N_{\text{TIM-BNI}}$ comes from the average value of the branch numbers of the R OV LV BPL topologies of the TIM OV LV BPL topology database, which presents the R lowest RMSDs among the P computed ones, while the default value of R is equal to 5. In Table 5, the branch number approximations of TIM-BNI are reported, when the aforementioned default operation settings of Sec.4.1 are assumed but for six different values of R (i.e, 1, 2, 3, 5, 7 and 10). Apart from the branch number approximations, the actual branch numbers of the four examined OV LV BPL topologies of Table 1 are again presented. Also, RMSDs of TIM-BNI for the four examined OV LV BPL topologies and the six different values of R are demonstrated.

From Table 5, it is evident that RMSD depends on the value of R . As the TIM-BNI branch number approximations of urban case A, suburban case and rural case do not depend on the value of R , RMSD is only affected by the branch number approximation of LOS case. Since the LOS case is unique in the TIM OV LV BPL topology database, when R increases, this implies that $(R-1)$ OV LV BPL topologies of the TIM OV LV BPL topology database of different number of branches but with the $(R-1)$ lowest RMSDs are taken into account during the computation of the average of branch numbers. Therefore, as R increases, the number of approximate branches in the LOS case will also increase. Note that the best branch number approximation per examined OV LV BPL topology and the best RMSD are highlighted in green color in Table 5.

4.4 The Impact of Participation Percentages on NNIM-BNI Performance

Until now, the operation settings that affect the preparation of the TIM OV LV BPL topology database and the operation of TIM-BNI have been studied. In this subsection, the factors that affect the approximation performance of NNIM-BNI are analyzed. More specifically, the main factor that affects the operation of NNIM-BNI is the participation percentages of the three phases, *i.e.*, training, validation and testing. In Table 6, the branch number approximations of NNIM-BNI are reported, when the aforementioned default operation settings of Sec.4.1 are assumed but for seven participation percentage combinations –*i.e.*, (10%,45%,45%), (30%,35%,35%), (50%,25%,25%), (70%,15%,15%), (80%,10%,10%), (80%,10%,10%), (90%,5%,5%) and (98%,1%,1%)–. Apart from the branch number approximations, the actual branch numbers of the four examined OV LV BPL topologies of Table 1 are again presented. Also, RMSDs of TIM-BNI for the four examined OV LV BPL topologies and the seven different participation percentage combinations are demonstrated. Note that up to 5 hidden layers and one execution per hidden layer and participation percentage combination are assumed in Table 6.

Table 5.
Branch Number Approximations of TIM-BNI for the Default Operation Settings and Different R Values

Indicative OV LV BPL Topologies of Table 1		Urban case A (Typical urban case)	Suburban case	Rural case	LOS case	RMSD	Notes
Actual Number of Branches N		3	2	1	0	-	-
TIM-BNI (Approximated Number of Branches) $N_{TIM-BNI}$	$R=1$	3	3	2	0	0.71	Default Operation Settings
	$R=2$	3	3	2	0.50	0.75	
	$R=3$	3	3	2	0.67	0.78	
	$R=5$ (Default)	3	3	2	0.80	0.81	
	$R=7$	3	3	2	1	0.87	
	$R=10$	3	3	2	1.30	0.96	

Table 6.
Branch Number Approximations of NNIM-BNI for the Default Operation Settings and Different Participation Percentage Values of Training, Validation and Testing

Indicative OV LV BPL Topologies of Table 1		Urban case A (Typical urban case)	Suburban case	Rural case	LOS case	RMSD	Notes
Actual Number of Branches N		3	2	1	0	-	-
	Participation Percentages for Training, Validation and Testing (%,%,%)						
NNIM-BNI (Approximated Number of Branches) $N_{NNIM-BNI}$	(10%,45%,45%)	2.94	2.94	2.94	2.94	1.82	Default Operation Settings + 1 hidden layer
	(30%,35%,35%)	3.07	2.83	2.62	2.59	1.58	
	(50%,25%,25%)	2.41	2.41	2.41	2.41	1.44	
	(70%,15%,15%)	2.94	2.81	2.82	2.82	1.73	
	(80%,10%,10%)	3	2.49	2.49	2.49	1.47	
	(90%,5%,5%)	3.06	2.86	2.77	2.76	1.70	
	(98%,1%,1%)	3	3	2.55	2.55	1.58	Default Operation Settings + 2 hidden layers
	(10%,45%,45%)	5.03	2.82	2.58	2.52	1.85	
	(30%,35%,35%)	4.96	3.33	2.61	2.52	1.91	
	(50%,25%,25%)	5.71	3.44	2.53	2.44	2.10	
	(70%,15%,15%)	8.26	1.35	2.72	2.70	3.09	
	(80%,10%,10%)	5.58	3.47	2.61	2.56	2.12	
	(90%,5%,5%)	-51.36	54.23	2.60	2.53	37.72	
	(98%,1%,1%)	759.24	3.02	2.77	2.53	1.57	

	(10%,45%,45%)	6.15	6.14	2.56	2.40	2.97	Default Operation Settings + 3 hidden layers
	(30%,35%,35%)	2.98	3.35	2.47	2.23	1.50	
	(50%,25%,25%)	3.18	2.81	2.51	2.41	1.48	
	(70%,15%,15%)	2.87	2.86	2.84	2.83	1.74	
	Default						
	(80%,10%,10%)	5.40	3.39	2.61	2.56	2.05	
	(90%,5%,5%)	-0.250	0.40	2.93	2.66	2.45	
	(98%,1%,1%)	3.89	3.07	2.64	2.61	1.69	Default Operation Settings + 4 hidden layers
	(10%,45%,45%)	4.82	0.99	2.55	2.45	1.78	
	(30%,35%,35%)	2.21	5.93	2.51	2.36	2.44	
	(50%,25%,25%)	5.73	3.50	2.62	2.56	2.17	
	(70%,15%,15%)	3.01	-15.36	2.72	2.70	8.82	
	Default						
	(80%,10%,10%)	4.72	3.43	2.62	2.58	1.89	
	(90%,5%,5%)	4.89	3.24	2.61	2.58	1.90	Default Operation Settings + 5 hidden layers
	(98%,1%,1%)	2.98	2.87	2.87	2.86	1.76	
	(10%,45%,45%)	3.65	2.90	2.64	2.62	1.64	
	(30%,35%,35%)	4.38	2.87	2.63	2.58	1.73	
	(50%,25%,25%)	3.01	2.01	2.64	2.57	1.52	
	(70%,15%,15%)	354.21	2.15	2.06	2.19	175.61	
	Default						
	(80%,10%,10%)	2.24	1.63	2.71	2.49	1.57	
	(90%,5%,5%)	3	3	3.48	2.41	1.80	
	(98%,1%,1%)	5.50	3.51	2.59	2.55	2.09	

From Table 6, the significance of the validation and testing phases is outlined, since low RMSDs can be detected when high participation percentages of the previous phases (*i.e.*, above 15%) are assumed regardless of the number of hidden layers. Indeed, the highest RMSDs occurring are equal to 378.1 and 175.61, when participation percentage of validation phase is equal to 1% and 15%, respectively. Note that the lowest RMSD that is equal to 1.44 occurs, when one hidden layer is applied and the participation percentages for training, validation and testing are equal to 50%, 25% and 25%, respectively. Finally, 1 and 3 hidden layers offer more secure approximations regardless of the participation percentage combinations, since in all the other numbers of hidden layers, there is at least one participation percentage combination whose RMSD is above 5 renders unacceptable an approximation. Note that the best branch number approximation per examined OV LV BPL topology is highlighted in green color in Table 6 as well the best RMSD.

Concluding this Section, the approximation performance impact of a variety of settings that affects the preparation of the TIM OV LV BPL topology database and the operation of TIM-BNI and NNIM-BNI has been assessed. The factors that affect the preparation of the TIM OV LV BPL topology database, such as its accuracy degree and its representativeness, has the most significant effect on the approximation performance of TIM-BNI and NNIM-BNI thus rendering NNIM-BNI equivalent to TIM-BNI. On the basis of the factors that affect the accuracy degree of the TIM OV LV BPL topology database, the effect of lower values of the length spacing L_s for both branch distance and branch length and of higher values of the maximum branch length $L_{b,max}$ during the preparation of the TIM OV LV BPL topology database on the approximation performance of NNIM-BNI is as subject of future research.

5. Conclusions

In this paper, the branch number approximation methods of TIM-BNI and NNIM-BNI have been proposed, while the factors that affect their approximation performance have been recognized and benchmarked. The factors that affect the preparation of the TIM OV LV BPL topology database, which is the big data input of TIM-BNI and NNIM-BNI, have a significant impact on their approximation performance; the accuracy degree and the representativeness of the TIM OV LV BPL topology database have significantly improved RMSDs of the branch number approximations of both TIM-BNI and NNIM-BNI. As the operation settings of TIM-BNI are concerned, it has been revealed that the least the number of OV LV BPL topologies of the TIM OV LV BPL topology database are taken into account during the deterministic TIM-BNI branch number approximation, the better the RMSDs of the TIM-BNI approximations get. As the operation settings of NNIM-BNI are regarded, the hidden layers and the participation percentages of training, validation and testing may affect the stochastic NNIM-BNI branch number approximations. In fact, the best approximation performances with reference to RMSD have been reported when below three hidden layers and high participation percentages of the validation and testing phases are assumed. In the future research steps, TIM-BNI and NNIM-BNI are going to be further elaborated and expanded in order to cope with the fervent issues of the operation of the smart grid.

CONFLICTS OF INTEREST

The author declares that there is no conflict of interests regarding the publication of this paper.

References

- [1] F. Aalamifar and L. Lampe, "Optimized WiMAX profile configuration for smart grid communications," *IEEE Transactions on Smart Grid*, vol. 8, no. 6, pp. 2723-2732, 2017.
- [2] A. G. Lazaropoulos, "Wireless Sensor Network Design for Transmission Line Monitoring, Metering and Controlling Introducing Broadband over PowerLines-enhanced Network Model (BPLeNM)," *ISRN Power Engineering*, vol. 2014, Article ID 894628, 22 pages, 2014. doi:10.1155/2014/894628. [Online]. Available: <http://www.hindawi.com/journals/isrn.power.engineering/2014/894628/>
- [3] A. G. Lazaropoulos, "Improvement of Power Systems Stability by Applying Topology Identification Methodology (TIM) and Fault and Instability Identification Methodology (FIIM)–Study of the Overhead Medium-Voltage Broadband over Power Lines (OV MV BPL) Networks Case," *Trends in*

- Renewable Energy*, vol. 3, no. 2, pp. 102-128, Apr. 2017. [Online]. Available: <http://futureenergysp.com/index.php/tre/article/view/34>
- [4] A. G. Lazaropoulos, "Main Line Fault Localization Methodology in Smart Grid—Part 1: Extended TM2 Method for the Overhead Medium-Voltage Broadband over Power Lines Networks Case," *Trends in Renewable Energy*, vol. 3, no. 3, pp. 2-25, Dec. 2017. [Online]. Available: <http://futureenergysp.com/index.php/tre/article/view/36>
- [5] A. G. Lazaropoulos, "Business Analytics and IT in Smart Grid – Part 1: The Impact of Measurement Differences on the iSHM Class Map Footprints of Overhead Low-Voltage Broadband over Power Lines Topologies," *Trends in Renewable Energy*, vol. 6, no. 2, pp. 156-186, May 2020. [Online]. Available: <http://futureenergysp.com/index.php/tre/article/view/117/pdf>
- [6] M. H. Rehmani, M. Reisslein, A. Rachedi, M. Erol-Kantarci, and M. Radenkovic, "Integrating renewable energy resources into the smart grid: recent developments in information and communication technologies," *IEEE Transactions on Industrial Informatics*, vol. 14, no. 7, pp. 2814-2825, 2018.
- [7] F. R. Yu, P. Zhang, W. Xiao, and P. Choudhury, "Communication systems for grid integration of renewable energy resources," *IEEE Network*, vol. 25, no. 5, pp. 22–29, Sep. 2011.
- [8] B. Heile, "Smart grids for green communications [industry perspectives]," *IEEE Wireless Commun.*, vol. 17, no. 3, pp. 4–6, Jun. 2010.
- [9] A. G. Lazaropoulos, "Review and Progress towards the Capacity Boost of Overhead and Underground Medium-Voltage and Low-Voltage Broadband over Power Lines Networks: Cooperative Communications through Two- and Three-Hop Repeater Systems," *ISRN Electronics*, vol. 2013, Article ID 472190, pp. 1-19, 2013. [Online]. Available: <http://www.hindawi.com/isrn/electronics/aip/472190/>
- [10] A. S. de Beer, A. Sheri, H. C. Ferreira, and A. H. Vinck, "Channel frequency response for a low voltage indoor cable up to 1GHz," In *Power Line Communications and its Applications (ISPLC), 2018 IEEE International Symposium on*, pp. 1-6, 2018.
- [11] A. G. Lazaropoulos and P. G. Cottis, "Transmission characteristics of overhead medium voltage power line communication channels," *IEEE Trans. Power Del.*, vol. 24, no. 3, pp. 1164-1173, Jul. 2009.
- [12] A. G. Lazaropoulos and P. G. Cottis, "Capacity of overhead medium voltage power line communication channels," *IEEE Trans. Power Del.*, vol. 25, no. 2, pp. 723-733, Apr. 2010.
- [13] A. G. Lazaropoulos and P. G. Cottis, "Broadband transmission via underground medium-voltage power lines-Part I: transmission characteristics," *IEEE Trans. Power Del.*, vol. 25, no. 4, pp. 2414-2424, Oct. 2010.
- [14] A. G. Lazaropoulos and P. G. Cottis, "Broadband transmission via underground medium-voltage power lines-Part II: capacity," *IEEE Trans. Power Del.*, vol. 25, no. 4, pp. 2425-2434, Oct. 2010.
- [15] E. Biglieri, "Coding and modulation for a horrible channel," *IEEE Commun. Mag.*, vol. 41, no. 5, pp. 92–98, May 2003.
- [16] M. Gebhardt, F. Weinmann, and K. Dostert, "Physical and regulatory constraints for communication over the power supply grid," *IEEE Commun. Mag.*, vol. 41, no. 5, pp. 84-90, May 2003.

- [17] P. S. Henry, "Interference characteristics of broadband power line communication systems using aerial medium voltage wires," *IEEE Commun. Mag.*, vol. 43, no. 4, pp. 92-98, Apr. 2005.
- [18] S. Liu and L. J. Greenstein, "Emission characteristics and interference constraint of overhead medium-voltage broadband power line (BPL) systems," in *Proc. IEEE Global Telecommunications Conf.*, New Orleans, LA, USA, Nov./Dec. 2008, pp. 1-5.
- [19] M. Götz, M. Rapp, and K. Dostert, "Power line channel characteristics and their effect on communication system design," *IEEE Commun. Mag.*, vol. 42, no. 4, pp. 78-86, Apr. 2004.
- [20] A. G. Lazaropoulos, "Towards Modal Integration of Overhead and Underground Low-Voltage and Medium-Voltage Power Line Communication Channels in the Smart Grid Landscape: Model Expansion, Broadband Signal Transmission Characteristics, and Statistical Performance Metrics (Invited Paper)," *ISRN Signal Processing*, vol. 2012, Article ID 121628, pp. 1-17, 2012. [Online]. Available: <http://www.hindawi.com/isrn/sp/2012/121628/>
- [21] D. G. Della and S. Rinaldi, "Hybrid Communication Network for the Smart Grid: Validation of a Field Test Experience," *IEEE Trans. Power Del.*, vol. 30, no. 6, pp. 2492-2500, 2015.
- [22] F. Versolatto and A. M. Tonello, "An MTL theory approach for the simulation of MIMO power-line communication channels," *IEEE Trans. Power Del.*, vol. 26, no. 3, pp. 1710-1717, Jul. 2011.
- [23] P. Amirshahi and M. Kavehrad, "High-frequency characteristics of overhead multiconductor power lines for broadband communications," *IEEE J. Sel. Areas Commun.*, vol. 24, no. 7, pp. 1292-1303, Jul. 2006.
- [24] L. Stadelmeier, D. Schneider, D. Schill, A. Schwager, and J. Speidel, "MIMO for inhome power line communications," presented at the *Int. Conf. on Source and Channel Coding*, Ulm, Germany, Jan. 2008.
- [25] T. Sartenaer, "Multiuser communications over frequency selective wired channels and applications to the powerline access network" *Ph.D. dissertation*, Univ. Catholique Louvain, Louvain-la-Neuve, Belgium, Sep. 2004.
- [26] T. Calliacoudas and F. Issa, "'Multiconductor transmission lines and cables solver,' An efficient simulation tool for plc channel networks development," presented at the *IEEE Int. Conf. Power Line Communications and Its Applications*, Athens, Greece, Mar. 2002.
- [27] S. Galli and T. Banwell, "A deterministic frequency-domain model for the indoor power line transfer function," *IEEE J. Sel. Areas Commun.*, vol. 24, no. 7, pp. 1304-1316, Jul. 2006.
- [28] S. Galli and T. Banwell, "A novel approach to accurate modeling of the indoor power line channel-Part II: Transfer function and channel properties," *IEEE Trans. Power Del.*, vol. 20, no. 3, pp. 1869-1878, Jul. 2005.
- [29] A. Pérez, A. M. Sánchez, J. R. Regué, M. Ribó, R. Aquilué, P. Rodríguez-Cepeda, and F. J. Pajares, "Circuitual and modal characterization of the power-line network in the PLC band," *IEEE Trans. Power Del.*, vol. 24, no. 3, pp. 1182-1189, Jul. 2009.
- [30] T. Sartenaer and P. Delogne, "Deterministic modelling of the (Shielded) outdoor powerline channel based on the multiconductor transmission line equations," *IEEE J. Sel. Areas Commun.*, vol. 24, no. 7, pp. 1277-1291, Jul. 2006.

- [31] T. Sartenaer and P. Delogne, "Powerline cables modelling for broadband communications," in *Proc. IEEE Int. Conf. Power Line Communications and Its Applications*, Malmö, Sweden, Apr. 2001, pp. 331-337.
- [32] C. R. Paul, *Analysis of Multiconductor Transmission Lines*. New York: Wiley, 1994.
- [33] J. A. B. Faria, *Multiconductor Transmission-Line Structures: Modal Analysis Techniques*. New York: Wiley, 1994.
- [34] H. Meng, S. Chen, Y. L. Guan, C. L. Law, P. L. So, E. Gunawan, and T. T. Lie, "Modeling of transfer characteristics for the broadband power line communication channel," *IEEE Trans. Power Del.*, vol. 19, no. 3, pp. 1057-1064, Jul. 2004.
- [35] A. Semlyen and B. Gustavsen, "Phase-domain transmission-line modeling with enforcement of symmetry via the propagated characteristic admittance matrix," *IEEE Trans. Power Del.*, vol. 27, no. 2, pp. 626-631, Apr. 2012.
- [36] A. G. Lazaropoulos, "Statistical Broadband over Power Lines Channel Modeling – Part 1: The Theory of the Statistical Hybrid Model," *Progress in Electromagnetics Research C*, vol. 92, pp. 1-16, 2019. [Online]. Available: <http://www.jpier.org/PIERC/pierc92/01.19012902.pdf>
- [37] A. G. Lazaropoulos, "Measurement Differences, Faults and Instabilities in Intelligent Energy Systems – Part 2: Fault and Instability Prediction in Overhead High-Voltage Broadband over Power Lines Networks by Applying Fault and Instability Identification Methodology (FIIM)," *Trends in Renewable Energy*, vol. 2, no. 3, pp. 113-142, Oct. 2016. [Online]. Available: <http://futureenergysp.com/index.php/tre/article/view/27/33>
- [38] A. G. Lazaropoulos, "Measurement Differences, Faults and Instabilities in Intelligent Energy Systems–Part 1: Identification of Overhead High-Voltage Broadband over Power Lines Network Topologies by Applying Topology Identification Methodology (TIM)," *Trends in Renewable Energy*, vol. 2, no. 3, pp. 85-112, Oct. 2016. [Online]. Available: <http://futureenergysp.com/index.php/tre/article/view/26/32>
- [39] Y. Huo, G. Prasad, L. Lampe, and V. C. Leung, "Advanced Smart Grid Monitoring: Intelligent Cable Diagnostics using Neural Networks," in *Proc. IEEE Int. Symp. Power Line Communications and its Applications*, May 2020, pp. 1-6.
- [40] A. M. Tonello, N. A. Letizia, D. Righini, and F. Marcuzzi, "Machine learning tips and tricks for power line communications," *IEEE Access*, vol. 7, pp. 82434-82452, 2019.
- [41] Y. Cui, X. Liu, J. Cao, and D. Xu, "Network Performance Optimization for Low-Voltage Power Line Communications," *MDPI Energies*, vol. 11, no. 5, pp. 1266-1290, 2018.
- [42] M. Ibnkahla, "Applications of neural networks to digital communications—a survey. Signal processing," vol. 80, no. 7, pp. 1185-1215, 2020.
- [43] D. Okoh, *Computer Neural Networks on MATLAB*. CreateSpace Independent Publishing Platform, 2016.
- [44] K. P. Murphy, *Machine Learning: A Probabilistic Perspective*. Cambridge, MA, USA: MIT Press, 2012.
- [45] A. G. Lazaropoulos, "Statistical Channel Modeling of Overhead Low Voltage Broadband over Power Lines (OV LV BPL) Networks – Part 1: The Theory of Class Map Footprints of Real OV LV BPL Topologies, Branch Line Faults and Hook-Style Energy Thefts," *Trends in Renewable Energy*, vol. 6, no. 1, pp. 61-87,

- Mar. 2020. [Online]. Available: <http://futureenergysp.com/index.php/tre/article/download/112/pdf>
- [46] OPERA1, D44: Report presenting the architecture of plc system, the electricity network topologies, the operating modes and the equipment over which PLC access system will be installed, IST Integr. Project No 507667, Dec. 2005.
- [47] P. Amirshahi, "Broadband access and home networking through powerline networks" Ph.D. dissertation, Pennsylvania State Univ., University Park, PA, May 2006.
- [48] M. D'Amore and M. S. Sarto, "A new formulation of lossy ground return parameters for transient analysis of multiconductor dissipative lines," *IEEE Trans. Power Del.*, vol. 12, no. 1, pp. 303-314, Jan. 1997.
- [49] M. D'Amore and M. S. Sarto, "Simulation models of a dissipative transmission line above a lossy ground for a wide-frequency range-Part I: Single conductor configuration," *IEEE Trans. Electromagn. Compat.*, vol. 38, no. 2, pp. 127-138, May 1996.
- [50] M. D'Amore and M. S. Sarto, "Simulation models of a dissipative transmission line above a lossy ground for a wide-frequency range-Part II: Multi-conductor configuration," *IEEE Trans. Electromagn. Compat.*, vol. 38, no. 2, pp. 139-149, May 1996.
- [51] A. G. Lazaropoulos, "Broadband Performance Metrics and Regression Approximations of the New Coupling Schemes for Distribution Broadband over Power Lines (BPL) Networks," *Trends in Renewable Energy*, vol. 4, no. 1, pp. 43-73, Jan. 2018. [Online]. Available: <http://futureenergysp.com/index.php/tre/article/view/59/pdf>
- [52] A. G. Lazaropoulos, "New Coupling Schemes for Distribution Broadband over Power Lines (BPL) Networks," *Progress in Electromagnetics Research B*, vol. 71, pp. 39-54, 2016. [Online]. Available: <http://www.jpier.org/PIERB/pierb71/02.16081503.pdf>
- [53] I. C. Demetriou, "An application of best L1 piecewise monotonic data approximation to signal restoration," *IAENG International Journal of Applied Mathematics*, vol. 53, no. 4, pp. 226-232, 2013.
- [54] I. C. Demetriou, "L1PMA: A Fortran 77 Package for Best L1 Piecewise Monotonic Data Smoothing," *Computer Physics Communications*, vol. 151, no. 1, pp. 315-338, 2003.
- [55] Y. T. Ma, K. H. Liu, and Y. N. Guo, "Artificial neural network modeling approach to power-line communication multi-path channel," in *Proc. Int. Conf. Neural Netw. Signal Process*, Jun. 2008, pp. 229-232.
- [56] R. Hecht-Nielsen, "Theory of the backpropagation neural network," *Neural networks for perception. Academic Press*, pp. 65-93, 1992.
- [57] D. Okoh, Neural Network Training Code (<https://www.mathworks.com/matlabcentral/fileexchange/59362-neural-network-training-code>), MATLAB Central File Exchange. Retrieved April 22, 2020.
- [58] F. Pan, W. Wang, A. K. Tung, and J. Yang, "Finding representative set from massive data," In *Fifth IEEE International Conference on Data Mining (ICDM'05)*, Nov. 2005.
- [59] S. V. R. Kannan and A. Veta, "On clusterings: Good, bad and spectral," *Journal of the ACM (JACM)*, vol. 51, no. 3, pp. 497-515, 2000.

- [60] D. S. Hochbaum and A. Pathria, "Analysis of the greedy approach in problems of maximum k-coverage," *Naval Research Quarterly*, vol. 45, pp. 615-627, 1998.

Article copyright: © 2021 Athanasios G. Lazaropoulos. This is an open access article distributed under the terms of the [Creative Commons Attribution 4.0 International License](https://creativecommons.org/licenses/by/4.0/), which permits unrestricted use and distribution provided the original author and source are credited.



World on the Road to 100% Renewable Energy

Nima Norouzi, Maryam Fani*

Department of Energy Engineering and Physics, Amirkabir University of Technology (Tehran Polytechnic), 424 Hafez Avenue, PO. Box 15875-4413, Tehran, Iran

Received September 11, 2021; Accepted October 19, 2021; Published October 28, 2021

In the study, the current and future status of renewable energy resources were compiled in the light of large databases of national and international renewable energy institutions, and the latest situation in the world in the transition to 100% renewable energy was examined. The extent of the goal for the transition to 100% renewable energy has been determined, and predictions have been made based on all this information. In today's world where energy and environmental problems are on the agenda, countries' transition to renewable energy is the primary solution. This goal is called the transition to 100% renewable energy, which brings advantages such as providing needed energy and producing clean energy. Today, renewable energy sources account for more than one-third of the global energy capacity, and the world is rapidly moving towards 100% renewable energy. Compared with 2017, the total amount of renewable energy in 2018 increased by 181 GW, and the number of countries with an increase in the proportion of renewable energy increased. Taking into account the external dependence of the use of fossil fuels and environmental issues, this development is at a promising level in the future. In order to shift from highly polluting oil resources to natural gas and renewable resources, this article aims to investigate the current global energy transition trends, and then propose some important strategies to get closer to upstream goals and obligations in this way.

Keywords: 100% Renewable energy; Alternative energy sources; Fossil fuel; Energy policy; Sustainable economics

1. Introduction

Today, energy has become one of the most vital needs of the world and humanity. Due to the increasing demands and the production processes developed to meet these demands, the energy use is also increasing. To find permanent solutions to the energy demands, it is necessary to define energy problems correctly, find applicable solutions, distinguish between old and current best energy technologies, and not use old technologies that do more harm than good [1, 2]. From the perspective of energy market and energy demand, fossil fuels are under pressure, which gives the newly mature renewable energy market an advantage. Renewable energy including solar energy, wind energy, geothermal energy, hydro energy, ocean energy, biomass energy and hydrogen energy can be listed as renewable energy sources [2].

Fossil fuels pose a critical problem, as they cause global climate change and environmental problems. Fossil fuels are not endless resources and are in danger of extinction. Due to the greenhouse gases formed by fossil fuels in energy production. The

*Corresponding author: mfani@aut.ac.ir

limitation of fossil fuel sources necessitates the diversification of energy sources to ensure the availability of energy. It is predicted that turning to new and renewable energy sources will be the right step in meeting the energy needs of the future [3].

With the development of technology, industrialization and the improvement of living standards, the energy resources of countries, how they use these energy sources, how efficiently they use them, and how they evaluate, control, and develop have also effectively shaped the country's political process. The energy independence of the countries adds political decisiveness. For all these reasons, studies to increase the use of renewable energy sources in production planning for the future are also gaining momentum [4-6].

To meet the increasing energy demand in countries, reduce foreign dependency on energy resources, and make an environmentally friendly production, it is important to use renewable energy resources at the highest level. Various renewable energy sources have a utilizable potential to provide added value to the economy in countries. The fact that the potential is not fully utilized puts the world's economy under pressure and causes negative effects on the ecosystem, especially air pollution and climate change [7].

The most up-to-date and effective solution proposal for improving similar problems experienced on a global scale is accepted as the "Transition to 100% Renewable Energy" approach. Renewable energy includes high entropy resources suitable for realizing and converting energy production of the desired quality [8]. The benefits of transitioning to 100% renewable energy can be listed as a fuel source, possible decrease in energy prices, reducing foreign dependency on energy, a safe and clean energy production, improvement of air, water, and environmental pollution, protection of public health, and regulation of the local economy [9].

Of course, besides the advantages of renewable energy sources such as clean energy and infinite, some disadvantages should be considered. These relate to limited potential, high cost, and energy densities. The high initial investment costs of the projects for renewable energy sources in energy production and energy storage problems create a disadvantage in using renewable energy sources [9].

Renewable energy sources currently account for more than one-third of global energy capacity [10]. More than 1 gigawatts (GW) of renewable power capacity was installed in more than ninety countries in 2018. In recent years, cities and countries have seen an increasing movement towards meeting 100% of energy from renewable sources. Countries such as Norway, Costa Rica, China, Germany, and Sweden have set the targets of their local energy sectors as "100% transition to renewable energy sources" [11].

According to the Renewable Energies 2019 Global Status Report, 2018 experienced a relatively stable market for renewable energy technologies, with a total renewable energy increase of 181 GW compared to 2017, and the number of countries growing their share of renewable energy continues to increase. Renewable energy sources provided an estimated more than 26% of global electricity generation by year-end, but renewable energy options provide only 10% and 3% of the energy needed for heating and transportation. Increasing renewable technologies and improving integration between the energy, heating, cooling, and transport sectors will enable the transition to a fully renewable energy world [12]. Investments in the transition to 100% renewable energy, which started to gain momentum in 2013, increased steadily towards the end of 2015 and reached 290 billion dollars. Due to reducing carbon dioxide emissions released into the atmosphere and creating a healthier environment, the transition to 100% renewable energy is the only way to offer a healthy life to all humanity in a sustainable structure. To

become a world that has switched to 100% renewable energy by 2050 using existing renewable energy technologies, it is necessary to use all renewable energy sources together and develop storage technologies [13]. Global pressures due to the negative effects on both national economies and environmental resources, depending on the technologies applied for the extraction and use of the natural resources they use while meeting the countries' energy needs, make the implementation of 100% renewable energy transition policies inevitable. In this context, this study aims for the readers to access the most up-to-date information on the subject by compiling the sources and academic articles of internationally accepted international institutions where the records of up-to-date statistical information are kept. In light of the data obtained in this context, it aims to reveal a road map suitable for the world's socio-economic structure in line with the transition to 100% renewable energy [14].

2. Renewable Energy Sources

This section gives brief information about the current status of renewable energy resources on an international scale.

2.1 Biomass

Biomass is an important renewable and sustainable energy source that is thought to replace fossil fuel sources. Wood, agricultural products, agricultural by-product waste, animal waste, municipal solid waste, sewage sludge from wastewater treatment plants, wastes from food processing, aquatic plants, and algae are the most important biomass sources [15]. It is foreseen that biomass and bioenergy will play a vital role in the future of the global energy scenario in producing heat and power, chemicals, and fuels. Bioenergy has recently received special attention by decreasing fossil fuel resources and increasing environmental concerns [16]. Bioenergy contributes to poverty reduction in developing countries. Bioenergy is considered the best alternative fuel that meets energy requirements. It can meet energy demands in the future, with its advantages such as providing the necessary energy at all times without complex energy conversion and expensive processes and being environmentally friendly. By 2050, it is predicted that more than 25% of the world's primary energy will be obtained from biomass [17]. Bioenergy is among the energy sources that make the most important contribution to the global renewable energy supply. It has been reported to contribute an estimated 12.4% to final global energy consumption as of the end of 2017. 5% of the global heating supply, 3% of the transportation, and 2% of the electricity supply were provided from bioenergy. According to 2018 data, China is the world leader in this field, while the USA, Brazil, India, and Germany are among the countries that follow China [18].

2.2 Geothermal Energy

Geothermal energy, the earth's internal heat, is based on spreading this internal heat from the hot region in the center to the earth and is used in many areas such as electrical energy production, heating, agriculture, greenhouse cultivation, and fishing. The world's installed capacity of geothermal energy is expressed in two ways: power generation and heat generation. Total geothermal power generation in 2018 is estimated at 630 PJ, of which about half is used for electricity purposes (89.3 TWh). A new

geothermal energy capacity of 0.5 GW was created in 2018, and the global total was 13.3 GW [13].

With the geothermal energy projects completed in 2018, Turkey increased its installed capacity by 21% (219 MW) to 1.3 GW. Indonesia increased its geothermal capacity by 140 MW and its installed capacity to 1.95 GW [17]. USA, Iceland, New Zealand, Croatia, Philippines, and Kenya follow these two countries. Countries on an active tectonic belt can be mentioned as geothermal-rich due to their geological and geographical location. Approximately tens of thousands of geothermal springs in natural outflows at different temperatures are scattered worldwide[18].

2.3 Hydropower

Hydropower is a renewable energy source that has greatly expanded its role in electricity generation due to factors such as the increase in electricity demand and the increase in turbine efficiency. It is especially popular in emerging markets in Asia, Latin America, and Africa[19]. In 2018, the total installed power in the global hydropower market increased by 20 GW and reached 1132 GW. The top 10 countries in total hydropower capacity (respectively) are China, Brazil, Canada, United States of America, Russian Federation, India, Norway, Turkey, Japan, and France, and these countries represent two-thirds of the global capacity [20].

2.4 Ocean Energy

Wide and powerful oceans store enough energy in heat, current, waves, and tides to meet the total energy demand worldwide many times over. However, ocean energy still makes up only a small part of the world's energy supply today. Concerns about global climate change and other environmental effects of dependence on fossil fuels worldwide have increased interest in renewable energy and ocean energy. As global reliance on renewable energies grows in the future, there will be greater interest in large ocean energy stores. Ocean energy is a renewable energy source that represents the smallest segment of the renewable energy market. Most of the projects with this type of energy are small-scale and pilot projects, and it was calculated that there was an operating capacity of 532 MW in 2018. Although the resource potential of ocean energy is high, its use is unfortunately not common. The support of ocean power technologies, especially by governments in Europe and North America, has strengthened electricity generation with ocean energy [21, 22].

2.5 Solar Energy

Solar energy is a primary energy source widely applied in heating, architecture, urban planning, agriculture, horticulture, transportation, and fuel production applications. Demand for solar energy is increasing in emerging markets and Europe. Solar energy showed the highest electricity production values in 2018 and became one of the most sought-after renewable energy types globally. More than 100 GW of capacity in solar energy was added to the annual global market, and the total capacity was 505.5 GW at the end of the year [23]. Especially in the United States and Europe, solar energy capacity has increased significantly. It also builds solar power plants to run mining, manufacturing, and other industries worldwide [24]. By 2018, solar energy capacity has increased by 1 GW or more in 32 countries [19]. China accounts for approximately 74% of the global capacity in solar energy, followed by Turkey, Brazil, and the USA [25].

2.6 Wind Power

Wind energy is a renewable energy source whose global market is developing steadily, increasing its capacity by approximately 51 GW in 2018. Wind power capacity increased by 9% in 2018 to 591 GW. In 2017, record wind energy capacity was experienced in Europe and India, but this situation did not show the same stability in 2018, while there was remarkable growth in other regions and countries. The largest regional market was Asia with 52%. Seven countries in Europe and two in Asia increased their capacity by 4.5 GW and global capacity by 24% to 23.1 GW [22].

2.7 Hydrogen Energy

Today's increased investment and cheaper renewable energy supply will impact hydrogen production costs and increase the shift from fossil fuels to cheaper renewable energy. This fact confirms that hydrogen energy technologies will play an important role in reaching the 100% renewable energy target [26].

Hydrogen produces nearly zero emissions, and its abundant natural resources can be an ideal sustainable energy source. Unlike hydrogen, fossil fuel sources cause serious environmental problems such as air pollution and global warming. Hydrogen should be produced from clean and rich sources with environmentally friendly methods to eliminate the negative effects of fossil fuel use on the environment, human health, and climate. Hydrogen energy produced from renewable energy sources will pave the way for a permanent energy system [23].

Many projects are being produced globally for hydrogen energy to become widespread, and various pilot plants are being established. The hydrogen-powered bus in many countries, such as Turkey's wind hydrogen production projects, are among the pilot plant studies. Apart from this, there are many examples of pilot-scale projects in the world. Among these projects, small hydroelectric power plants established for hydrogen production in China, hydrogen-producing wind turbines in Argentina, hydrogen-fueled vehicles in South Korea and India are examples of these studies. In addition, it is planned to produce hydrogen with solar panels in Libya, and the use of hydrogen is becoming common in countries such as Portugal, Colombia, Egypt, Russia, and Italy [28].

3. 100% Renewable Energy

Fossil fuels resources face increasing supply, environmental pollution, and climate change problems, while renewable energy can offer the best prospects for energy. Renewable energy sources differ from fossil fuels in many important ways. The concept of transition to 100% renewable energy means using completely renewable energy sources in all areas where energy is used, especially in electricity generation, transportation, and heating/cooling. Achieving this goal will reduce unsustainable energy demand, increase energy efficiency, and produce much cheaper and cleaner energy [11].

In this section, it provides information on the path taken by the world's 100% renewable energy from the past to the present, and explains the work done to accelerate the global and local transition to 100% renewable energy.

3.1 Transition to 100% Renewable Energy in the World

Progress in the renewable energy sector continues to be concentrated in electricity generation, while there is much less growth in heating, cooling, and transportation.

Electricity accounts for only one-fifth of global energy consumption, and the role of renewable energies in the transport and heating sectors remains critical to the energy transition [9]. Globally, 2018 has drawn a stable profile in the transition to 100% renewable energy. Compared to 2017, 181 GW of renewable energy was added and the number of countries making progress in the transition to 100% renewable energy increased. The renewable energy sector generally provided around 11 million (direct and indirect) employments worldwide in 2018 [11]. Although progress has been made in energy efficiency and transition to 100% renewable energy, it is behind the World Sustainable Development Goals and the Paris Agreement globally. Global energy-related carbon dioxide (CO₂) emissions increased by 1.7% in 2018 due to increased fossil fuel consumption. Fossil fuel use has increased by 11% since 2017 [22]. Fossil fuel companies continue to spend hundreds of millions of dollars on advertising to delay, control or thwart climate change policies and influence public opinion.

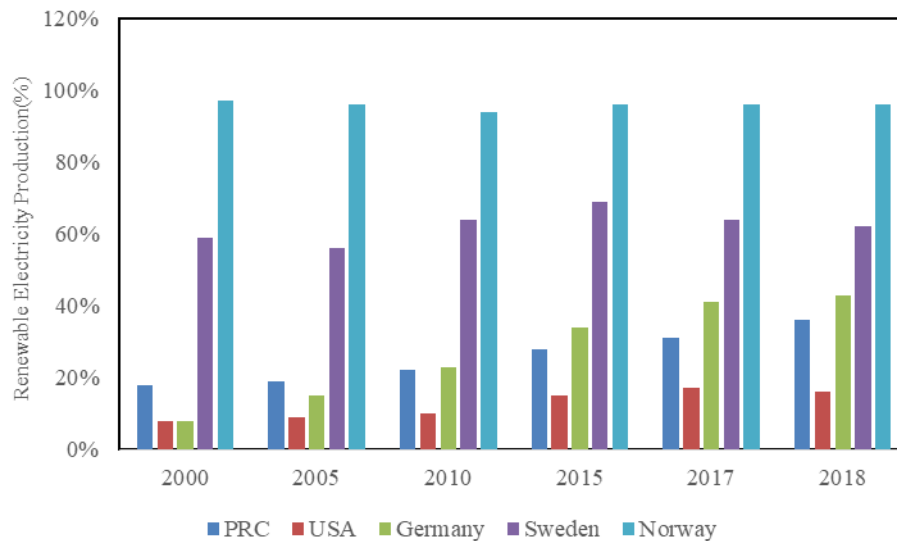


Figure 1. Renewable electricity production (%) of countries [28]

In Figure 1, renewable energy productions of countries that are one step ahead of other countries in the transition to 100% renewable energy are compared. When the renewable energy production of China, the United States of America, Germany, Sweden, and Norway (which is one step ahead of other countries in the transition to 100% renewable energy) is compared with each other, it is seen that Norway has switched to 100% renewable energy. All of its electrical energy is from renewable energy appears to be met. Sweden, closest to the transition to 100% renewable energy, follows Norway in second place. China, the USA, and Germany are also countries that have made progress in the transition to 100% renewable energy with their ever-increasing renewable energy profiles [29].

Figure 2 shows the share of countries' renewable production in total consumption and information about the status of renewable production in total consumption.

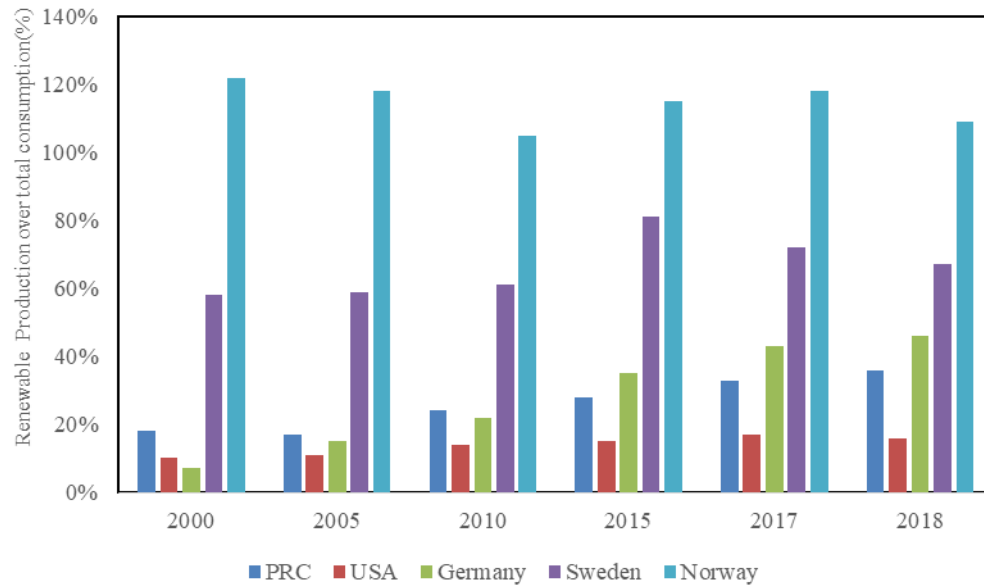


Figure 2. Share of renewable energy production(%) of countries in total consumption [18]

When the data in Figure 2 are analyzed statistically, Norway has a high production rate approaching or even exceeding 120%, because there is more renewable production than consumption in Norway, and the share of renewable production in total consumption is high. Sweden follows Norway in second place. It is observed that the share of renewable generation in the USA total consumption is low. Figure 3 shows the electrical energy consumption in different countries [30].

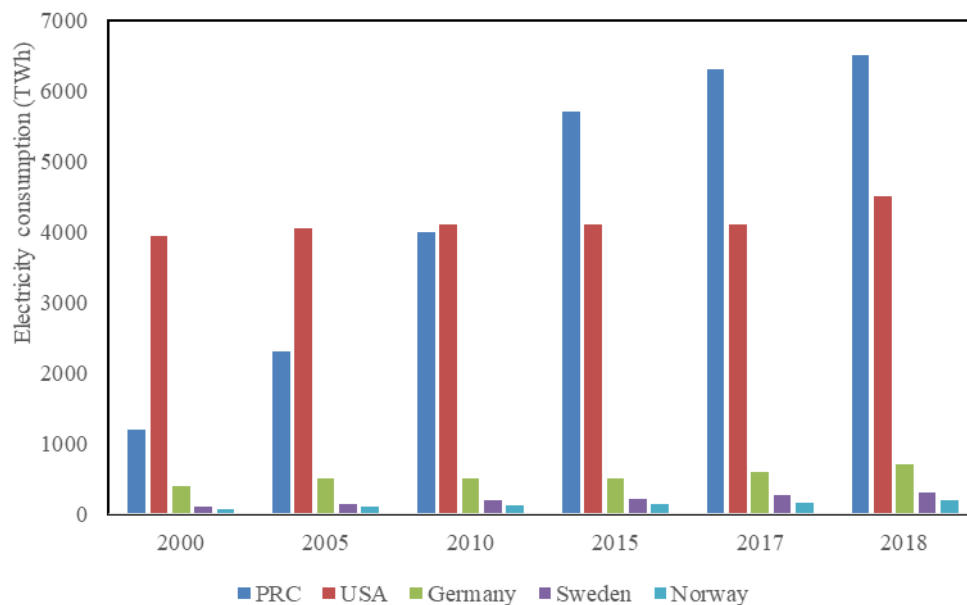


Figure 3. Electricity consumption of countries (TWh) [14]

When Figure 3 is examined, the total electrical energy consumption in China, where the share of renewable generation is low, was 6500 TWh in 2018, only about a

quarter of which can be met from renewable energy production. This is also true for the USA. Despite the electricity consumption of 4500 TWh in 2018, only about 18% of this energy is met by renewable generation [15]. In the light of this information, it is seen that although energy consumption is high, the share of renewable generation in this consumption share is low in many countries except Sweden. The energy consumed cannot be satisfied with renewable energy, and there is still a long way to go to satisfy it [31].

Countries aiming to transition to 100% renewable energy have many initiatives, small or large, to achieve this goal. According to 2018 International Energy Agency data, the share of global electricity generation from renewable energy was 26%. This situation shows that there is a 26% transition to 100% renewable energy globally. By 2018, 169 countries aim to transition to 100% renewable energy at the national or state/provincial level [17]. Since buses contribute more to air pollution than other public transport vehicles, solar buses in Uganda, solar ferries in India, and wind-powered trains in the Netherlands have begun to be used to switch to renewable power [19]. Countries also implement several policy measures to move forward on the path to 100% renewable energy. In Australia, the University of New South Wales has become the world's first fully solar-powered university, and it will start working with 100% solar energy by 2020. Again, many universities in Kenya (including Strathmore and Kenyatta Universities) use solar panels for their energy supply and earn money by selling the electricity they produce to the national grid. Scotland aims to produce all its electrical energy from renewable energy sources by 2020. Albania, Norway, and Costa Rica are among the countries that have transitioned to 100% renewable energy [27]. In the Dutch rail network systems, 100% of its trains are powered by the Catholic Diocese wind energy. In England, they have committed to switch to 100% renewable energy and buy renewable energy. In light of all this information, it is possible to say that the share of renewable generation has increased globally, the transition to 100% renewable energy has accelerated, and all developed, and developing countries have taken steps in this regard [32].

3.2 Towards the Future

The energy issue is a big problem all over the world. Most energy problems arise from providing rent, not making the right investments, and risky projects. Switching to renewable and 100% renewable energy will be the cleanest and right solution [11]. For the transition to 100% renewable energy, an energy system based on efficiency, scientifically appropriate, and protected by laws from political influences should be introduced, leaving aside the discussion of profit/loss in the energy sector [9].

Most countries are dependent on foreign sources at a rate of 60-75% in electrical energy production. The regulations that are tried to be implemented within the scope of the Energy Efficiency regulations cannot take a very important distance in this regard. This dependency, unfortunately, also hinders independence in political and economic terms [32-34].

In the transition to 100% renewable energy, the most important thing that can be done to achieve the target is the efforts of local governments to achieve the target [11]. The local government authorities' targeting of transition to 100% renewable energy while creating energy-related policies will also positively affect the applicability. The general steps that can be taken to achieve the target are presented below in articles [27, 35, 36].

- Organize meetings with authorities to explain that the transition to 100% renewable energy is feasible and beneficial.

- Develop a local climate action plan for a rapid transition to 100% renewable energy.
- By increasing the awareness and practice of energy control in the society, to improve energy saving and access, to ensure clean energy production, to support small business activities; saving public money by reducing energy costs in local government buildings, reducing air and water pollution.
- Increasing public transportation in transportation and encouraging the use of renewable energy in transportation.
- To overhaul all transportation systems to make renewable energy healthier, more accessible, and sustainable, reduce fossil fuel dependence in transportation systems and combat climate change and air pollution. (For example, switching to electric energy in public vehicles, reducing and banning fossil fuel-powered cars in the city, incentivizing private electric vehicles.)
- Switch to renewable energy sources wherever possible and make buildings energy-efficient, including local authorities and public offices.
- Working with countries, cities, institutions, and organizations that have switched to 100% renewable energy, using their experiences, sharing ideas, contacting and examining the path they follow.
- Communities most affected by climate change, experiencing the direct effects of fossil fuels such as air, soil, and water pollution, are leaders transitioning to a new energy system[37].
- To ensure the rapid transition of primarily medical associations, hospitals, and health centers to 100% renewable energy, all medical authorities recognize the harm fossil fuels cause to public health, especially air pollution.
- Ensuring worker retraining and re-employment in the expanding renewable energy sector.
- Ensuring that trade unions and youth organizations working on this issue employ the transition to renewable energy for all, including workers in the fossil fuel sector.

4. CONCLUSIONS

The world is at a turning point due to the effects of climate change. The energy issue has become a problem with the increasing population, energy demand, and energy use. Contrary to the environmental pollution and negativities caused by fossil production, the advantages of renewable production necessitate the world's transition to 100% renewable energy. Renewable energy sources, including solar, wind, hydroelectricity, are at the heart of the transition to a less carbon and more sustainable energy system. The sun is only one of the renewable energy sources that can provide much more energy than the whole world can use in a year. Besides, it is an obvious fact that the more investments are made in renewable energy sources, the cheaper the electricity production will be. There is still a long way to go, both locally and globally, to reach a world powered by 100% renewable energy.

In the world, significant progress has been made in the transition to 100% renewable energy. Since 2007, the share of fossil production in electrical energy production globally has decreased from 79% to 68%. The share of renewable generation

also increased from 21% to 32%. It has been observed that the world has shown an increase of 6% for the concept of transition to 100% renewable energy in electrical energy production and can switch to 100% renewable energy at a rate of 26%. However, it is possible to increase this share, because the potential of renewable energy sources in different locations is very high. Depending on this potential, it is possible to meet the energy demand of countries with renewable generation. Regionally, Scotland aims to produce all its electrical energy from renewable energy sources by 2020. Albania, Norway, and Costa Rica are among the countries that have transitioned to 100% renewable energy. In the light of all this information, it is possible to say that the share of renewable generation in the world has increased, and the transition to 100% renewable energy has accelerated.

To accelerate this transition and live in a cleaner world, it is necessary to take many steps at the global/local level. First of all, a transition should be made from the grassroots to the national/global level. The transition to 100% renewable energy should be achieved step by step, first in the neighborhood and the city, then in the country, and finally in the world. For this, local governments have a great responsibility. Reducing fossil fuel projects and fossil fuel budget, the transition of all government institutions, primarily local government institutions, to 100% renewable energy, supporting the transition to 100% renewable energy economy are important steps that can be taken. The local government authorities' targeting of transition to 100% renewable energy while creating energy-related policies will also positively affect the applicability. Increasing the awareness and practice of energy control in society and supporting renewable energy in transportation, heating, and electricity production will be important steps in this regard.

The transition to 100% renewable energy will save energy and create the opportunity for clean energy production and create a healthier, more accessible, and sustainable energy system.

REFERENCES

- [1] Farfan, J., Fasihi, M., and Breyer, C. (2019). Trends in the global cement industry and opportunities for long-term sustainable CCU potential for Power-to-X. *Journal of Cleaner Production*, 217, 821-835. DOI: <https://doi.org/10.1016/j.jclepro.2019.01.226>
- [2] Yuan, B., Kongstein, O. E., and Haarberg, G. M. (2009). Electrowinning of Iron in Aqueous Alkaline Solution Using a Rotating Cathode. *Journal of the Electrochemical Society*, 156(2), D64. DOI: <https://doi.org/10.1149/1.3039998>.
- [3] Kermeli, K., ter Weer, P.-H., Crijns-Graus, W., and Worrell, E. (2015). Energy efficiency improvement and GHG abatement in the global production of primary aluminium. *Energy Efficiency*, 8(4), 629-666. DOI: 10.1007/s12053-014-9301-7
- [4] Suhr, M., Klein, G., Kourti, I., Gonzalo, M.R., Santonja, G.G., Roudier, S., and Sancho, L.D., (2015). Best available techniques (BAT) reference document for the production of pulp, paper and board. *Eur. Comm*, 906. DOI: <https://doi.org/10.2791/370629>
- [5] Kangas, P., Onarheim, K., Hankalin, V., and Santos, S. (2016). Carbon capture from integrated pulp and board mill. In *19th Conf Process Integr Model Optim Energy Savings Emiss Reduct*, Prague, Czech Republic

- [6] Caldera, U., and Breyer, C. (2020). Strengthening the global water supply through a decarbonised global desalination sector and improved irrigation systems. *Energy*, 200, 117507. DOI: <https://doi.org/10.1016/j.energy.2020.117507>
- [7] Bogdanov, D., and Breyer, C. (2016). North-East Asian Super Grid for 100% renewable energy supply: Optimal mix of energy technologies for electricity, gas and heat supply options. *Energy Conversion and Management*, 112, 176-190. DOI: <https://doi.org/10.1016/j.enconman.2016.01.019>
- [8] Stackhouse, P. and Whitlock, C. (2009). Surface Meteorology and Solar Energy (SSE) Release 6.0 Methodology. National Aeronautic and Space Administration (NASA). Langley, VA, USA
- [9] Norouzi, N., & Fani, M. (2022). Post-Covid-19 Energy Transition Strategies: Even Reaching 100% Renewable in Ecuador by 2055 is not Enough to Face Climate Change Issue. *Iranian (Iranica) Journal of Energy & Environment*, 13(1), 1-9. DOI:10.5829/ijee.2022.13.01.01
- [10] Stetter, D. (2012). Enhancement of the REMix energy system model: global renewable energy potentials, optimized power plant siting and scenario validation, University of Stuttgart, PhD thesis
- [11] Afanasyeva, S., Bogdanov, D., and Breyer, C. (2018). Relevance of PV with single-axis tracking for energy scenarios. *Solar Energy*, 173, 173-191. DOI: <https://doi.org/10.1016/j.solener.2018.07.029>
- [12] Verzano K. (2009). Climate Change Impacts on Flood Related Hydrological Processes: Further Development and Application of a Global Scale Hydrological Model. University of Kassel
- [13] Thrän, D., Buchhorn, M., Bunzel, K., Seyfert, U., Zeller, V., Müller, K., Matzdorf, B., Gaasch, N., Klöckner, K., Möller, I. and Starick, A. (2010). Globale und regionale Verteilung von Biomassepotenzialen Status-quo und Möglichkeiten der Präzisierung.
- [14] Eisentraut, A. and Brown, A. (2013). Technology roadmap: bioenergy for heat and power. *Management of Environmental Quality: An International Journal*, 24(1). DOI: 10.1108/meq.2013.08324aaa.005
- [15] IPCC. (2011). Renewable Energy Sources and Climate Change Mitigation — IPCC. Geneva: <https://www.ipcc.ch/report/renewable-energy-sources-and-climate-change-mitigation/> (accessed on August 24, 2020).
- [16] Aghahosseini, A., Bogdanov, D., and Breyer, C. (2017). A Techno-Economic Study of an Entirely Renewable Energy-Based Power Supply for North America for 2030 Conditions. *Energies*, 10(8), 1171.
- [17] Norouzi, N., de Rubens, G. Z., Choupanpiesheh, S., & Enevoldsen, P. (2020). When pandemics impact economies and climate change: exploring the impacts of COVID-19 on oil and electricity demand in China. *Energy Research & Social Science*, 68, 101654. <https://doi.org/10.1016/j.erss.2020.101654>
- [18] Aghahosseini, A. and Breyer, C. (2018). Assessment of geological resource potential for compressed air energy storage in global electricity supply. *Energy Conversion and Management*, 169, 161-173. DOI: <https://doi.org/10.1016/j.enconman.2018.05.058>
- [19] World Steel Association. (2008). Steel and Energy Fact Sheet. Brussels: http://www.steelforpackaging.org/uploads/ModuleXtender/Themesslides/10/Fact_sheet_Energy.pdf (accessed on August 24, 2020)

- [20] Fasihi, M., Bogdanov, D., and Breyer, C. (2016). Techno-Economic Assessment of Power-to-Liquids (PtL) Fuels Production and Global Trading Based on Hybrid PV-Wind Power Plants. *Energy Procedia*, 99, 243-268. DOI: <https://doi.org/10.1016/j.egypro.2016.10.115>
- [21] Fasihi, M., Weiss, R., Savolainen, J., and Breyer, C. (2021). Global potential of green ammonia based on hybrid PV-wind power plants. *Applied Energy*, 294, 116170. DOI: <https://doi.org/10.1016/j.apenergy.2020.116170>
- [22] Fasihi, M., Breyer, C. (2017). Synthetic Methanol and Dimethyl Ether Production based on Hybrid PV-Wind Power Plants. *11th Int. Renew. Energy Storage Conf. (IRES 2017)*, Düsseldorf, March 14-16, 2017
- [23] European Aluminium Association. Life Cycle Inventory data for aluminium production and transformation processes in Europe. Brussels: 2013. <https://european-aluminium.eu/media/1329/environmental-profile-report-for-the-european-aluminium-industry.pdf> (accessed on August 24, 2020)
- [24] [EC] - European Commission. Greenmelt - Laymans report. Duffel: 2000. https://ec.europa.eu/environment/life/project/Projects/files/laymanReport/LIFE96_ENV_B_000477_LAYMAN.pdf (accessed on August 24, 2020)
- [25] Australian Government Department of Industry Innovation and Science, Resources and Energy Quarterly - March 2018. Canberra: 2018. <https://publications.industry.gov.au/publications/resourcesandenergyquarterlymarch2018/index.html> (accessed on August 24, 2020)
- [26] World Aluminium — Mass Flow Statistics n.d. <http://www.world-aluminium.org/statistics/massflow/> (accessed on August 24, 2020)
- [27] Kuparinen, K., Vakkilainen, E., and Tynjälä, T. (2019). Biomass-based carbon capture and utilization in kraft pulpmills. *Mitigation and Adaptation Strategies for Global Change*, 24(7), 1213-1230. DOI: 10.1007/s11027-018-9833-9
- [28] Caldera, U., Bogdanov, D., Afanasyeva, S., and Breyer, C. (2018). Role of Seawater Desalination in the Management of an Integrated Water and 100% Renewable Energy Based Power Sector in Saudi Arabia. *Water*, 10(1), 3. DOI: <https://doi.org/10.3390/w10010003>
- [29] Caldera, U., and Breyer, C. (2018). The role that battery and water storage play in Saudi Arabia's transition to an integrated 100% renewable energy power system. *Journal of Energy Storage*, 17, 299-310. DOI: <https://doi.org/10.1016/j.est.2018.03.009>
- [30] Norouzi, N., & Kalantari, G. (2020). The sun food-water-energy nexus governance model a case study for Iran. *Water-Energy Nexus*, 3, 72-80. <https://doi.org/10.1016/j.wen.2020.05.005>.
- [31] Praliyev, N., Zhunis, K., Kalel, Y., Dikhanbayeva, D., and Rojas-Solórzano, L. (2020). Impact of One- and Two-axis Solar Tracking on Techno-Economic Viability of On-Grid PV Systems: Case of Burnoye-1, Kazakhstan. *International Journal of Sustainable Energy Planning and Management*, 29, 79–90. <https://doi.org/10.5278/ijsepm.3665>.
- [32] Brown, T., Schlachtberger, D., Kies, A., Schramm, S., and Greiner, M. (2018). Synergies of sector coupling and transmission reinforcement in a cost-optimised, highly renewable European energy system. *Energy*, 160, 720-739. DOI: <https://doi.org/10.1016/j.energy.2018.06.222>
- [33] Norouzi, N. (2021). 4E analysis of a fuel cell and gas turbine hybrid energy system. *Biointerface Res. Appl. Chem.*, 11, 7568-7579.

- [34] Mathiesen, B. V., Lund, H., Connolly, D., Wenzel, H., Østergaard, P. A., Möller, B., Nielsen, S., Ridjan, I., Karnøe, P., Sperling, K., and Hvelplund, F. K. (2015). Smart Energy Systems for coherent 100% renewable energy and transport solutions. *Applied Energy*, 145, 139-154. DOI: <https://doi.org/10.1016/j.apenergy.2015.01.075>
- [35] Gils, H. C., Simon, S., and Soria, R. (2017). 100% Renewable Energy Supply for Brazil—The Role of Sector Coupling and Regional Development. *Energies*, 10(11), 1859. <https://doi.org/10.3390/en10111859>
- [36] Taljegard, M., Walter, V., Göransson, L., Odenberger, M., and Johnsson, F. (2019). Impact of electric vehicles on the cost-competitiveness of generation and storage technologies in the electricity system. *Environmental Research Letters*, 14(12), 124087. DOI: 10.1088/1748-9326/ab5e6b
- [37] Breyer, C., Fasihi, M., Bajamundi, C., and Creutzig, F. (2019). Direct Air Capture of CO₂: A Key Technology for Ambitious Climate Change Mitigation. *Joule*, 3(9), 2053-2057. DOI: <https://doi.org/10.1016/j.joule.2019.08.010>

Article copyright: © 2021 Nima Norouzi, Maryam Fani. This is an open access article distributed under the terms of the [Creative Commons Attribution 4.0 International License](https://creativecommons.org/licenses/by/4.0/), which permits unrestricted use and distribution provided the original author and source are credited.





CALL FOR PAPERS

Trends in Renewable Energy

ISSN Print: 2376-2136 ISSN online: 2376-2144

<http://futureenergysp.com/index.php/tre/>

Trends in Renewable Energy (TRE) is an open accessed, peer-reviewed semi-annual journal publishing reviews and research papers in the field of renewable energy technology and science. The aim of this journal is to provide a communication platform that is run exclusively by scientists. This journal publishes original papers including but not limited to the following fields:

- ✧ Renewable energy technologies
- ✧ Catalysis for energy generation, Green chemistry, Green energy
- ✧ Bioenergy: Biofuel, Biomass, Biorefinery, Bioprocessing, Feedstock utilization, Biological waste treatment,
- ✧ Energy issues: Energy conservation, Energy delivery, Energy resources, Energy storage, Energy transformation, Smart Grid
- ✧ Environmental issues: Environmental impacts, Pollution
- ✧ Bioproducts
- ✧ Policy, etc.

We publish the following article types: peer-reviewed reviews, mini-reviews, technical notes, short-form research papers, and original research papers.

The article processing charge (APC), also known as a publication fee, is fully waived for the Trends in Renewable Energy.

Call for Editorial Board Members

We are seeking scholars active in a field of renewable energy interested in serving as volunteer Editorial Board Members.

Qualifications

Ph.D. degree in related areas, or Master's degree with a minimum of 5 years of experience. All members must have a strong record of publications or other proofs to show activities in the energy related field.

If you are interested in serving on the editorial board, please email CV to editor@futureenergysp.com.